Winter 12-2013

ULTRASONIC PROPAGATION AND SCATTERING IN PEARLITIC STEEL

Hualong Du
University of Nebraska-Lincoln, hualong.du@huskers.unl.edu

Du, Hualong, "ULTRASONIC PROPAGATION AND SCATTERING IN PEARLITIC STEEL" (2013). *Engineering Mechanics Dissertations & Theses*. 38.
https://digitalcommons.unl.edu/engmechdiss/38

ULTRASONIC PROPAGATION AND SCATTERING IN PEARLITIC STEEL

by

Hualong Du

A DISSERTATION

Presented to the Faculty of

The Graduate College at the University of Nebraska

In Partial Fulfilment of Requirements

For the Degree of Doctor of Philosophy

Major: Mechanical Engineering and Applied Mechanics

Under the Supervision of Professor Joseph A. Turner

Lincoln, Nebraska

December, 2013

ULTRASONIC PROPAGATION AND SCATTERING IN PEARLITIC STEEL

Hualong Du, Ph. D.

University of Nebraska, 2013

Adviser: Joseph A. Turner

Diffuse ultrasonic backscatter measurements have been especially useful for extracting microstructural information and for improving flaw detection in materials. In this dissertation, this approach is applied to inspection of railroad wheels. To improve the wear resistance, the tread surfaces of railroad wheels are usually quenched with water to increase the hardness. The pearlite phase of iron, characterized by alternating ferrite and cementite phases, is created by the quenching and the lamellar spacing within grains increases progressively from the quenched tread surface to deeper locations due to the non-uniform cooling rate. The quench depth is an important parameter governing the wheel performance.

In this dissertation, several aspects of ultrasonic methods are studied. A new singly-scattered response (SSR) model that includes lamellar duplex microstructure within grains is developed to investigate the dependence of ultrasonic backscatter on such a microstructure in pearlitic wheel steel. An ultrasonic attenuation model is developed to study the influence of pearlite phase on ultrasonic attenuation. The experimental results show that both ultrasonic scattering amplitudes and longitudinal attenuation drop dramatically near the tread surface of a quenched wheel due to the presence of pearlite. The quench depth is measured by fitting the variance curve from the tread surface with the SSR model that includes the graded lamellar spacing on the propagation path. A mode-converted (longitudinal-to-transverse, or L-T) SSR model that includes duplex microstructure within grains is also developed to examine the preferred orientation of microstructure in a quenched sample. Finally, the dependence of ultrasonic backscatter on stress is verified by observing the decrease of backscatter amplitudes measured from a 1018 steel block under a uniaxial load. The experimental results show a trend that is similar to the theoretical prediction. The residual stress in a quenched steel sample is estimated by quantifying the change of backscatter amplitudes with and without residual stress.

Diffuse ultrasonic backscatter techniques exhibit strong sensitivity to duplex microstructure, texture and stress, outcomes that can be applicable for quality control including microstructure evaluation, measurement of quench depth and residual stress.

ACKNOWLEDGMENTS

The work supported by *Amsted Rail* Inc. is greatfully acknowledged. I would like to thank my advisor Dr. Joseph A. Turner for constant guidance, inspiration, enthusiasm and support, without which I am not able to finish my Ph.D program.

I would like extend my thanks to my committee members Dr. Jeffrey Shield, Dr. Ruqiang Feng and Dr. Jiashi Yang for providing critical reviews and advices on my research work. Dr. Cameron Lonsdale, John Oliver and Brent M. Wilson from *Amsted Rail* are acknowledged for their collaboration and helpful discussion about this work.

I would like to express my gratitude to my colleagues, Christopher M. Kube, Lucas Koester and Ping Hu for their suggestions, support, assistance and discussions in this project. I would like to thank the departmental faculties and staffs for providing assistance whenever needed.

Finally, I would like to appreciate my parents, my brother and my wife for their never ending support, understanding and patience throughout my entire academic career.

Contents

Contents **v**

List of Figures **viii**

List of Tables **xiii**

1 Introduction **1**

2 Background **7**

2.1 Pearlitic Steel 8

2.2 Attenuation Model 11

2.3 Statistical Backscatter Model 12

2.4 Backscatter Applications 14

2.5 Wheel Inspections 16

3 Ultrasound Propagation in a Polycrystalline Media **19**

3.1 Dyson Equation and the Mean Green's Function 20

3.2 Bethe-Salpeter Equation and Green's Function Covariance 22

3.3 Sources, Receivers, Mean and Mean Square Signals 23

3.4 Singly Scattered Response (SSR) 26

3.5 Wigner Transform of a Piston Transducer 29

3.6 Singly Scattered Response (SSR) from a Piston Transducer 32

4 Ultrasonic Backscatter from Lamellar Duplex Microstructure in Pearlitic Steel 35

4.1 Theoretical Model 36

4.2 Model Results 44

4.3 Experiments 47

4.3.1 Backscatter Measurements 47

4.3.2 Cross Section Mapping 57

4.3.3 Ultrasonic Backscatter and Hardness 60

4.4 Summary 62

5 Measurement of Quench Depth in Quenched Railroad Wheels 64

5.1 Theory 65

5.2 Model Results 66

5.3 Experiments 70

5.4 Summary 77

6 Ultrasonic Attenuation in Pearlitic Steel 79

6.1 Theoretical Model 81

6.2 Model Results 86

6.3 Experiments 89

6.4 Summary 95

7 Mode-converted Diffuse Backscatter in Pearlitic Steel 96

7.1 Theoretical Model 97

7.2 Model Results 105

7.3 Experiments 108

7.4 Summary 116

8 Dependence of Ultrasonic Backscatter on Stress 118

8.1 Stress-dependent Ultrasonic Backscatter Coefficient 120

8.2 Experiments 123

8.2.1 Uniaxial Stress on a 1018 Steel Block 123

8.2.2 Effects of Residual Stress on Ultrasonic Backscatter 125

8.2.3 Water Quenching 131

8.3 Summary 140

9 Conclusions and Future Work 142

Bibliography 147

List of Figures

1.1 An example ultrasonic signal reflected from a foreign object in a steel sample. 2
1.2 A typical backscatter signal. 4

2.1 Phase diagram of carbon steel. 9
2.2 Redistribution of carbon and iron atoms during eutectoid reaction. . . . 10

4.1 Lamellar duplex microstructure (pearlite phase) in the railroad wheel steel. 39
4.2 Schematic of lamellar duplex microstructure within an individual grain (pearlite phase). 42
4.3 Spatial variance curves from the model given by Eq. (4.13) with and without the inclusion of duplex microstructure within grains ($M = 0.9$) with a transducer center frequency of 10 MHz. 45
4.4 Normalized spatial variance amplitudes versus frequency, (a) by fixing d/L=1/24, L=24 μm, (b) by fixing M =0.75 and L=24 μm. 46
4.5 Cross section images of polished railroad wheel samples, (a) an unquenched wheel, (b) a quenched wheel. 48
4.6 Example of a typical waveform included in the spatial variance calculations of Eq. (4.14). The part of the signal of primary interest lies between the front and back wall echoes and is due to scattering from the grains. . . . 50

4.7 Spatial variance curves with a 10 MHz focused transducer, (a) for an unquenched wheel, (b) for a quenched wheel. 51
4.8 Distribution of spatial variance amplitudes from tread surface to the deeper location with 10 MHz and 15 MHz focused transducers. 53
4.9 Distribution of calculated lamellar space d from tread surface to the deeper location. 55
4.10 Micrographs of pearlite phase in a railroad wheel steel, (a) near the tread surface, (b) at a depth of 30 mm from the tread. 56
4.11 A cross section image of a quenched wheel sample. 57
4.12 C-scan images of cross section of wheel slice samples, (a) before quenching, (b) after quenching. 58
4.13 Variance amplitude distribution for cross section mapping of wheel samples, (a) before quenching, (b) after quenching. 59
4.14 Comparison between the measured hardness and spatial variance amplitude from the tread surface to deeper positions. 60

5.1 (a) Schematic of the ultrasonic testing of a railroad wheel sample using the normal incident ultrasound, (b) The dependence of lamellar spacing d on depth z. 67
5.2 Normalized spatial variance curves with respect to different profiles shown in Fig. 5.1b of lamellar spacing distribution. 68
5.3 Normalized variance curves corresponding to different water paths (calculated using M=0.9 in Eq. (5.2)). 69
5.4 Images of a quenched railroad wheel sample produced by *Griffin Wheel, Inc.*, (a) cross section, (b) tread surface. 71

5.5 The spatial variance curves for tread surface and cross section scanning along with the fitting curves. 72

5.6 The spatial variance curves with respect to varying material paths. $A_i, (i = 1, 2, 3)$ represents the variance peak. 73

5.7 The mean error square between experimental variance curve and theoretical curve versus the quench depth z_1. 75

5.8 The normalized spatial variance curves and corresponding curve fits. . . . 76

6.1 The attenuation components α_{LL}, α_{LT}, α_{TL} and α_{TT} versus frequency. (L=24 μm, d=2.0 μm and M=0.9) 87

6.2 The effects of the parameters M and d on (a) longitudinal attenuation, (b) transversal attenuation (L=24 μm). 88

6.3 An image of cross section of an unquenched railroad wheel sample (manufactured by *Griffin Wheel. Inc.*). 89

6.4 Signal used for attenuation calculation (An unfocused transducer with 10 MHz central frequency). 90

6.5 FFT of the back wall reflections shown in Fig. 6.4. 91

6.6 Experimental attenuation versus frequency with respect to different positions (shown in Fig 6.3). 92

6.7 Distribution of attenuation coefficients from quenched surface to deeper locations with respect to f=10 MHz. 93

6.8 Attenuation map of the cross section of a quenched railroad wheel sample. 94

7.1 A schematic of the mode-converted (L-T) ultrasonic backscatter using a pitch-catch transducer configuration (adapted from [69]). 97

7.2 The geometrical relationship for coordinate transformation. 98

7.3 Schematics of lamellar duplex microstructure within an individual grain (pearlite phase), (a) a 3D model, (b) the cross section feature sliced in the 1-3 plane, (c) the cross section feature sliced in the 1-2 plane. 102

7.4 The variance amplitudes versus the lamellar spacing d, the angle $\theta_0 = \arccos d/L$ shown in Eq. (7.9) varies with increasing d, while L=24 μm, M=0.9. 105

7.5 The attenuation coefficients versus the lamellar spacing d (L=24 μm, M=0.9). 106

7.6 The backscatter coefficient including lamellar microstructure within grains given in Eq. (7.11) versus the lamellar spacing d (L=24 μm, M=0.9). . . 107

7.7 The experimental setup for the mode-converted diffuse ultrasonic backscatter in a pitch-catch configuration. 109

7.8 The cross section image of a wheel sample annealed to remove the residual stress. 110

7.9 Experimental spatial variance curves of ultrasonic backscattered signals, (a) near the tread surface, (b) 30 mm from the tread. 112

7.10 Distribution of variance amplitudes from the tread surface to deeper locations. 113

7.11 The calculated lamellar spacing d versus the correlation length L using the variance amplitudes measured in two directions. 115

7.12 Distribution of the calculated lamellar spacing d and the correlation length L with depth from the tread surface to deeper locations (M=0.9). 116

8.1 Experimental setup for the backscatter measurement under a uniaxial load. 123

8.2 The measured spatial variance peaks versus applied loads. 124

8.3 (a) Cross section and (b) rim surface images of a 50 mm thick wheel sample. 126

8.4 The variation of spatial variance amplitudes after annealing from the rim surface. 128

8.5 Variance amplitude distribution on the cross section of the wheel slice,(a) before annealing, (b) after annealing. 129

8.6 Comparison of spatial variance curves before and after annealing measured from the cross section. 130

8.7 Image of a 1080 steel block (2 inch × 2 inch × 3 inch). 132

8.8 Experimental setup for quench with running water. 132

8.9 Comparison of spatial variance curves before and after water quenching. 133

8.10 Spatial variance curves measured from the whole quenched surface after quenching and after annealing with the normal incidence ultrasound. . . 134

8.11 The residual stress state in the quenched steel block, the normal direction of the quenched surface is parallel to T_{11}. 135

8.12 Distribution of the estimated residual stress (MPa) along the quenching direction based on the elastic constants of pure iron. 137

8.13 Variance curves before and after annealing at the subarea with minimum amplitude change as shown in Fig. 8.12. 138

8.14 Variance curves before and after annealing at the subarea with maximum amplitude change as shown in Fig. 8.12. 139

List of Tables

4.1 Constants used in the theoretical model to examine the influence of lamellar spacing. The wave speeds and attenuation values are determined from scattering models from the grains without the lamellar structure as derived in [7]. 44

5.1 Measured variance peaks corresponding with different water paths. . . . 74

6.1 Single crystal elastic constants of iron used in the formulation of attenuation given in Eqs. (6.9). 86

8.1 Single crystal second - and third-order elastic constants (GPa) for pure iron. 122

8.2 Theoretical backscatter coefficients of pure iron [39]. 122

8.3 Theoretical backscatter coefficients of pure iron under five residual stress states, respectively [39]. 136

Chapter 1

Introduction

Nondestructive testing (NDT) or evaluation (NDE) techniques are powerful methods for material inspection. Compared with the traditional destructive inspection techniques such as hardness testing or micrographic analysis that damages the test sample through cutting or polishing, the primary advantage is that the material is not destroyed during inspection. There are several nondestructive techniques that have been used for routine measurements in industry, such as ultrasound, X-ray diffraction, electromagnetic waves, Eddy current, etc. All these NDT methods refer to the interaction between an incident wave with the material. Therefore, basic knowledge of the wave interaction with the material is required for interpreting the experimental results. This main focus of this dissertation is the study of ultrasonic wave propagation and scattering in pearlitic steel.

Typically, an ultrasonic experiment involves an ultrasonic wave generated by a transducer that is transmitted through a coupling medium and then into the sample. The ultrasonic waves reflected from foreign objects, including the voids, inclusions and defects are received by the same or another transducer in the pulse-echo or pitch-catch configuration, respectively. Three types of transducers are typically used in ultrasonic measurements including contact, air-coupled and immersion transducers. Contact transducers usually use a layer of honey or glycerin between the transducer face and the sample which acts as the coupling medium. Air-coupled transducers use air as the coupling medium. In an ultrasonic test with an immersion transducer, both the transducer and the test sample are immersed in a fluid. Water is the most common coupling medium for this type of transducer due to the fact that it has low viscosity, is easily obtained and is environmentally friendly.

Fig. 1.1 shows an experimental setup using an immersion transducer in the pulse-echo configuration, along with a typical waveform. The immersion transducer transmits the ultrasonic pulse through water into the sample and the ultrasonic wave reflects from the top surface of the sample due to the acoustic impedance mismatch. The portion of energy reflected back to the same transducer is called the frontwall reflection, while the ultrasonic echo reflected from the back surface is called the backwall reflection. Any reflection appearing between the frontwall and the backwall indicates the presence of foreign material. A gate is usually set between the frontwall and backwall reflections so that the maximum amplitudes of reflected signals from foreign

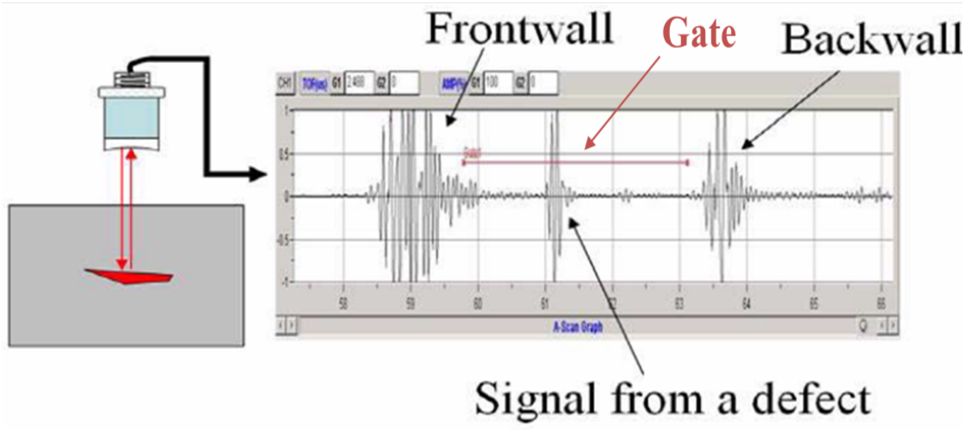

Figure 1.1: An example ultrasonic signal reflected from a foreign object in a steel sample.

objects can be monitored. The amplitudes are displayed in an image that is called a C-scan image, in which the locations of the foreign objects are mapped. Another type of setup that is usually used in ultrasonic inspection is the pitch-catch configuration, in which two transducers behave as the transmitter and receiver, separately.

As the ultrasonic wave propagates through polycrystalline media, energy is lost due to scattering and absorption. The lost energy causes the input waves to decay, an effect referred to as a attenuation. The pitch-catch method is often used for material inspection where a large amount of energy is lost from the coherent ultrasonic wave, so that it only needs to propagate a short distance before detection.

The defects in a structural material can act as stress concentrators that can contribute to fatigue crack initiation, and ultimately cause the failure of a structure. Many conventional ultrasonic techniques involve identification of the signals that reflect from the defects in the material. If the sizes of the defects are much larger than the order of heterogeneities in a polycrystalline material, the detection is relatively easy, the gate amplitude can be placed above the effective material 'noise' that comes from the heterogeneous background. However, if the defect size is on the order of the heterogeneities, the reflected signals are often masked by the incident energy that scatters from the heterogeneous background. In such a case, one can increase the inspection frequency with the hope of increasing the sensitivity to the defect, but this method usually increases the background noise as well. The grain noise can hamper the detection of minor defects, so that understanding the grain noise level reflected from the background will be useful for quantifying the probability of identifying a minor defect in the material.

Many approaches have been proposed to quantify the diffuse scattering noise from the background, heterogeneous medium such that any deviations from this response can be attributed to the presence of a defect. To obtain the ultrasonic scattering from heterogeneities, a high amplifier gain is used. Fig. 1.2 shows a single pulse-echo backscatter signal collected from a heterogeneous material. The different colors in the test material denote the orientations of the polycrystalline grains. The electronic noise level is much lower in contrast to the ultrasonic backscatter from heterogeneities such that the electronic noise can be neglected. The reflected signals from minor flaws might emerge within the scattering from the background. Differentiating the scattered signal from the signal reflected from minor defects is a very challenging problem. Ultrasonic scattering (grain noise) reflected from the heterogeneities is related to the physical properties of the scatterers, such as grain size, microstructure, texture and so on, which can also be used to estimate the grain size if properly modeled. However, the scattering between the frontwall and the backwall reflections shown in Fig. 1.2 is completely random due to the random orientations of the grains, so that it is highly dependent on the test position. The scattered signal at one position might be completely different from those measured from other positions. Therefore, statistical methods are used to analyze the collected signals.

In this dissertation, ultrasonic propagation and scattering in pearlitic steel is studied. A statistical scattering model is proposed to quantify the duplex microstructure in pearlitic steel from the ultrasonic signals collected on a sample. In chapter 2, the

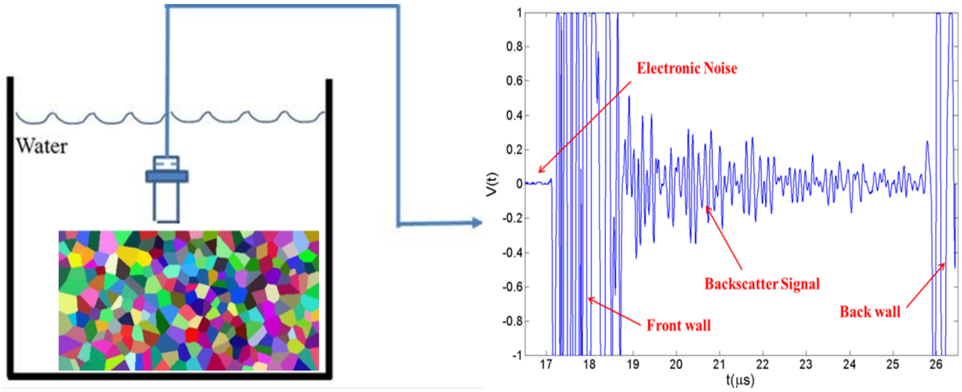

Figure 1.2: A typical backscatter signal.

background of material characterization with ultrasonic backscatter is discussed. In chapter 3, the theoretical model for the scattered response (the spatial variance of the ultrasonic backscattered signals) within a multiple scattering formalism is reviewed. The singly scattered response (SSR) is obtained by assuming the wave scatters only once before returning to the transducer.

In chapter 4, the developed SSR model is extended by including the effects of lamellar duplex microstructure characterized by the alternating cementite and ferrite phases in railroad wheel steel. The dependence of ultrasonic backscatter on duplex microstructure within grains is observed by comparing cross section measurements from an unquenched wheel with that from a quenched wheel. The modified model is utilized to fit the experimental results measured from the cross section of a quenched wheel sample.

In chapter 5, the SSR model including the effects of duplex microstructure is further modified by considering the gradation of lamellar spacing on the propagation path. The SSR model is compared with backscatter measurements from the wheel tread surface. The effects of the graded lamellar duplex microstructure along the propagation path on ultrasonic scattering can be observed by comparing backscatter measurements from the tread surface with those from the cross section. The quench depth can be estimated by fitting the variance curve of ultrasonic backscatter signals measured from the tread surface with the graded SSR model. Chapter 6 discusses the dependence of ultrasonic scattering attenuation on lamellar duplex microstructure. An ultrasonic attenuation model that includes the lamellar duplex microstructure within grains is developed for studying the influence of lamellar spacing on attenuation.

In chapter 7, a mode-converted (longitudinal-to-transverse, or L-T) SSR that models the received shear wave scattered by an incident longitudinal wave is modified to include the effects of lamellar duplex microstructure. The experiments are performed on the cross section of a quenched wheel sample using two focused transducers in the pitch-catch configuration measured in two directions. The theoretical model is compared with the experimental results. The lamellar spacing and the correlation length are calculated with the L-T spatial variance amplitudes measured in two directions. Chapter 8 investigates the effects of the applied stress and residual stress on ultrasonic scattering generated by water quenching. The variation of the variance amplitudes with and without residual stress is quantified, from which the residual stress is estimated with the SSR model. Finally, chapter 9 gives the conclusions and future work.

Chapter 2

Background

Ultrasonic energy in the form of elastic waves is extensively used for measuring the quality of structural components in the manufacturing process or during service. Applications are comprised of detecting the size of discrete flaws that cause failure (e.g., inclusion or cracks), characterizing the degradation of materials during the service time (e.g., fatigue of aircraft components or embrittlement of pressure vessels in nuclear power plants), monitoring the structural changes of materials that occur during manufacturing processes (e.g., grain size, microstructure and porosity) to provide information to modify the manufacturing process.

If an ultrasonic wave passes through a homogeneous material, equally spaced echoes with equal amplitudes can be observed. When the ultrasound propagates in polycrystalline medium, it loses energy due to scattering and absorption, which leads to an exponential decay of the echo (attenuation) and the appearance of grain noise between the echoes. Many structural materials are comprised of polycrystalline grains. Because grains are anisotropic and their orientation varies from grain to grain, the material has a continuous variation of elastic properties. The change of sonic properties causes some of the incident wave energy to be reflected, this detectable energy is known as "grain noise" or scattering. The scattered signals carry very important information about the sample microstructure and can be used to quantify the grain size and microstructure if properly modeled [24], [27], [41], [42].

The importance of understanding the scattering is not limited to its effects on flaw detection and characterization. Other functions in ultrasonic nondestructive evaluation, such as characterizing material microstructure during manufacturing or degradation during service, are also highly dependent on the understanding of the interactions between ultrasound and microstructure. In the following sections of this chapter, the microstructure in pearlitic steel and the formation of the pearlite phase is discussed. Ultrasonic attenuation and statistical backscatter models developed for cubic and hexagonal polycrystalline materials with various microstructures are reviewed. The methods for the inspection of railroad wheels including flaw inspection, microstructure evaluation and measurements of hardening layers are also summarized.

2.1 Pearlitic Steel

Pearlite is a two-phase, lamellar (or layered) structure composed of alternating layers of α-ferrite (88 wt%) and cementite (Fe_3C, 12 wt%) that occurs in some steels and cast irons. Fig. 2.1 shows a phase diagram of carbon steel. When an iron-carbon alloy containing eutectoid composition of 0.76 % carbon is heated up to 727 °C (1030 °F, the eutectoid temperature), the structure contains only austenite (γ) phase. The eutectoid reaction begins when the sample temperature cools to 727 °C. The iron-iron carbide eutectoid reaction is given by [57]

$$\gamma_{0.77\%C} \rightarrow \alpha_{0.0218\%C} + \mathrm{Fe_3C}_{6.67\%C}. \tag{2.1}$$

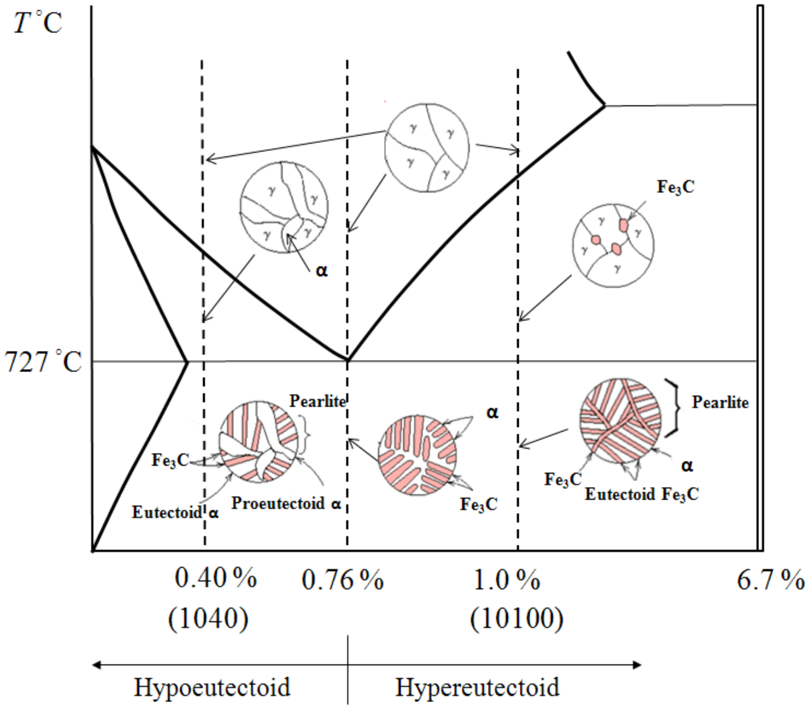

Figure 2.1: Phase diagram of carbon steel.

The austenite has an intermediate carbon concentration that transforms to a ferrite phase with a much lower carbon content, and also cementite with a much higher carbon concentration. Atoms must diffuse during the reaction as shown in Fig. 2.2. Most carbon atoms diffuse to the cementite (Fe_3C) phase, while a great percentage of iron atoms diffuse to the ferrite (α) phase. This redistribution of atoms is easiest if the diffusion distances are short, which is the case when the α and Fe_3C phases grow as thin lamellae, or plates.

Temperature plays an important role in the rate of the austenite-to-pearlite transformation. The thickness ratio of the ferrite and cementite layers in pearlite is approximately 8 to 1. However, the absolute layer thickness depends on the temperature at which the isothermal transformation is allowed to occur. At temperatures just below the eutectoid point, relatively thick layers of both the α-ferrite and Fe_3C phases are produced; this microstructure is called coarse pearlite. At these temperatures, diffusion rates are relatively high, such that carbon atoms can diffuse relatively long distances during the transformation, which results in the formation of thick lamellae. With decreasing temperature, the carbon diffusion rate decreases, and the layers become progressively thinner. The thin-layered structure produced is called fine pearlite. The mechanical properties are dependent on lamellar thickness.

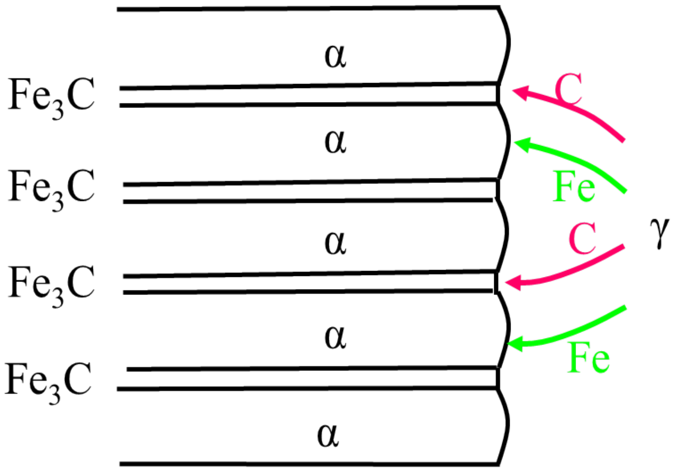

Figure 2.2: Redistribution of carbon and iron atoms during eutectoid reaction.

Hypoeutectoid steels contain less than 0.76 % C, and ferrite is the primary or proeutectoid microconstituent in hypoeutectoid alloys. When the hypoeutectoid alloy containing 0.60 % C is heated below 750 °C, ferrite precipitates and grows at the austenite boundaries as shown in Fig. 2.1. Primary ferrite continues to grow until the temperature falls to 727 °C. The remaining austenite at that temperature is now surrounded by ferrite and has changed in composition from 0.60 % C to 0.77 % C. Subsequent cooling to below 727 °C causes all of the remaining austenite to transform to pearlite by the eutectoid reaction. The final structure contains two phases, primary ferrite and cementite. The primary phase is Fe_3C in the hypereutectoid alloy containing more than 0.76 % C, which is formed at the austenite grain boundaries. After the austenite cools through the eutectoid reaction, the steel contains hard, brittle cementite surrounding islands of pearlite.

2.2 Attenuation Model

When an ultrasonic wave propagates in polycrystalline materials, it scatters on grain boundaries due to the relative misorientation of the crystallites. The lost energy due to scattering is typically described in terms of the ultrasonic scattering attenuation, a quantity that can be measured and can serve as a metric to characterize the microstructure of polycrystalline materials [3]. Many previous studies of ultrasonic scattering in polycrystals focused on scattering-induced attenuation as a function of frequency and microstructure [2] - [7], [9], [10], [43], [45]. Lifshits and Parkhomovski [2] developed a general scattering attenuation model which was suitable for a wide frequency range. Merkulov [4] simplified the general theory and reduced the results to an elegant equation for attenuation coefficients for both the Rayleigh and Stochastic regimes for cubic polycrystalline materials. He also derived attenuations in those regimes for hexagonal polycrystals. Hirsekorn [5] developed a scattering model by using a Born series and by considering multiple scattering in a test material.

Stanke and Kino [6] developed a general theory for equiaxed untextured polycrystalline media with cubic symmetry in all frequency ranges. To obtain their final results they used the the second-order Keller approximation [56]. The theory was proposed to be valid for all frequency ranges and for an arbitrary crystal anisotropy factor. The final solution of Stanke and Kino [6] can also be simplified with the Born approximation. The Born approximation considers the scattered wave function by a plane wave if the scatter potential is so weak that it will distort only slightly the incident plane wave. Weaver [7] presented a general solution to determine the diffusivity of ultrasound for the untextured cubic-symmetry polycrystalline material using the Dyson equation. The Born approximation was employed to simplify the general solution. Compared with the Stanke and Kino's theory using Keller approximation, Weaver's solutions matched with those of Stanke and Kino for strongly scattering materials up to very high frequencies. However, the explicit equations for attenuation were identical to those of the Born approximation of Stanke and Kino [6]. The results were suitable for the frequency range below the geometrical limit.

Ahmed and Thompson [9] extended the Stanke and Kino model [6] to untextured cubic materials with elongated grains. An integral solution was numerically evaluated for the Green's function and the attenuation was calculated as a function of different microstructural parameters. Yang et al. [45] studied the shape effects of elongated grains on ultrasonic attenuation in cubic polycrystalline materials. Turner [10] presented an attenuation model for textured materials with cubic symmetry grains using Weaver's method, and Yang et al. [11] also used Weaver's approach to develop a general solution for textured materials with grains of hexagonal symmetry. Yang et al. [44], [51] developed integrated attenuation models for ultrasonic wave propagation and scattering in a hexagonal polycrystalline medium with equiaxed and elongated grains, respectively. Han and Thompsan [48] and Lobkis and Rokhlin [49], [50] studied the effects of duplex microstructure in titanium alloys on ultrasonic backscatter and attenuation.

2.3 Statistical Backscatter Model

The main focus here is the analysis of the received signals collected in a typical C-scan scan rather than on each waveform by itself to extract the microstructural information of the test sample. Statistical methods are usually used to quantify the diffuse scattering from the heterogeneities to infer microstructural information. H$\ddot{o}$ller [12], Rose [20], Margetan [13], Thompson [27], [41] and their workers pioneered the work of investigating ultrasonic scattering models for polycrystalline media. Rose [20], [47] developed the first backscatter model for polycrystals with equiaxed grains. Margetan et al. [13] derived a backscatter model within a single scattering assumption such that it includes all the necessary experimental parameters. Their theoretical model is mainly based on a normal incidence experimental setup, such that it is not able to be used with different experimental setups such as oblique incidence or a pitch-catch type setup. Margetan et al. [22] demonstrated experimental results using a pitch-catch technique by propagating only shear waves in a steel sample. They also discussed the necessity of considering multiple scattering in the model while inspecting samples with larger grain sizes with respect to the wavelength of the incident wave. Thompson et al. [23] showed that a theoretical model with a multiple scattering formalism is required to be developed to interpret experimental results by comparing experimental results with singly-scattered models. Han and Thompson [48] expanded the backscatter model for titanium alloys with duplex microstructure. They mainly focused on an arrangement of a second phase (called a colony) in the large macrograins (prime β grains of cubic symmetry). Lobkis et al. [49], [50] and Yang et al. [52] presented an ultrasonic backscatter model and experimental measurements in polycrystals with elongated single phase and duplex microstructures. They considered microtextural regions (MTRs) as the largest size phase which is formed by a secondary set of primary crystallites. The contribution of those crystallites to ultrasonic backscatter had been neglected in [48]. Recently, Ghoshal et al. [24] developed a mathematical formalism that includes a transducer model within a multiple scattering framework. The more general model was reduced to the limit of the singly scattered response (SSR). The SSR simplified to a convolution between the Wigner transform of the source and receiver displacement response with a scattering operator that quantifies the scattering within the medium. Those simplified results matched the overall behavior observed in the original work of Margetan et al. [13]. The details on how the SSR model is derived is given in chapter 3.

Another important component in modeling ultrasonic backscatter experiments is the transducer beam model. Cook [25] presented the solution to the linear wave equation for planar and plane-plate piston transducers in a polar coordinate system. Gubernatis et al. [26] used the Green's function to derive the expression for the scattering amplitude to inspect flaws in an isotropic homogeneous elastic mediam in a three-dimensional domain. Thompson and Gray [27] calculated the acoustic field at the transducer face by assuming a single medium for the liquid-solid interfaces. Schmerr and Song [70] explained the Gaussian beam at oblique incidence through interfaces in great detail. A transducer beam model that can be used for both planar and curved interfaces was developed. It can be applied for inspecting curved surfaces such as railroad wheels, roller bearings and so on.

2.4 Backscatter Applications

The developed statistical models are utilized for analyzing the backscatter signals measured by experiments, through which the microstructure, or grain size can be evaluated. A significant number of experimental backscatter studies have been performed by Thompson and coworkers. Thompson et al. [87] gave a brief review of the classical understanding of how elastic waves are scattered by grain boundaries in randomly oriented polycrystalline materials. The backscatter experiments were conducted in different directions of titanium alloys taken from cylindrical components of aircraft engines with duplex microstructure. The grain elongation was demonstrated by comparing the backscatter measured from different directions. Margetan et al. [13] presented a study of the backscatter measured in a jet-engine nickel alloy in the pulse-echo configuration. The contribution from the microstructure known as the Figure-of-Merit (FOM), which is equal to the square root of the backscatter coefficient, was measured as a function of position, and its value was demonstrated to correlate well with the variation in the average grain sizes. Lobkis et al. [50] developed a backscatter model (known as the M-factor model) for titanium alloys with elongated single phase and duplex microstructures by considering microtextural regions (MTR) as the largest size phase that is formed by a secondary (small size phase) of prime α. The ultrasonic backscatter measurements were performed along several directions in engine-grade near-alpha titanium alloy samples. The experimental results matched well with the theoretical predictions.

In addition to microstructural information in materials, diffuse ultrasonic measurements have been shown to be sensitive to changes in applied stress and residual stress. Acoustoelasticity refers to the study of the relationship between applied stress and wave speed within solids. This relationship considers the influence of finite strain or wave displacement on higher-order material behavior. Often, linear-elastic approximations are not sufficient for describing material response under large strains. Acoustoelastic behavior is typically examined in two forms: the nonlinear response of single crystals under large accelerations or applied stress. The acoustoelastic response of the complex solid is described at the macroscale level. For polycrystals, single-crystal nonlinear behavior has been used to predict the nonlinear behavior of an ensemble of randomly oriented crystals. Researchers have applied the first-order grain statistics through wave speed for measuring ultrasonic propagation modes to extract stress information from complex solids [30] - [33]. In the last several decades, higher-order spatial statistics of polycrystals have been of interest. When high-frequency waves pass through polycrystals, ultrasonic scattering results from heterogenous boundaries. The second-order grain statistics, through the covariance of the elastic moduli fluctuations, have been used to connect single crystal properties to ultrasonic scattering behavior. Recently, Turner and Ghoshal [39] presented a theoretical basis to extract stress information from polycrystalline microstructures by considering second-order grain statistics through the covariance of elastic moduli fluctuations, an eighth-rank tensor. Kube et al. [40] confirmed the stress-dependence of the covariance tensor by measuring ultrasonic scattering under uniaxial loads.

Recently scientists have started to use diffuse ultrasonic backscatter methods for biomaterials to quantify the size of scatters and to locate the scatterer sites. Because scattered signals are sensitive to microstructural changes such that they might be able to be used for distinguishing diseased tissues from healthy tissues. Oleze and Zachary [29] suggested that a higher-order scattering model might be necessary to obtain accurate microstructure information from biological samples. Most singly-scattered models may lead to an under or over estimate of scatterer size. Thus, it may be necessary to develop higher-order scattering models to interpret better the experimental results.

2.5 Wheel Inspections

Flaws in railroad wheels can act as stress concentrators during service, which can result in the initiation of fatigue cracks, and ultimately cause the rim to split from a wheel. Ultrasound inspection techniques are widely used for detecting flaws in railroad wheels. Previous standards for the manufacturing inspection of railroad wheels using ultrasound have been replaced by new standards, for example EN 13262 [34] and RD32.144-2000 [35], both requiring ultrasonic testing by means of the immersion technique. The current requirement for the minimum detectable flaw size is DSR 1 mm (disc shape reflector, DSR, 1 mm diameter) for high-speed train wheels rims and DSR 2 mm for all other wheel rims. The minimum detectable flaw size for all other wheel areas (hub and disk areas) is DSR 3 mm. To meet all these criteria, a new Rail Wheel Inspection (RWI) system was developed by IZFP and its partners [59].

The mechanical behavior, such as hardness, of wheel steel is governed significantly by microstructure. Optical micrographs, X-ray diffraction (XRD) [60], scanning electron microscopy (SEM) [60], [62], transmission electron microscopy (TEM) [60], [61] have been used to observe the microstructure of the hardened layer on the quenched surface of pearlitic wheel/rail steel. The hardened layer was confirmed to be composed of severely deformed fine pearlite lamellae as well as nanocrystalline martensite, austenite and cementite. The lamellar spacing in fine pearlite phase was measured directly from the SEM images. All these methods are time consuming and require extensive sample preparation, including the cutting of the sample, mounting, grinding, polishing and etching. So far a non-destructive method using ultrasound has not been found to quantify the lamellar spacing in pearlitic steel.

To improve the wear resistance, the tread surfaces of wheels are usually quenched with cold water to improve the hardness. The quench depth that is defined as the thickness of the hardening layer plays an important role in determining the wheel performance. The quench depth is usually estimated from the measured hardness profile of the cross section from the quenched surface [63]. Hirao et al. [64] described a nondestructive test method to measure the hardening layer of steels with surface treatments (including induction hardening, carburizing, and then quenching and nitriding) by means of ultrasonic surface waves. Velocity measurements with the pulse-overlap technique demonstrated the frequency dependence of the surface-wave velocity, which implies that these treatments form a well-defined surface layer of uniform thickness, having different elastic properties than the matrix. The measured thicknesses were relatively consistent with the destructive observation of micro-Vickers hardness variation with depth. Fujisawa and Nakanishi [65] introduced a non-destructive method of measuring the hardening depth by using ultrasonic backscatter. They measured several bearing steels with various hardening depths. Backscattering amplitude patterns were obtained by averaging rectified signals of ultrasonic shear wave with changing incident positions. The first increasing point corresponded to the shore depth where bainite structure initiates.

The above discussion gives a brief survey of the available literature on wave scattering. There exists an enormous amount of information about scattering in heterogeneous media due to the important application for characterization of materials nondestructively. Technological advancements lead to the creation of the new materials with complex microstructure. Studying the wave interaction with such complex materials is very important for monitoring the structural health of components using nondestructive methods. Therefore, more theoretical models are required so that the experiments may be interpreted quantitatively.

Chapter 3

Ultrasound Propagation in a Polycrystalline Media

In this chapter, ultrasonic scattering within heterogeneous media is reviewed [24]. The mean and mean square signals from a model source and receiver in a random medium are investigated. The mean signal or the mean square signal is related to a convolution between the mean Green's function or Green's function covariance and the model transducer functions, respectively. The Dyson equation [7] is achieved to describe the mean Green's function and the Bethe-Salpeter equation results from consideration of the covariance. The latter equation is expanded in a multiple scattering series and the results inserted into the previously derived convolution expression for the mean square signal. The distribution function of the displacement profile is derived to model the beam pattern of an ultrasonic transducer through a liquid-solid interface. A singly-scattered response (SSR) model based on the assumption that ultrasonic wave scatters only once before returning back to the transducer is developed to investigate the dependence of microstructure on ultrasonic scattering. In later chapters, this SSR model is expanded for application to pearlitic steel with duplex microstructure within grains and to study the effects of lamellar duplex microstructure on ultrasonic scattering.

3.1 Dyson Equation and the Mean Green's Function

The analysis begins with the governing partial differential equation (PDE) for the Green's function $G_{i\alpha}(\mathbf{x},\mathbf{y},t)$ of an elastic medium with constant material density (set to unity) and modulus that varies randomly in space

$$[-\delta_{li}\frac{\partial^2}{\partial t^2}+\frac{\partial}{\partial x_k}\mu_{klij}(x)\frac{\partial}{\partial x_j}]G_{i\alpha}(\mathbf{x},\mathbf{y},t)=\delta^3(\mathbf{x}-\mathbf{y})\delta(t)\delta_{l\alpha}, \tag{3.1}$$

where $\mu_{klij}(\mathbf{x})$ is the position dependent elastic modulus tensor with a mean value of C^0_{klij}, and fluctuations from the mean given by $\gamma_{ijkl}(\mathbf{x})=\mu_{ijkl}(\mathbf{x})-C^0_{ijkl}$. This form for the PDE corresponds to the case of a random polycrystal, in which case $\mathbf{C}^0$ is defined as the volume average or the Voigt, effective modulus. As their mean $\langle\rangle$ is zero, the leading order non-trivial quantity is the moduli-covariance Λ, defined by

$$\langle\gamma_{ijkl}(\mathbf{x})\gamma_{\alpha\beta\gamma\delta}(\mathbf{y})\rangle=\Lambda(\mathbf{x}-\mathbf{y})^{\alpha\beta\gamma\delta}_{ijkl}, \tag{3.2}$$

where the angular brackets $\langle\rangle$ define ensemble average quantities. The moduli covariance is considered to depend on the difference between vector $\mathbf{x}$ and $\mathbf{y}$ based on the assumption of statistical homogeneity. If the temporal Fourier transform of $\mathbf{G}$ defined by $G_{i\alpha}(\mathbf{x},\mathbf{y},\omega)=\int_{-\infty}^{\infty}G_{i\alpha}(\mathbf{x},\mathbf{y},t)\exp(i\omega t)dt$, is applied to Eq. (3.1), then

Eq. (3.1) becomes

$$[(\omega+i\varepsilon)^2\delta_{li}+C^0_{klij}+\frac{\partial}{\partial x_k}\gamma_{klij}(\mathbf{x})\frac{\partial}{\partial x_j}]G_{i\alpha}(\mathbf{x},\mathbf{y})=\delta^3(\mathbf{x}-\mathbf{y})\delta_{l\alpha}. \tag{3.3}$$

The mean solution $\langle\mathbf{G}\rangle$ to Eq. (3.3) is expressed in the form of an integral equation

$$\langle G_{i\alpha}(\mathbf{x},\mathbf{y})\rangle=G^0_{i\alpha}(\mathbf{x},\mathbf{y})+\int\int G^0_{i\beta}(\mathbf{x},\mathbf{z})m_{\beta j}(\mathbf{z},\mathbf{z'})\langle G_{j\alpha}(z',y)\rangle d^3zd^3z', \tag{3.4}$$

where $\mathbf{G}^0$ is the solution to Eq. (3.3) when $\gamma=0$, the tensor $m_{\beta j}$ is defined as the self energy operator. The spatial Fourier transform of the self-energy is defined as

$$-\sigma_{\beta j}(p)\delta^3(\mathbf{p}-\mathbf{s})=\frac{2}{(2\pi)^3}\int\int d^3xd^3y\exp\{-i\mathbf{p}\cdot x+i\mathbf{s}\cdot y\}m_{\beta j}(x,y). \tag{3.5}$$

Eq. (3.4) is called the Dyson equation [7].

The Dyson equation is easily solved in the spatial Fourier transform domain,

$$\begin{aligned}\langle\tilde{\mathbf{G}}(\mathbf{p})\rangle &= \left[\left[\tilde{\mathbf{G}}^0(\mathbf{p})\right]^{-1}+\sigma(\mathbf{p})\right]^{-1}\\ &= \left[\mathbf{I}(\omega+i\varepsilon)^2-\mathbf{p}\cdot\mathbf{C}^0\cdot\mathbf{p}+\sigma(\mathbf{p})\right]^{-1},\end{aligned} \tag{3.6}$$

where $\tilde{\mathbf{G}}(\mathbf{p})$ and $\sigma(\mathbf{p})$ are the spatial Fourier transforms of the Green function $\mathbf{G}$ and the self energy $\mathbf{m}$. The effective wave number $\mathbf{p}$ is the wave number of the mean Green's function, the value of $\mathbf{p}$ at which $\langle\mathbf{G}\rangle$ is singular. The solutions $\mathbf{p}$ can be determined from algebraic equation

$$\det\left[\mathbf{I}(\omega+i\varepsilon)^2-\mathbf{p}\cdot\mathbf{C}^0\cdot\mathbf{p}+\sigma(\mathbf{p})\right]=0. \tag{3.7}$$

The problem of determining the mean response reduces to that of determining the self-energy. The real part of $\mathbf{p}$ is inversely proportional to the wave speed and the imaginary part is proportional to the attenuation coefficient α.

3.2 Bethe-Salpeter Equation and Green's Function Covariance

It is not sufficient to calculate the mean response $\langle \mathbf{G} \rangle$ for diffuse field measurements in which signals are squared before averaging. The Green's function covariance is defined as $\langle G_{\alpha\beta}(\mathbf{x}, \mathbf{x}', \omega) G^{*}_{ij}(\mathbf{y}, \mathbf{y}', \omega + \Omega) \rangle$, in which the asterisk implies $\omega + \Omega$ as well as the complex conjugate. Note that that covariance is a measure of how much two variables change together (the variance is a special case of the covariance when two variables are identical.) The spatial Fourier transform of the Green's function covariance $\langle \mathbf{G}\mathbf{G}^{*} \rangle$ is defined by

$$
\begin{aligned}
{}^{\mathbf{p}}_{\mathbf{p}'}\,{}^{\alpha}_{i}H^{\beta}_{j}\,{}^{\mathbf{s}}_{\mathbf{s}'}\,\delta^{3}(\mathbf{p}+\mathbf{s}'-\mathbf{s}-\mathbf{p}') = \frac{1}{(2\pi)^{6}} \int d^{3}x d^{3}x' d^{3}y d^{3}y' \langle G_{\alpha\beta}(\mathbf{x},\mathbf{x}') G^{*}_{ij}(\mathbf{y},\mathbf{y}') \rangle \\
\times \exp(-i\mathbf{p}\cdot\mathbf{x} + i\mathbf{s}\cdot\mathbf{x}' + i\mathbf{p}'\cdot\mathbf{y} - i\mathbf{s}'\cdot\mathbf{y}'), \qquad (3.8)
\end{aligned}
$$

where the delta function is a consequence of the assumed statistical homogeneity of the medium. It is conventional to employ the delta-function and a change of variables $\mathbf{p}'$=$\mathbf{p}$+$\boldsymbol{\Delta}$, and consider only the three wavevector dependent quantity.

The covariance is governed by the solution of the Bethe-Salpeter equation

$$
\begin{aligned}
{}^{\mathbf{p}}_{\mathbf{p}+\boldsymbol{\Delta}}\,{}^{\alpha}_{i}H^{\beta}_{j}\,{}^{\mathbf{s}}_{\mathbf{s}+\boldsymbol{\Delta}} &= {}^{\alpha}_{i}\Gamma^{\beta}_{j}\,{}^{\mathbf{s}}_{\mathbf{s}+\boldsymbol{\Delta}}\delta^{3}(\mathbf{p}-\mathbf{s}) \\
&+ \int d^{3}s\, {}^{\alpha}_{i}\Gamma^{\gamma}_{k}\,{}^{\mathbf{p}}_{\mathbf{p}+\boldsymbol{\Delta}}\,{}^{\mathbf{p}}_{\mathbf{p}+\boldsymbol{\Delta}}\,{}^{\gamma}{}_{k}K^{\delta}_{l}\,{}^{\mathbf{s}}_{\mathbf{s}+\boldsymbol{\Delta}}\,{}^{\mathbf{s}}_{\mathbf{s}+\boldsymbol{\Delta}}\,{}^{\delta}{}_{l}H^{\beta}_{j}\,{}^{\mathbf{s}}_{\mathbf{s}+\boldsymbol{\Delta}}, \qquad (3.9)
\end{aligned}
$$

where the double mean field Green's function $\boldsymbol{\Gamma}$ is ${}^{\alpha}_{i}\Gamma^{\gamma}_{k}\,{}^{\mathbf{s}}_{\mathbf{s}+\boldsymbol{\Delta}} = \langle G_{\alpha\gamma}(\mathbf{s}) \rangle \langle G^{*}_{ik}(\mathbf{s}+\boldsymbol{\Delta}) \rangle$.

It describes the propagation of the square of the mean field. The operator $\mathbf{K}$, known as the intensity operator, is approximated by (often called the ladder approximation because of the shapes of the corresponding Feynman diagrams)

$$\,^{\mathbf{p}}_{\mathbf{p}+\boldsymbol{\Delta}}\,{}^{\gamma}_{k}K^{\delta}_{l}\,{}^{\mathbf{s}}_{\mathbf{s}+\boldsymbol{\Delta}} = p_{\beta}s_{\alpha}(p_i+\Delta_i)(s_j+\Delta_j)\tilde{\Lambda}(\mathbf{p}-\mathbf{s})^{\gamma\beta\alpha\delta}_{kijl}. \tag{3.10}$$

The Bethe-Salpeter equation can be expanded in a multiple scattering series,

$$\begin{aligned}\,^{\mathbf{p}}_{\mathbf{p}+\boldsymbol{\Delta}}\,{}^{\alpha}_{i}H^{\beta}_{j}\,{}^{\mathbf{s}}_{\mathbf{s}+\boldsymbol{\Delta}} &\approx {}^{\alpha}_{i}\Gamma^{\beta}_{j}\,{}^{\mathbf{s}}_{\mathbf{s}+\boldsymbol{\Delta}}\delta^3(\mathbf{p}-\mathbf{s})\\ &\quad + {}^{\alpha}_{i}\Gamma^{\gamma}_{k}\,{}^{\mathbf{p}}_{\mathbf{p}+\boldsymbol{\Delta}}\,{}^{\mathbf{p}}_{\mathbf{p}+\boldsymbol{\Delta}}\,{}^{\gamma}_{k}K^{\delta}_{l}\,{}^{\mathbf{s}}_{\mathbf{s}+\boldsymbol{\Delta}}\,{}^{\mathbf{s}}_{\mathbf{s}+\boldsymbol{\Delta}}\,{}^{\delta}_{l}\Gamma^{\beta}_{j}\,{}^{\mathbf{s}}_{\mathbf{s}+\boldsymbol{\Delta}} + o(k^2),\end{aligned} \tag{3.11}$$

where the expansion has been truncated to include only single scattering events. The first term of the right side of Eq. (3.11) indicates the coherent propagation of covariance from source to receiver. The second term describes a coherent propagation at wavevector $\mathbf{s}$ followed by a scattering to wavevector $\mathbf{p}$.

3.3 Sources, Receivers, Mean and Mean Square Signals

The field produced by a source transducer is written as a convolution in space and time between the Green's function of the medium and the source

$$\Psi^{S}_{\beta}(\mathbf{x},t) = \int G_{\beta\alpha}(\mathbf{x}',\mathbf{x},t)B_{\alpha}(\mathbf{x}') \otimes S(t)d^3x', \tag{3.12}$$

where $B_{\alpha}(\mathbf{x})S(t)$ represents a body force which is distributed in space, time and direction. The operator $\otimes$ indicates a temporal convolution. The spatial and temporal

Fourier transform of the ensemble average of this response is

$$\begin{aligned}\langle \Psi^S_\alpha(\mathbf{p},\omega)\rangle &= \int d^3r \langle G_{\alpha\beta}(\mathbf{r},t)\rangle \exp\{-i\mathbf{p}\cdot\mathbf{r}\}\frac{d^3x'}{(2\pi)^{3/2}}B_\beta(\mathbf{x}')\\ &\times \exp\{-i\mathbf{p}\cdot\mathbf{x}\}\otimes S(t)\exp\{i\omega t\}dt\\ &= \langle \tilde{G}_{\alpha\beta}(\mathbf{p},\omega)\rangle \tilde{B}_\beta(\mathbf{p})S(\omega). \end{aligned} \tag{3.13}$$

The Fourier transformed average field is given by a simple product of the Fourier transform of the source function and the average Green's function.

The response of the receiver at time t to a point source in direction β at time zero and position $\mathbf{x}$ is given by the convolution with the Green's function of the medium as

$$\Psi^R_\beta(\mathbf{x},t) = \int R(t)\otimes A_\alpha(\mathbf{x}')G_{\alpha\beta}(\mathbf{x}',\mathbf{x},t)d^3x', \tag{3.14}$$

where $A_\alpha(\mathbf{x})R(t)$ is defined as the receiver sensitivity distribution function. The averaged response of the receiver after taking the Fourier transform can be written as

$$\begin{aligned}\langle \Psi^R_\beta(\mathbf{p},\omega)\rangle &= \int d^3r \langle G_{\alpha\beta}(\mathbf{r},t)\rangle \exp\{i\mathbf{p}\cdot\mathbf{r}\}\frac{d^3x'}{(2\pi)^{3/2}}B_\beta(\mathbf{x}')\\ &\times \exp\{i\mathbf{p}\cdot\mathbf{x}\}\otimes S(t)\exp\{i\omega t\}dt\\ &= \langle \tilde{G}_{\beta\alpha}(\mathbf{p},\omega)\rangle \tilde{A}_\alpha(\mathbf{p})R(\omega). \end{aligned} \tag{3.15}$$

If the field produced by the source is detected by the receiver, the resulting signal $\phi(t)$ is given by the following convolution

$$\phi(t) = \int\int R(t)\otimes A_\beta(\mathbf{x})G_{\beta\alpha}(\mathbf{x},\mathbf{x}',t)B_\alpha(\mathbf{x}')\otimes S(t)d^3xd^3x'. \tag{3.16}$$

The position of the receiver or source is implicit in the factors $A_\beta(\mathbf{x})$ and $B_\alpha(\mathbf{x}')$, which have their chief support in the vicinity of those respective transducers. This expression defines the “signal” from which the mean and mean square are taken. As the source and receiver characteristics are nonstochastic, the mean signal is obtained from Eq. (3.16) simply by replacing $\mathbf{G}$ with $\langle\mathbf{G}\rangle$. Diffuse fields are typically analyzed by considering the square of the signal. The square of the signal given in Eq. (3.16)($\langle\phi^2(t)\rangle$=$\Phi(t)$) is transformed temporally and re-expressed in terms of the receiver and source characteristics and Green’s function covariance as

$$\begin{aligned}\Phi(\Omega) = \int & d^3x d^3x' d^3y d^3y' \frac{d\omega}{2\pi} R(\omega) S(\omega) R^*(\omega+\Omega) S^*(\omega+\Omega) \\ & \times A_\alpha(\mathbf{x}) A_i(\mathbf{y}) B_\beta(\mathbf{x}') B_j(\mathbf{y}') \langle G_{\alpha\beta}(\mathbf{x},\mathbf{x}') G^*_{ij}(\mathbf{y},\mathbf{y}')\rangle, \qquad (3.17)\end{aligned}$$

where the covariance of the Green’s function can be expressed in terms of its (12-fold) spatial inverse Fourier transform

$$\begin{aligned}\langle G_{\alpha\beta}(\mathbf{x},\mathbf{x}') G^*_{ij}(\mathbf{y},\mathbf{y}')\rangle = \frac{1}{(2\pi)^6} \int & d^3p d^3p' d^3s d^3s' \, {}^{\mathbf{p}}_{\mathbf{p}+\boldsymbol{\Delta}}{}^{\alpha}_{i} H^{\alpha}_{j}{}^{\mathbf{s}}_{\mathbf{s}+\boldsymbol{\Delta}} \delta^3(\mathbf{p}+\mathbf{s}'-\mathbf{s}-\mathbf{p}) \\ & \times \exp(i\mathbf{p}\cdot\mathbf{x} - i\mathbf{s}\cdot\mathbf{x}' - i\mathbf{p}'\cdot\mathbf{y} + i\mathbf{s}'\cdot\mathbf{y}'). \qquad (3.18)\end{aligned}$$

Substituting Eq. (3.18) into Eq. (3.17), and performing the integration over space, Eq. (3.17) can be reexpressed as

$$\begin{aligned}\Phi(\Omega) = \int & \frac{d\omega}{2\pi} d^3p d^3s d^3\boldsymbol{\Delta} \tilde{A}_\alpha(\mathbf{p}) \tilde{A}^*_i(\mathbf{p}+\boldsymbol{\Delta}) \tilde{B}_\beta(\mathbf{s}) \tilde{B}^*_j(\mathbf{s}+\boldsymbol{\Delta}) \\ & \times {}^{\mathbf{p}}_{\mathbf{p}+\boldsymbol{\Delta}}{}^{\alpha}_{i} H^{\alpha}_{j}{}^{\mathbf{s}}_{\mathbf{s}+\boldsymbol{\Delta}} \, R(\omega) S(\omega) R^*(\omega+\Omega) S^*(\omega+\Omega). \qquad (3.19)\end{aligned}$$

This expression characterizes the mean square signal (in the frequency domain) in terms of the transducer properties and the scattering characteristics of the medium.

3.4 Singly Scattered Response (SSR)

Substituting the multiple scattering series of Eq. (3.11) into Eq. (3.19) for Φ gives a multiple scattering expression for the mean square signal. The zeroeth order term of the mean of the square, $\Phi^0(\Omega)$, which is the first term of Eq. (3.19) vanishes, while the first order term in powers of $\mathbf{K}$ can be written as

$$\Phi^1(\Omega) = \int \frac{d\omega}{2\pi} dpdsd\Delta [\tilde{A}_\alpha(\mathbf{p})\langle \tilde{G}_{\alpha\beta}(\mathbf{p})\rangle R(\omega)][\tilde{A}_i(\mathbf{p}+\boldsymbol{\Delta})\langle \tilde{G}_{ij}(\mathbf{p}+\boldsymbol{\Delta})\rangle R(\omega+\Omega)]^*$$
$$\times {}^{\mathbf{p}}_{\mathbf{p}+\boldsymbol{\Delta}}{}^{\beta}_{j}K^{\gamma}_{k}{}^{\mathbf{s}}_{\mathbf{s}+\boldsymbol{\Delta}} [\tilde{B}_\tau(\mathbf{s})\langle \tilde{G}_{\gamma\tau}(\mathbf{s})\rangle S(\omega)][\tilde{B}_l(\mathbf{s}+\boldsymbol{\Delta})\langle \tilde{G}_{kl}(\mathbf{s}+\boldsymbol{\Delta})\rangle S(\omega+\Omega)]^*. \tag{3.20}$$

The quantities in square brackets [ ] can be written as the Fourier transform of the fields Ψ^R and Ψ^S

$$\begin{aligned}
\Phi^1(\Omega) = & \int \frac{d\omega}{2\pi} d^3p d^3s d^3\boldsymbol{\Delta}\, {}^{\mathbf{p}}_{\mathbf{p}+\boldsymbol{\Delta}}{}^{\beta}_{j}K^{\gamma}_{k}{}^{\mathbf{s}}_{\mathbf{s}+\boldsymbol{\Delta}} \\
& \times \left[\int \langle \Psi^R_\beta(\mathbf{x},t)\rangle \frac{dtd^3x}{(2\pi)^{\frac{3}{2}}} \exp\{i\mathbf{p}\cdot\mathbf{x} + i\omega t\}\right] \\
& \times \left[\int \langle \Psi^R_j(\mathbf{y},u)\rangle \frac{dud^3y}{(2\pi)^{\frac{3}{2}}} \exp\{-i(\mathbf{p}+\boldsymbol{\Delta})\cdot\mathbf{y} + i(\omega+\Omega)u\}\right] \\
& \times \left[\int \langle \Psi^S_\gamma(\mathbf{x}',t')\rangle \frac{dt'd^3x'}{(2\pi)^{\frac{3}{2}}} \exp\{i\mathbf{s}\cdot\mathbf{x}' + i\omega t'\}\right] \\
& \times \left[\int \langle \Psi^S_k(\mathbf{y}',u')\rangle \frac{du'd^3y'}{(2\pi)^{\frac{3}{2}}} \exp\{-i(\mathbf{s}+\boldsymbol{\Delta})\cdot\mathbf{y}' + i(\omega+\Omega)u'\}\right].
\end{aligned} \tag{3.21}$$

After making the variable changes

$$\mathbf{x} = \mathbf{X} + \xi/2, \mathbf{y} = \mathbf{X} - \xi/2, t = T + \tau/2, t = T - \tau/2,$$
$$\mathbf{x} = \mathbf{X} + \xi/2, \mathbf{y} = \mathbf{X} - \xi/2, t = T + \tau/2, t = T - \tau/2, \tag{3.22}$$

$\Phi^1(\Omega)$ is given by

$$\begin{aligned}\Phi^1(\Omega) = &\int \frac{d\omega}{(2\pi)^7} d^3p d^3s d^3\boldsymbol{\Delta}\, {}^{\mathbf{p}}_{\mathbf{p}+\boldsymbol{\Delta}}\, {}^{\beta}_{j}K^{\gamma}_{k}\, {}^{\mathbf{s}}_{\mathbf{s}+\boldsymbol{\Delta}} \\ &\times \int d^3X dT d^3\xi d\tau \langle \Psi^R_\beta(\mathbf{X}+\xi/2, T+\tau/2)\rangle \, \langle \Psi^R_j(\mathbf{X}-\xi/2, T-\tau/2)\rangle \\ &\times \exp\{i\tau(\omega+\Omega/2) + i\xi\cdot(\mathbf{p}+\boldsymbol{\Delta}/2) - i\Omega T - i\boldsymbol{\Delta}\cdot\mathbf{X}\} \\ &\times \int d^3X' dT' d^3\xi' d\tau' \langle \Psi^S_\gamma(\mathbf{X}'+\xi'/2, T'+\tau'/2)\rangle \, \langle \Psi^S_k(\mathbf{X}'-\xi'/2, T'-\tau'/2)\rangle \\ &\times \exp\{i\tau'(\omega+\Omega/2) + i\xi'\cdot(\mathbf{s}+\boldsymbol{\Delta}/2) - i\Omega T' - i\boldsymbol{\Delta}\cdot\mathbf{X}'\}. \qquad (3.23)\end{aligned}$$

The integrations over ξ, τ, ξ' and τ' can be done by defining two 4-fold Wigner transforms as

$$\begin{aligned}W^S_{\gamma k}(\mathbf{X}, T, \mathbf{k}, \omega) = &\int \langle \Psi^S_\gamma(\mathbf{X}+\xi/2, T+\tau/2)\rangle \, \langle \Psi^S_k(\mathbf{X}-\xi/2, T-\tau/2)\rangle \\ &\times \exp\{-i\mathbf{k}\cdot\xi + i\omega\tau\} d^3\xi d\tau, \\ W^R_{\beta j}(\mathbf{X}, T, \mathbf{k}, \omega) = &\int \langle \Psi^R_\beta(\mathbf{X}+\xi/2, T+\tau/2)\rangle \, \langle \Psi^R_j(\mathbf{X}-\xi/2, T-\tau/2)\rangle \\ &\times \exp\{+i\mathbf{k}\cdot\xi + i\omega\tau\} d^3\xi d\tau. \qquad (3.24)\end{aligned}$$

Eqs. (3.24) represent spatial and temporal generalizations of the more well known temporal Wigner transform widely utilized in signal processing, and other applications such as imaging, optics, and so on. $\mathbf{W}$ indicates a distribution in space and time $\mathbf{X}$, T of spectral energy density as a function of wavevector $\mathbf{k}$ and frequency ω.

Using the definitions in Eqs. (3.24), the singly-scattered response in Eq. (3.23) is given by

$$\begin{aligned}\Phi^1(\Omega) = &\int \frac{d\omega}{(2\pi)^7} d^3p d^3s d^3\boldsymbol{\Delta}\, {}^{\mathbf{p}}_{\mathbf{p}+\boldsymbol{\Delta}}\,{}^{\beta}_{j}K^{\gamma}_{k}\,{}^{\mathbf{s}}_{\mathbf{s}+\boldsymbol{\Delta}} \\ &\times \int d^3X dT W^R_{\beta j}(\mathbf{X}, T, \mathbf{p}+\boldsymbol{\Delta}/2, \omega+\Omega/2) \exp\{-i\Omega T - i\boldsymbol{\Delta}\cdot\mathbf{X}\} \\ &\times \int d^3X' dT' W^S_{\gamma k}(\mathbf{X}', T', \mathbf{s}+\boldsymbol{\Delta}/2, \omega+\Omega/2) \exp\{-i\Omega T' + i\boldsymbol{\Delta}\cdot\mathbf{X}'\}.\end{aligned} \tag{3.25}$$

At this point it is necessary to assume that the dependence of $\mathbf{K}$ on the $\boldsymbol{\Delta}$ and Ω is negligible. This allows the $\boldsymbol{\Delta}$ integration, and the integation over Ω entailed in the inverse Fourier transform to be done immediately. After changing the variables by shifting ω by $\Omega/2$ and p, q by $\boldsymbol{\Delta}/2$, Eq. (3.25) is given by

$$\begin{aligned}\Phi^1(T) = &\int \frac{d\omega}{(2\pi)^4} d^3p d^3s d^3X dT' \\ &\times W^R_{\beta j}(\mathbf{X}, T-T', \mathbf{p}, \omega)\, {}^{\mathbf{p}}_{\mathbf{p}}\,{}^{\beta}_{j}K^{\gamma}_{k}\,{}^{\mathbf{s}}_{\mathbf{s}}\, W^S_{\gamma k}(\mathbf{X}, T', \mathbf{s}, \omega).\end{aligned} \tag{3.26}$$

It can be seen that the singly scattered contribution is a convolution in time and space of the product of the Wigner distributions of the beam pattern of the source and receiver, mediated by the scattering strength $\mathbf{K}$ from wave vector $\mathbf{p}$ to wave vector $\mathbf{s}$. The Wigner distributions that enter into this description are the Wigner transforms of the coherent fields associated with source and receiver, the fields that would be present if the source and receiver were placed in a medium described by the average Green's function.

3.5 Wigner Transform of a Piston Transducer

The square of the variance of the signal obtained from a typical ultrasonic C-scan is a typical diffuse ultrasonic result. In such experiments, the signals are collected at various positions of the transducer and the scattering from the local depth is analyzed to extract the microstructural information by examining the statistics of the signals. Eq. (3.26) can be utilized to model the variance of the signal at the focal region [24]. An expression of the singly-scattered response (SSR) for polycrystalline materials was previously derived by Thompson and Gray [27]. In analogy with the model developed by Thompson and Gray, Eq. (3.26) represents an expression for single scattering.

Eq. (3.26) applies for a specific case of measurement, in which the same transducer acts as both source and receiver. Because the focus here is on the longitudinal-to-longitudinal SSR, the Wigner transform of the receiver and the source is simplified. The longitudinal component of the mean Green's function in space and time is given by [7]

$$\langle \mathbf{G}(\mathbf{x},\mathbf{x}',t)\rangle = -\frac{\exp[-\alpha_L|\mathbf{x}-\mathbf{x}'|]}{4\pi c_l^2(|\mathbf{x}-\mathbf{x}'|)}\delta(t-\frac{|\mathbf{x}-\mathbf{x}'|}{c_L})\hat{\mathbf{p}}\hat{\mathbf{p}}, \tag{3.27}$$

where α_L is the longitudinal attenuation coefficient. The body force is assumed to be a Gaussian pulse in space and is given by

$$B_\alpha(x) = B_0\delta(z)\exp\left[-\frac{x^2+y^2}{w_0^2}\right]\hat{\mathbf{n}}_\alpha, \tag{3.28}$$

where w_0 is the effective transducer radius, B_0 is the force per unit area and $\hat{n}_\alpha$ is the unit normal to the transducer face. The source is also assumed to be a Gaussian pulse in time such that

$$S(t) = \frac{1}{\sigma\sqrt{\pi}}\exp\left[i\omega_0 t-\frac{t^2}{\sigma^2}\right], \tag{3.29}$$

where ω_0 is the center excitation frequency and σ is the width of the pulse.

Then the temporal convolution becomes

$$\langle G_{\beta\alpha}(\mathbf{x},\mathbf{x}',t)\rangle \otimes S(t) = -\frac{\exp\left(i\omega_0 t - (\frac{t}{\sigma})^2\right)}{\sigma\sqrt{\pi}4\pi c_L^2}\frac{\exp\left[(-ik_0 + \frac{2t}{\sigma^2 c_L})|\mathbf{x}-\mathbf{x}'| - \frac{|\mathbf{x}-\mathbf{x}'|^2}{\sigma^2 c_L^2}\right]}{|\mathbf{x}-\mathbf{x}'|}$$
$$\times \exp[-\alpha_L|\mathbf{x}-\mathbf{x}'|]\hat{p}_\beta\hat{p}_\alpha. \tag{3.30}$$

Within the context of the paraxial approximation, the quantity $|\mathbf{x}-\mathbf{x}'|$ is expanded to first order in the phase term as $((z-z') + \{(x-x')^2 + (y-y')^2\}/2z)$ and to zeroeth order in the amplitude term as $(z-z')$. Thus, using the convolution in space, the mean source field is simplified as

$$\langle \Psi_\beta(\mathbf{x},t)\rangle = -\frac{B_0\exp(i\omega_0 t - (\frac{t}{\sigma})^2)}{\sigma\sqrt{\pi}4\pi c_L^2}\exp\left[-\alpha_L z + \frac{z(2c_L t - z)}{\sigma^2 c_L^2}\right]\frac{\lambda_0\omega_0}{w(z)}$$
$$\times\exp\left[-ik_0 z - \frac{r^2}{w^2(z)} - i\frac{\pi}{\lambda_0}\frac{r^2}{R(z)} + i\frac{\pi}{2} + i\Psi_0(z)\right]\hat{p}_\beta(\hat{\mathbf{p}}\cdot\hat{\mathbf{n}}), \tag{3.31}$$

where $w_z = w_0\left[1 + (\frac{\lambda_0 z}{\pi w_0^2})^2\right]^{1/2}$ is the Gaussian beam width, $R_z = z + (\frac{\pi w_0^2}{\lambda_0})^2\frac{1}{z}$ is the radius of curvature of the wavefront and $\Psi_0(z) = \tan^{-1}(\frac{\lambda_0 z}{\pi w_0^2})$ is the excess phase. The mean source field given in Eq. (3.31) can also be written in the form

$$\langle \Psi_\beta^S(\mathbf{r},z,t)\rangle = A(\mathbf{r},z,t)\exp\{i\Theta(\mathbf{r},z,t)\}\hat{p}_\beta(\hat{\mathbf{p}}\cdot\hat{\mathbf{n}}), \tag{3.32}$$

where $r^2{=}x^2+y^2$. The amplitude $A(\mathbf{r},z,t)$ and the phase $\Theta(\mathbf{r},z,t)$ of the source field are given as

$$A(\mathbf{r},z,t) = -\frac{B_0\exp\left(-\frac{-t^2}{\sigma^2}\right)}{\sigma\sqrt{\pi}4\pi c_L^2}\frac{\lambda_0 w_0}{w(z)}\exp\left[-\frac{r^2}{w^2(z)} - \alpha_L z + \frac{z(2c_L t - z)}{\sigma^2 c_L^2}\right],$$
$$\Theta(\mathbf{r},z,t) = \omega_0 t - k_0 z - \frac{\pi}{\lambda_0}\frac{r^2}{R(z)} + \frac{\pi}{2} + \Psi_0(z). \tag{3.33}$$

The Wigner transform of $\langle \Psi_\beta^S \rangle$ can be approximated by [37]

$$W(\mathbf{x}, t, \mathbf{k}, \omega) = (2\pi)^4 |A(\mathbf{x}, t)|^2 \delta^3(\mathbf{k} - \bigtriangledown_{\mathbf{x}} \Theta(\mathbf{x}, t)) \delta \left(\omega - \frac{\partial}{\partial t} \Theta(\mathbf{x}, t) \right). \tag{3.34}$$

Thus the space-time Wigner transform of the mean transducer field becomes

$$\begin{aligned} W_{\gamma k}(\mathbf{x}, \mathbf{k}, t, \omega) = (2\pi)^4 & \left(\frac{B_0}{\sigma \sqrt{\pi} 4\pi c_L^2} \frac{\lambda_0 \omega_0}{w(z)} \right)^2 \exp \left[-2\alpha_L z + 2z \frac{(2c_L t - z)}{\sigma^2 c_L^2} - 2 \frac{r^2}{w^2(z)} \right] \\ & \times \exp \left[-2 \left(\frac{t}{\sigma} \right)^2 \right] \delta(\omega - \omega_0) \delta^2 \left(\mathbf{k}_r + \frac{2\pi}{\lambda_0} \frac{r}{R(z)} \right) \\ & \times \delta \left(k_z + k_0 - \frac{\lambda_0}{\pi} \frac{1}{w^2(z)} - \frac{\pi}{\lambda_0} r^2 \frac{1}{R^2(z)} \left(1 - \left(\frac{\pi w_0^2}{\lambda_0 z} \right)^2 \right) \right) (\hat{\mathbf{k}} \cdot \hat{\mathbf{n}})^2 \hat{k}_\gamma \hat{k}_k. \end{aligned} \tag{3.35}$$

The terms $\frac{2\pi}{\lambda_0} \frac{r}{R(z)}$ and $-\frac{\lambda_0}{\pi} \frac{1}{w^2(z)} - \frac{\pi}{\lambda_0} r^2 \frac{1}{R_2(z)} \left(1 - \left(\frac{\pi w_0^2}{\lambda_0 z} \right)^2 \right)$ in the delta function are assumed negligible in comparison with k_0. This assumption implies that all energy is primarily in the $k_z = k_0$ direction, which is along the transducer axis ($|\mathbf{k}|^2 = k_r^2 + k_z^2 \cong k_z^2$). Finally the longitudinal component of the Wigner transform of a piston transducer becomes

$$\begin{aligned} W_{\gamma k}^S(\mathbf{x}, \mathbf{k}, t, \omega) = (2\pi)^4 & \left(\frac{B_0}{\sigma \sqrt{\pi} 4\pi c_L^2} \frac{\lambda_0 w_0}{w(z)} \right)^2 \exp \left[-2\alpha_L z + 2z \frac{(2c_L t - z)}{\sigma^2 c_L^2} - 2 \frac{r^2}{w^2(z)} \right] \\ & \times \exp \left[-2 \left(\frac{t}{\sigma} \right)^2 \right] \delta(\omega - \omega_0) \delta^3(\mathbf{k} + k_0) (\hat{\mathbf{k}} \cdot \hat{\mathbf{n}})^2 \hat{k}_\gamma \hat{k}_k. \end{aligned} \tag{3.36}$$

Eq. (3.26) describes the distribution of longitudinal energy in space, time, frequency and wave vector resulting from a piston transducer.

3.6 Singly Scattered Response (SSR) from a Piston Transducer

By assuming that the spatial and the tensorial components of the covariance of moduli are independent, $\tilde{\Lambda}(\mathbf{p})^{\alpha\beta\gamma\delta}_{lmjk} = \Xi^{\alpha\beta\gamma\delta}_{lmjk}\tilde{\eta}(\mathbf{p})$, where $\tilde{\eta}(\mathbf{p})$ is the spatial Fourier transform of the two-point spatial correlation function. In this case, the intensity operator given in Eq. (3.10) is written as

$$\begin{aligned} {}^{\mathbf{p}\beta}_{\mathbf{p}j}K^{\gamma\mathbf{s}}_{k\,\mathbf{s}} &\approx \eta(\mathbf{p}-\mathbf{s})\mathbf{p}_\alpha\mathbf{s}_\delta\mathbf{p}_l\mathbf{s}_m\Xi^{\alpha\delta\beta\gamma}_{lmjk} \\ &= p^2s^2\tilde{\eta}(p\hat{\mathbf{p}}-s\hat{\mathbf{s}})\hat{p}_\alpha\hat{s}_\delta\hat{p}_l\hat{s}_m\Xi^{\alpha\delta\beta\gamma}_{lmjk}. \end{aligned} \tag{3.37}$$

The singly-scattered response (SSR) then becomes

$$\begin{aligned} \Phi^1(t) = {} & (2\pi)^8\left(\frac{B_0\lambda_0}{\sigma\sqrt{\pi}4\pi c_L^2}\right)^4\int\frac{d\omega}{(2\pi)^6}\left[\left(\frac{\omega_0}{c_L}\right)^4\tilde{\eta}\left(\frac{\omega_0}{c_L}\hat{\mathbf{p}}-\frac{\omega_0}{c_L}\hat{\mathbf{s}}\right)\hat{p}_\alpha\hat{s}_\delta\hat{p}_l\hat{s}_m\Xi^{\alpha\delta\beta\gamma}_{lmjk}\right] \\ & \times\left(\frac{\omega_0}{w(z)}\right)^4\exp\left[-4\alpha_Lz+2z\frac{2c_L(t-t')-z}{\sigma^2c_L^2}+2z\frac{2c_Lt'-z}{\sigma^2c_L^2}-4\frac{r^2}{w^2(z)}\right] \\ & \times\exp\left[-2\frac{(t-t')^2}{\sigma^2}-2\frac{t'^2}{\sigma^2}\right]\delta^2(\hat{\mathbf{p}}+\hat{\mathbf{p}}_0)\hat{p}_\beta\hat{p}_j(\hat{\mathbf{p}}\cdot\hat{\mathbf{n}})^2\delta(\omega-\omega_0)\delta^2(\hat{\mathbf{s}}+\hat{\mathbf{s}}_0) \\ & \times\hat{s}_\gamma\hat{s}_k(\hat{\mathbf{s}}\cdot\hat{\mathbf{n}})^2\delta(\omega-\omega_0)d^2\hat{p}d^2\hat{s}d^3Xdt'. \end{aligned} \tag{3.38}$$

In diffuse backscatter measurements the angle between the propagation and scattered direction is π for a normal incidence pulse echo setup. Therefore, $\hat{\mathbf{p}}_0\cdot\hat{\mathbf{n}}$=1, $\hat{\mathbf{s}}_0\cdot\hat{\mathbf{n}} =$

1, $\hat{\mathbf{p}}_0 \cdot \hat{\mathbf{s}}_0$ = -1. Thus the SSR is

$$\Phi^1(t) = (2\pi)^2 (\frac{B_0 \lambda_0}{\sigma\sqrt{\pi} 4\pi c_L^2})^4 \int \left(\frac{\omega_0}{c_L}\right)^4 \tilde{\eta}(\theta_{p_0 s_0} = \pi) \left[\hat{p}_{0\beta}\hat{p}_{0j}\hat{p}_{0\alpha}\hat{p}_{0\delta}\hat{p}_{0l}\hat{p}_{0m}\hat{p}_{0\gamma}\hat{p}_{0k}\Xi^{\alpha\delta\beta\gamma}_{lmjk}\right] \\ \times \left(\frac{w_0}{w(z)}\right)^4 \exp\left[-4\alpha_L z + 4z\frac{c_L t - z}{\sigma^2 c_L^2} - 4\frac{r^2}{w^2(z)} - 2\frac{(t-t')^2}{\sigma^2} - 2\frac{t'^2}{\sigma^2}\right] d^3X dt', \tag{3.39}$$

where $\tilde{\eta}(\theta_{p_0 s_0}) = \tilde{\eta}(\frac{\omega}{c_L}\hat{\mathbf{p}}_0 - \frac{\omega}{c_L}\hat{\mathbf{s}}_0)$ and $\theta_{p_0 s_0}$ is the angle between the vector $\hat{\mathbf{p}}_0$ and $\hat{\mathbf{s}}_0$. The inner product is denoted in direct form as $\Xi^{\alpha\delta\beta\gamma}_{lmjk}\hat{p}_\alpha\hat{p}_l\hat{s}_\delta\hat{s}_m\hat{p}_\beta\hat{p}_j\hat{s}_\gamma\hat{s}_k = \Xi^{\cdots\hat{\mathbf{p}}\hat{\mathbf{p}}\hat{\mathbf{s}}\hat{\mathbf{s}}}_{\cdots\hat{\mathbf{p}}\hat{\mathbf{p}}\hat{\mathbf{s}}\hat{\mathbf{s}}}(\theta_{ps})$. Then the singly scattered response is written as

$$\Phi^1(t) = (2\pi)^2 (\frac{B_{0\lambda_0}}{\sigma\sqrt{\pi} 4\pi c_L^2})^4 \left[\left(\frac{\omega_0}{c_L}\right)^4 \tilde{\eta}(\pi)\Xi^{\cdots\hat{\mathbf{p}}\hat{\mathbf{p}}\hat{\mathbf{s}}\hat{\mathbf{s}}}_{\cdots\hat{\mathbf{p}}\hat{\mathbf{p}}\hat{\mathbf{s}}\hat{\mathbf{s}}}\right] \\ \times \int \left(\frac{w_0}{w(z)}\right)^4 \exp\left[-4\alpha_L z + 4z\frac{c_L t - z}{\sigma^2 c_L^2} - 4\frac{r^2}{w^2(z)} - 2\frac{(t-t')^2}{\sigma^2} - 2\frac{t'^2}{\sigma^2}\right] d^3X dt'. \tag{3.40}$$

The integration in the lateral dimensions, x and y, indicates the effect of scattering from a plane at depth z in the material. It is given by

$$\int_{-\infty}^{\infty}\int_{-\infty}^{\infty} \exp\left[-4\frac{x^2+y^2}{w^2(z)}\right] dxdy = \frac{\pi w^2(z)}{4}. \tag{3.41}$$

The temporal integration becomes

$$\int_{-\infty}^{\infty} \exp\left(-2\frac{(t-t')^2 + (t')^2}{\sigma^2}\right) dt' = \frac{\sigma\sqrt{\pi}}{2}\exp\left[-\frac{t^2}{\sigma^2}\right]. \tag{3.42}$$

Substituting Eq. (3.41) and Eq. (3.42) into Eq. (3.38), the SSR reduces to

$$\Phi^1(t) = \frac{B_0^4}{4\sqrt{\pi}\sigma^3\omega_0^4}\left[\frac{\pi}{2}\frac{\omega_0^4}{c_L^8}\tilde{\eta}(\pi)\Xi^{\cdots\hat{\mathbf{p}}\hat{\mathbf{p}}\hat{\mathbf{s}}\hat{\mathbf{s}}}_{\cdots\hat{\mathbf{p}}\hat{\mathbf{p}}\hat{\mathbf{s}}\hat{\mathbf{s}}}\right]\exp\left(-\frac{t^2}{\sigma^2}\right) \\ \times\int_0^\infty\left(\frac{\pi}{4}\frac{w_0^4}{w^2(z)}\right)\exp\left(-4\alpha_L z + 4z\frac{c_L t - z}{\sigma^2 c_L^2}\right)dz. \qquad (3.43)$$

In Eq. (3.43) σ, w_0 and B_0 can be obtained by calibrating and characterizing transducers through typical ultrasonic pulse-echo experiments (B_0 can be calculated from the amplitude of the reflected signal from the surface of the test sample).

The integrand in the Eq. (3.43) is related to the transducer beam model which is solved using a numerical integration method. The term in the square brackets $[\frac{\pi}{2}\frac{\omega_0^4}{c_L^8}\tilde{\eta}(\pi)\Xi^{\cdots\hat{\mathbf{p}}\hat{\mathbf{p}}\hat{\mathbf{s}}\hat{\mathbf{s}}}_{\cdots\hat{\mathbf{p}}\hat{\mathbf{p}}\hat{\mathbf{s}}\hat{\mathbf{s}}}(\pi)]$ is known as the diffuse backscatter coefficient, which depends on the microstructural properties of the material. Eq. (3.43) was the primary result of Ghoshal, et al. [24], a quantity that can be compared with the covariance of the backscattered signals obtained from diffuse backscatter experiment. The parameters given in Eq. (3.43) will be discussed later. In the following chapters, the SSR model given by Eq. (3.43) is modified to include the effects of lamellar duplex microstructure in pearlitic steel.

Chapter 4

Ultrasonic Backscatter from Lamellar Duplex Microstructure in Pearlitic Steel

In this chapter, a new singly-scattered model is proposed based on the previous SSR model given by Eq. (3.43) in chapter 3 for application to pearlitic wheel steel. In this case, the material is assumed to have a lamellar duplex microstructure within grains (pearlite phase) so that the dependence of ultrasonic backscatter on the duplex microstructure can be examined. This microstructure is characterized by alternating phases of cementite and ferrite as shown in Figure 4.1. The effects of the lamellar spacing d on ultrasonic backscatter are observed by comparing the spatial variance curves of the collected backscatter signals measured from the cross section of an unquenched wheel with that of a quenched wheel. The lamellar spacing within grains increases from the tread surface to deeper locations due to the non-uniform cooling rate. The model developed is used to estimate the lamellar spacing as a function of depth and the results agree well with spacing estimates from optical microscopy.

4.1 Theoretical Model

One of the primary results in chapter 3 was a time-dependent spatial variance model for a collection of ultrasonic backscatter signals captured at various positions on a sample. The spatial variance defines the statistical expectation regarding the variability of ultrasonic measurements made from different positions on the sample and it is directly related to the microstructure. That work analyzed results from a typical diffuse ultrasonic backscatter experiment for which the signals that are collected at each position are not in phase with one another such that they may be considered diffuse (or incoherent). However, the lack of coherency does not restrict the results to a particular limit of the full multiple scattering expansion. To obtain a tractable solution for comparison with experiments, the initial multiple scattering model described in chapter 3 was further limited under an assumption of single scattering from the microstructure resulting in the singly-scattered response (SSR). In this case, the measurements are restricted to early times (or focused transducer beams) in contrast to measurements that occur at the opposite end of the scattering regime that lie in the diffusion limit. Major aspects of the SSR model are next described here briefly for completeness. The Wigner distribution of the transducer displacement profile is used to model the beam pattern of an ultrasonic transducer through a liquid-solid interface. Then the beam is assumed as a simple Gaussian to simplify the derivation. The final expression of the SSR given by the Eq. (3.43) is written as [46]

$$\begin{aligned}\Phi^{LL}(t) = V_{max}^2 \frac{\pi}{8\sqrt{2}} \left(\frac{w(z_F)}{w_0}\right)^2 \left(\frac{\rho_L c_L^2}{\rho_f c_f^2} \frac{T_{fL} T_{Lf}}{R_{ff} D(\omega_0)}\right)^2 \\ \times \exp(4\alpha_f z_F - 4\alpha_f z_f) \left[\frac{\pi}{2} \frac{\omega_0^4}{c_L^8} \tilde{\eta}^{LL}(\theta_{ps}, k_L) \Xi_{\cdots \hat{\mathbf{p}}\hat{\mathbf{p}}\hat{\mathbf{s}}\hat{\mathbf{s}}}^{\cdots \hat{\mathbf{p}}\hat{\mathbf{p}}\hat{\mathbf{s}}\hat{\mathbf{s}}}(\theta_{ps})\right] \\ \times \exp\left(-\frac{t^2}{\sigma^2}\right) \int_0^\infty \frac{w_0^2}{w^2(z)} \exp\left[-4\alpha_L z - \frac{4z(z - tc_L)}{\sigma^2 c_L^2}\right] dz. \qquad (4.1)\end{aligned}$$

Eq. (4.1) connects the recent scattering theory with experimental results involving the fluid-solid interface. This SSR model can be divided into three major portions: The first line of Eq. (4.1) shows the experimental parameters associated with the transducer, the fluid and the bulk properties of the sample. Here, ρ_L and c_L are the density and the longitudinal wave speed in the sample, respectively and ρ_f and c_f are the density and the wave speed of sound in the fluid, respectively. The transmission coefficients from the fluid to the longitudinal mode and from the solid to the fluid are given by $T_{fL} = 2\rho_f c_f/(\rho_f c_f + \rho_L c_L)$ and $T_{Lf} = T_{fL}(2\rho_f c_f)/(\rho_L c_L)$, while $R_{ff} = (\rho_L c_L - \rho_f c_f)/(\rho_f c_f + \rho_L c_L)$ defines the reflection coefficient. In addition, $D(\omega_0)$ is the diffraction correction [72] with ω_0 as the center frequency of the input wave. w_0 is the radius of the transducer aperture. w_{z_F} is the Gaussian beam width, and z_F is the water path between the transducer face and a planar reflector from which the reflected amplitude V_{max} is the measured during calibration. Finally, α_f is the attenuation coefficient of the fluid and z_f is the chosen water path between the transducer surface and the sample in the backscatter experiment.

The quantity $\tilde{\eta}^{LL}(\theta_{ps}, k_L)\Xi^{\cdots\hat{\mathbf{p}}\hat{\mathbf{p}}\hat{\mathbf{s}}\hat{\mathbf{s}}}_{\cdots\hat{\mathbf{p}}\hat{\mathbf{p}}\hat{\mathbf{s}}\hat{\mathbf{s}}}(\theta_{ps})$ shown in the second line of the Eq. (4.1) defines the diffuse backscatter coefficient which is used to quantify the microstructural properties. $\tilde{\eta}^{LL}(\theta_{ps}, k_L)$ is the spatial Fourier transform of the correlation function $\eta^{LL}(\mathbf{x} - \mathbf{y})$, which describes the probability that two randomly chosen points, $\mathbf{x}$ and $\mathbf{y}$, lie in a region of the material that has uniform properties. θ_{ps} defines the angle between the incident wave vector $\mathbf{p}$ and the scattered longitudinal wave vector $\mathbf{s}$. For the backscatter experiment examined here, $\theta_{ps} = \pi$ ($k_L = \omega_0/c_L$ is the wave number in the solid). The spatial Fourier transform of the correlation function for the longitudinal-to-longitudinal backscatter mode (with $\theta_{ps} = \pi$) in a test material with a single phase is expressed as [24], [46]

$$\tilde{\eta}^{LL}(\theta_{ps} = \pi, k_L) = \frac{L^3}{\pi^2(1 + 4k_L^2 L^2)^2}. \tag{4.2}$$

In Eq. (4.2), L is defined as the spatial correlation length, which is on the order of the length scale of the grains. The quantity $\Xi^{\cdots\hat{\mathbf{p}}\hat{\mathbf{p}}\hat{\mathbf{s}}\hat{\mathbf{s}}}_{\cdots\hat{\mathbf{p}}\hat{\mathbf{p}}\hat{\mathbf{s}}\hat{\mathbf{s}}}(\theta_{ps}) = \Xi^{\alpha\beta\gamma\delta}_{ijkl}\hat{p}_\alpha \hat{p}_i \hat{s}_\beta \hat{s}_j \hat{p}_\gamma \hat{p}_k \hat{s}_\delta \hat{s}_l$ [7], [24], [46] is the inner product on the eighth-rank covariance tensor $\Xi^{\alpha\beta\gamma\delta}_{ijkl} = \langle C_{ijkl} C_{\alpha\beta\gamma\delta}\rangle - \langle C_{ijkl}\rangle \langle C_{\alpha\beta\gamma\delta}\rangle$, where C_{ijkl} is the second-order modulus tensor (the angular brackets $\langle\rangle$ indicate ensemble average quantities). The vectors $\hat{\mathbf{p}}$ and $\hat{\mathbf{s}}$ indicate the incident and scattering propagation directions, respectively. For a crystal with cubic symmetry [7],

$$\Xi^{\cdots\hat{\mathbf{p}}\hat{\mathbf{p}}\hat{\mathbf{s}}\hat{\mathbf{s}}}_{\cdots\hat{\mathbf{p}}\hat{\mathbf{p}}\hat{\mathbf{s}}\hat{\mathbf{s}}}(\theta_{ps}) = \frac{\nu^2}{\rho^2}\left(\frac{9}{525} + \frac{6}{525}\cos^2\theta_{ps} + \frac{1}{525}\cos^4\theta_{ps}\right), \tag{4.3}$$

where $\nu = c_{11} - c_{12} - 2c_{44}$ is the single crystal anisotropy factor.

The remaining terms given in Eq. (4.1) define the average beam behavior as it penetrates the sample. Thus, α_L is the attenuation coefficient of the solid and σ is the temporal width of the input wave. The Gaussian beam width can be written as [70]

$$w^2(z) = -2k_f^{-1}\left[Im\left(q(0) + z_f + \frac{c_L}{c_f}\right)^{-1}\right]^{-1}, \tag{4.4}$$

where $k_f = \omega_0/c_f$ is the wave number in the liquid, and $q(0) = (-F^{-1} + 2ik_f^{-1}w_0^{-2})^{-1}$, with F as the focal length in water of the transducer used. For the measurements discussed here, the focal properties of the transducer are quantified in advance and used in the model for determining microstructural information.

The backscatter coefficient $\tilde{\eta}^{LL}(\theta_{ps}, k_L)\Xi^{\cdots\hat{\mathbf{p}}\hat{\mathbf{p}}\hat{\mathbf{s}}\hat{\mathbf{s}}}_{\cdots\hat{\mathbf{p}}\hat{\mathbf{p}}\hat{\mathbf{s}}\hat{\mathbf{s}}}(\theta_{ps})$ considered in Eq. (4.1) is applicable only for texture-free materials with single-phase polycrystalline grains. The

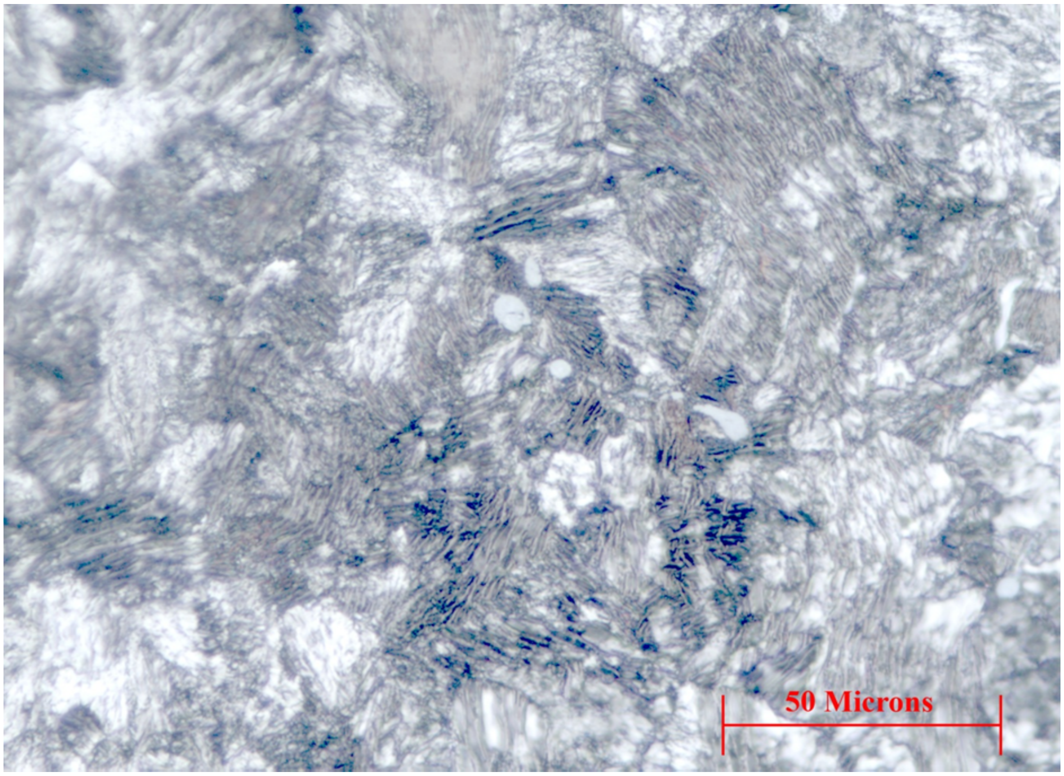

Figure 4.1: Lamellar duplex microstructure (pearlite phase) in the railroad wheel steel.

duplex microstructure within grains exhibited in some structural metals is expected to influence the backscatter coefficient significantly. Figure 4.1 shows the lamellar duplex microstructure in the pearlite-phase of railroad wheel steel. The light lines are the cementite phases, while the dark are the ferrite phases. To describe ultrasonic scattering in two-phase materials (duplex microstructures within grains), Han and Thompson [48] and Rose [47] proposed a general form of the backscatter coefficient. The total backscatter coefficient can be written using the two-point correlation functions for the two phases as

$$\Lambda(\mathbf{x}-\mathbf{y})_{ijkl}^{\alpha\beta\gamma\delta} = (\Xi_{ijkl}^{\alpha\beta\gamma\delta})_r \eta_r(\mathbf{x}-\mathbf{y}) + (\Xi_{ijkl}^{\alpha\beta\gamma\delta})_w \eta_r(\mathbf{x}-\mathbf{y})\eta_w(\mathbf{x}-\mathbf{y}). \tag{4.5}$$

The second term $\eta_r(\mathbf{x}-\mathbf{y})\eta_w(\mathbf{x}-\mathbf{y})$ given in Eq. (4.5) indicates the probability that two randomly chosen points fall in the same grain r and the same crystallite w within the grain. Thus, it is the product of the two independent probabilities η_r and η_w. For the samples of interest here, each lamella is assumed to lie exclusively within one grain. This restriction allows an assumption to be made such that $\eta_r \approx 1$ in the second term of Eq. 4.5 [50]. In other words, the lamellar spacing is small compared with the length scale of the grain such that two points within a lamella have 100 % probability of lying within the same grain.

Lobkis et al. [49], [50] developed a related and simplified backscatter model, which they called the M-factor backscatter model, for duplex microstructure within grains with application to forged near-α Ti alloys. In their model, the duplex spherical crystallites within grains were considered as the second phase and were of major significance to the scattering. Using a similar approach the total backscatter coefficient accounting for the misorientation of duplex microstructure with grains is defined as

$$\Lambda(\mathbf{x}-\mathbf{y})^{\alpha\beta\gamma\delta}_{ijkl} = (1-M)(\Xi^{\alpha\beta\gamma\delta}_{ijkl})_r\eta_r(\mathbf{x}-\mathbf{y}) + M(\Xi^{\alpha\beta\gamma\delta}_{ijkl})_w\eta_w(\mathbf{x}-\mathbf{y}). \tag{4.6}$$

In Eq. (4.6), the parameter M is an average normalized characteristic value that depends on the width of the orientation distribution function. If crystallites within elongated grains are orientated identically, M=0, and elongated grains behave like a single crystal. For the random, arbitrary orientation of crystallites with elongated grains, M=1.0, and the elongated grains are absent. The final expression of the backscatter coefficient K^{LL}_{total} for duplex microstructure, after taking the Fourier transform of the correlation functions and inner products on the eighth-rank covariance tensors, then becomes [49], [50]

$$\begin{aligned} K_{total}^{LL} &= (1-M)[\Xi_{\cdots\hat{\mathbf{p}}\hat{\mathbf{p}}\hat{\mathbf{s}}\hat{\mathbf{s}}}^{\cdots\hat{\mathbf{p}}\hat{\mathbf{p}}\hat{\mathbf{s}}\hat{\mathbf{s}}}(\theta_{ps}=\pi)]_r \tilde{\eta}_r^{LL}(\theta_{ps}=\pi, k_L) \\ &+ M[\Xi_{\cdots\hat{\mathbf{p}}\hat{\mathbf{p}}\hat{\mathbf{s}}\hat{\mathbf{s}}}^{\cdots\hat{\mathbf{p}}\hat{\mathbf{p}}\hat{\mathbf{s}}\hat{\mathbf{s}}}(\theta_{ps}=\pi)]_w \tilde{\eta}_w^{LL}(\theta_{ps}=\pi, k_L). \end{aligned} \tag{4.7}$$

Here, the duplex microstructure (pearlite phase) is assumed to be lamellar within an individual grain such that it can be modeled as shown schematically in Fig. 4.2. In contrast to the duplex crystallites within ellipsoidal microtextural regions (MTRs) considered previously [49], here the grain shape is assumed spherical. The duplex crystallites within grains are represented by a lamellar microstructure characterized by alternating cementite and ferrite phases. The parameter d represents the lamellar spacing, while L is the correlation length which is on the order of the length scale of an individual grain. The geometry of a duplex crystallite can be considered as a lamellar circular plate, with a diameter dimension equal to the correlation length, while the thickness is equal to the lamellar spacing.

In Fig. 4.2, k_x and k_y represent the wave numbers in the lamellar plane and normal to the plane, respectively, and are given by

$$\begin{aligned} k_x &= \sin(\theta) k_L, \\ k_y &= \cos(\theta) k_L, \\ k_z &= 0, \\ k_L &= \sqrt{k_x^2 + k_y^2 + k_z^2}. \end{aligned} \tag{4.8}$$

For this microstructure, the correlation function for the ellipsoidal grains [49], [50] $\tilde{\eta}(k) = \frac{a_x a_y a_z}{\pi^2(1+4k_x^2a_x^2+4k_y^2a_y^2+4k_z^2a_z^2)}$, must be adapted for the lamellar crystallites. In this case, the spatial scales a_x, a_z and a_y must be redefined as $a_x = a_z = L$ and $a_y = d$.

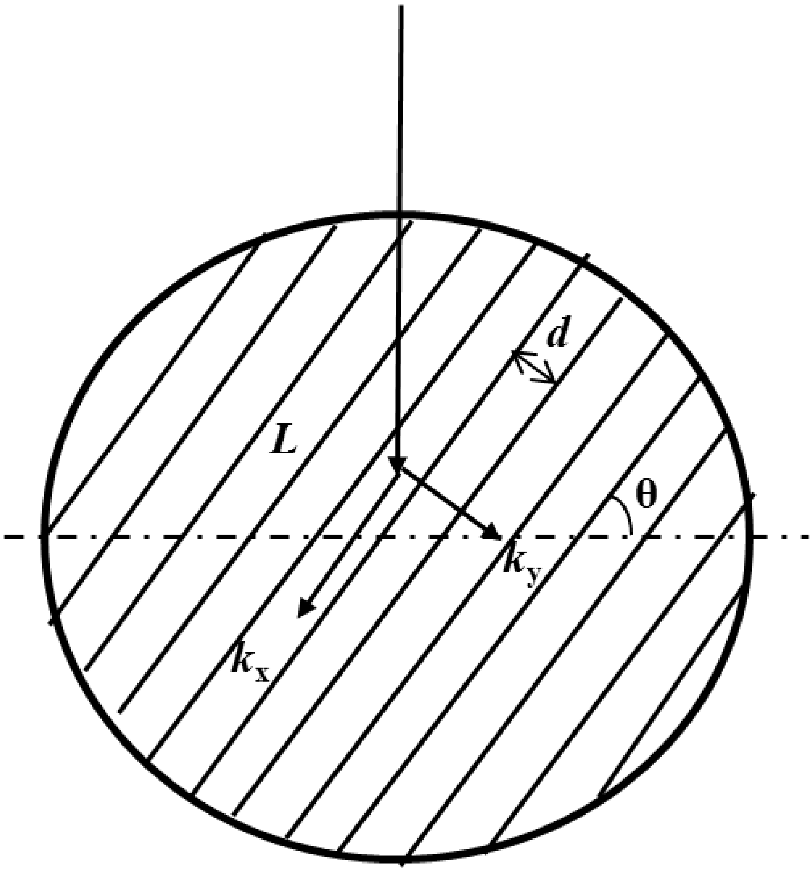

Figure 4.2: Schematic of lamellar duplex microstructure within an individual grain (pearlite phase).

Following the approach in [49], the spatial correlation function $\tilde{\eta}_w^{LL}(\theta_{ps} = \pi, k_L)$ for microstructure shown in Fig. 4.2 is written as

$$\begin{aligned}\tilde{\eta}_w^{LL}(\theta_{ps} = \pi, k_L) &= \frac{a_x a_y a_z}{\pi^2(1 + 4k_x^2 a_x^2 + 4k_y^2 a_y^2 + 4k_z^2 a_z^2)^2}, \\ &= \frac{L^2 d}{\pi^2(1 + 4k_L^2 \langle l^2 \rangle)^2}, \end{aligned} \tag{4.9}$$

where $k_L = \sqrt{k_x^2 + k_y^2 + k_z^2}$ and the quantity $l = \sqrt{n_x^2 a_x^2 + n_y^2 a_y^2 + n_y^2 a_y^2}$ defines the interaction length, which is the effective scale length in the direction of wave propagation, $\hat{\mathbf{n}}$. Here, the duplex crystallites within grains are assumed to be oriented randomly such that the angle θ shown in Fig. 4.2 varies with equal probability between 0 and π. The square of the effective interaction length is then averaged [49] giving

$$\langle l^2 \rangle = \frac{1}{\pi}\int_0^{\pi} (\sin^2\theta L^2 + \cos^2\theta d^2)d\theta = (L^2 + d^2)/2. \tag{4.10}$$

Substituting the Eq. (4.10) into Eq. (4.9) the correlation function for lamellar duplex microstructure is given by

$$\tilde{\eta}_w^{LL}(\theta_{ps} = \pi) = \frac{L^2 d}{\pi^2(1 + 2k_L^2 l^2)^2} = \frac{L^2 d}{\pi^2 \left[1 + 2k_L^2(L^2 + d^2)\right]^2}. \tag{4.11}$$

After substituting Eqs. (4.2) and (4.11) into the Eq. (4.7), the total backscatter coefficient becomes

$$K_{total}^{LL} = \frac{(1-M)L^3[\Xi^{\cdots\hat{\mathbf{p}}\hat{\mathbf{p}}\hat{\mathbf{s}}\hat{\mathbf{s}}}_{\cdots\hat{\mathbf{p}}\hat{\mathbf{p}}\hat{\mathbf{s}}\hat{\mathbf{s}}}(\theta_{ps} = \pi)]_r}{\pi^2(1 + 4k_L^2 L^2)^2} + \frac{ML^2 d[\Xi^{\cdots\hat{\mathbf{p}}\hat{\mathbf{p}}\hat{\mathbf{s}}\hat{\mathbf{s}}}_{\cdots\hat{\mathbf{p}}\hat{\mathbf{p}}\hat{\mathbf{s}}\hat{\mathbf{s}}}(\theta_{ps} = \pi)]_w}{\pi^2\left[1 + 2k_L^2(L^2 + d^2)\right]^2}. \tag{4.12}$$

Then by replacing the backscatter coefficient given in Eq. (4.1) with Eq. (4.12), the modified SSR, which includes the dependence of ultrasonic scattering on lamellar duplex microstructure, can be expressed as

$$\begin{aligned}
\Phi^{LL}(t) &= V_{max}^2 \frac{\pi}{8\sqrt{2}} \left(\frac{w(z_F)}{w_0}\right)^2 \left(\frac{\rho_L c_L^2}{\rho_f c_f^2}\frac{T_{fL}T_{Lf}}{R_{ff}D(\omega_0)}\right)^2 \exp(4\alpha_f z_F - 4\alpha_f z_f) \\
&\times \left[\frac{\pi}{2}\frac{\omega_0^4}{c_L^8}\frac{(1-M)L^3[\Xi^{\cdots\hat{\mathbf{p}}\hat{\mathbf{p}}\hat{\mathbf{s}}\hat{\mathbf{s}}}_{\cdots\hat{\mathbf{p}}\hat{\mathbf{p}}\hat{\mathbf{s}}\hat{\mathbf{s}}}(\theta_{ps} = \pi)]_r}{\pi^2(1 + 4k_L^2 L^2)^2} + \frac{ML^2 d[\Xi^{\cdots\hat{\mathbf{p}}\hat{\mathbf{p}}\hat{\mathbf{s}}\hat{\mathbf{s}}}_{\cdots\hat{\mathbf{p}}\hat{\mathbf{p}}\hat{\mathbf{s}}\hat{\mathbf{s}}}(\theta_{ps} = \pi)]_w}{\pi^2\left[1 + 2k_L^2(L^2 + d^2)\right]^2}\right] \\
&\times \exp\left(-\frac{t^2}{\sigma^2}\right)\int_0^{\infty} \frac{w_0^2}{w^2(z)} \exp\left[-4\alpha_L z - \frac{4z(z - tc_L)}{\sigma^2 c_L^2}\right] dz.
\end{aligned} \tag{4.13}$$

When the lamellar spacing d approaches L, (i.e, the lamellar duplex microstructure is absent), Eq. 4.13 reduces to the theoretical SSR model for a single phase given previously [24], [46]. Note that the inner product on the eighth-rank covariance tensor for lamellar duplex microstructure within a grain $[\Xi^{\cdots\hat{\mathbf{p}}\hat{\mathbf{p}}\hat{\mathbf{s}}\hat{\mathbf{s}}}_{\cdots\hat{\mathbf{p}}\hat{\mathbf{p}}\hat{\mathbf{s}}\hat{\mathbf{s}}}(\theta_{ps} = \pi)]_w$ is assumed equal to the same quantity when the lamellae are absent, $[\Xi^{\cdots\hat{\mathbf{p}}\hat{\mathbf{p}}\hat{\mathbf{s}}\hat{\mathbf{s}}}_{\cdots\hat{\mathbf{p}}\hat{\mathbf{p}}\hat{\mathbf{s}}\hat{\mathbf{s}}}(\theta_{ps} = \pi)]_r$. Several trends in the behavior of this model are observed in the next section.

4.2 Model Results

In this section, trends predicted by the model with respect to the microstructural parameters are examined. Several parameters given in Eq. (4.13) required for the model must first be specified (including the pulse width σ, the single-crystal elastic constants of steel, the sound speeds in water and steel). Table 4.1 shows some of the values used in the model for the results that follow. Theoretical values were selected for wavespeed and values for attenuation as a function of frequency come from [21] for water and from [7] for steel assuming a single phase material with a single correlation length. In addition, for the results shown in this section, transducer parameters were selected in the range of typical experiments (transducer element diameter of 0.375 inch; focal length in water of 2 inches; material path of 9.0 mm; central transducer frequency of 10 MHz for Fig. 4.3 and varying frequency for Fig. 4.4).

Fig. 4.3 shows the predicted spatial backscatter variance curves normalized by the maximum of the variance for the case without the lamellar microstructure. The solid

Table 4.1: Constants used in the theoretical model to examine the influence of lamellar spacing. The wave speeds and attenuation values are determined from scattering models from the grains without the lamellar structure as derived in [7].

Pulse Width	$V_{max}(V)$.		c_{ij}(GPa)		
σ	10MHz	15MHz	c_{11}	c_{12}	c_{13}
1.0	550	250	229.3	134.1	116.7

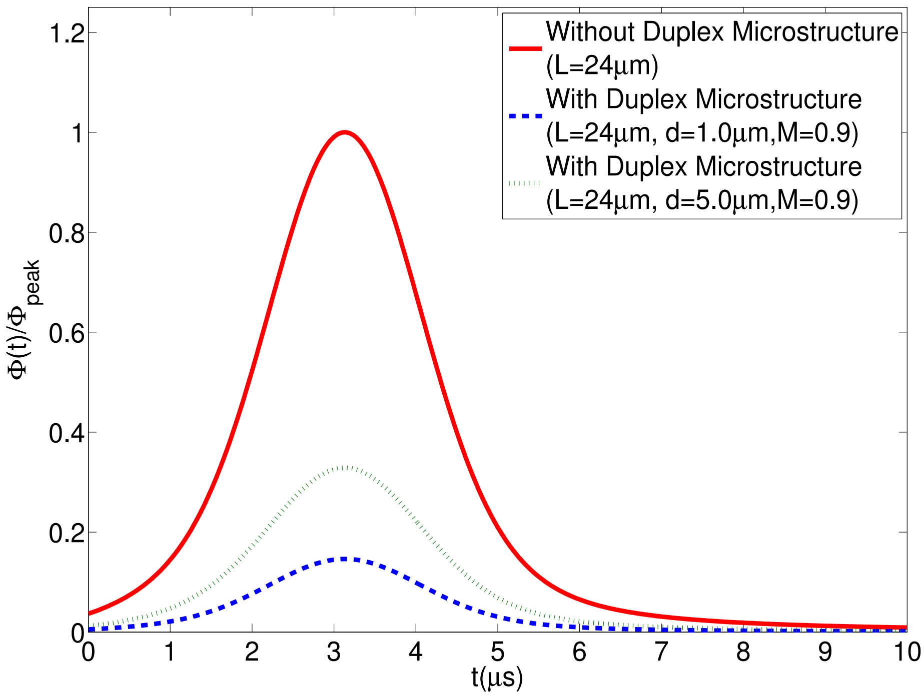

Figure 4.3: Spatial variance curves from the model given by Eq. (4.13) with and without the inclusion of duplex microstructure within grains ($M = 0.9$) with a transducer center frequency of 10 MHz.

red line shows the variance curve for the sample with no lamellar duplex microstructure within grains. The dashed blue and dotted green lines represent the calculated variance curves which include the effects of lamellar duplex microstructure, with d $= 1.0$ and 5.0 μm, respectively (the range is based on optical micrographs such as that shown in Fig. 4.1). It can be observed that the ultrasonic scattering amplitude decreases greatly when the pearlite phase is present within grains and is lowest for the smallest value of d. However, it is important to note that the lamellar spacing does not change the shape of the variance curves.

The backscatter coefficient given in Eq. (4.13) contains three unknown variables related to the microstructure M, d and L. First the dependence of backscatter ampli-

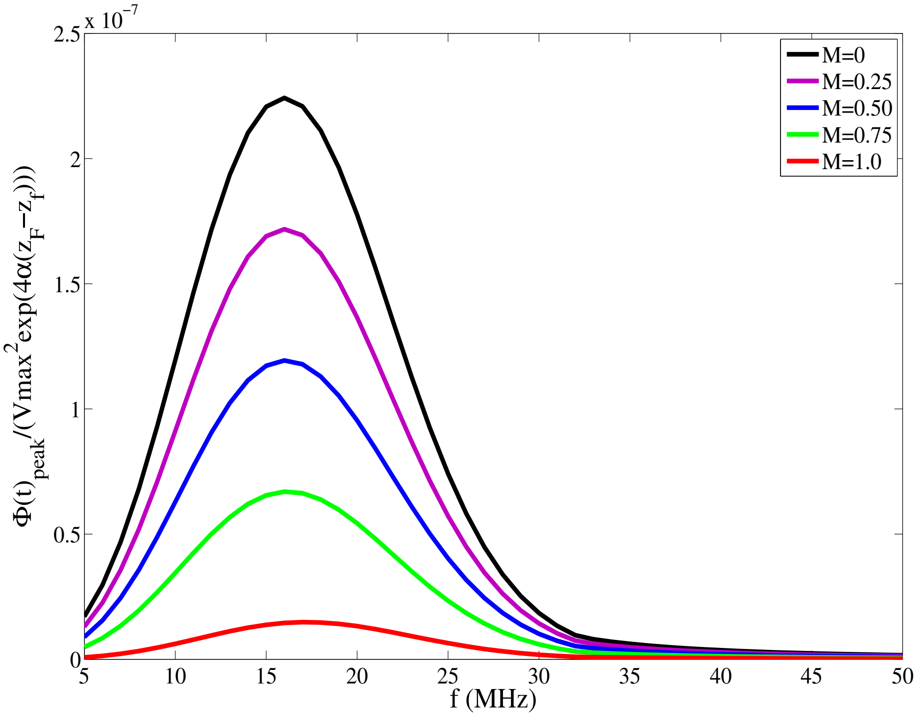

(a)

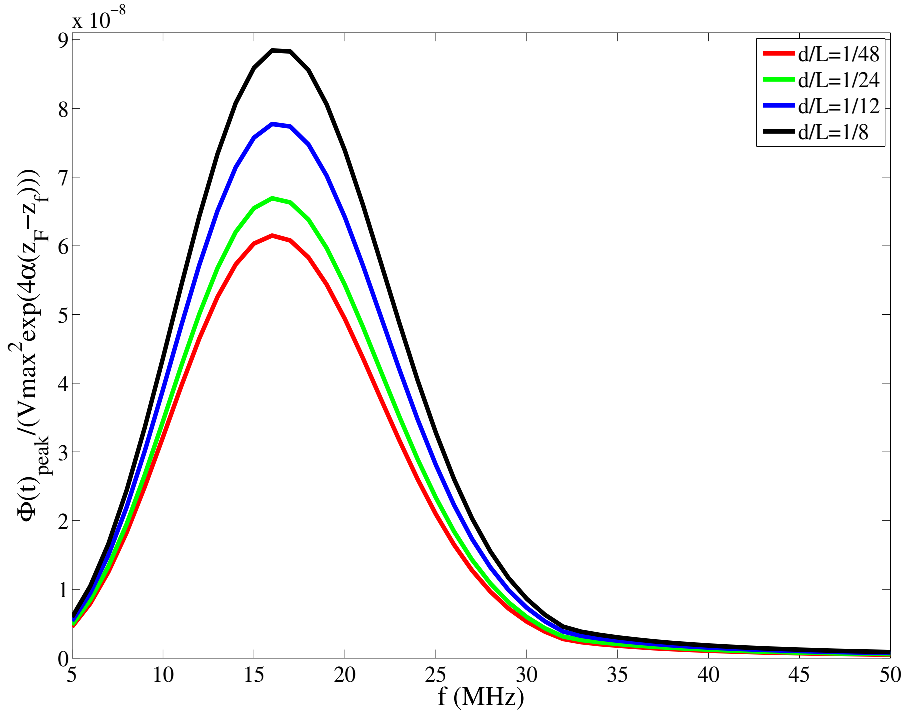

(b)

Figure 4.4: Normalized spatial variance amplitudes versus frequency, (a) by fixing d/L=1/24, L=24 μm, (b) by fixing M =0.75 and L=24 μm.

tude on the parameter M is investigated by fixing d=1 μm, L=24 μm. Fig. 4.4a shows the maximum of the spatial variance amplitudes normalized by $V_{max}^2 \exp[4\alpha_f(z_F - z_f)]$ versus frequency with varying M (all transducer parameters are the same as in Fig. 4.3 except for the central frequency of the transducer). The parameter M=0 indicates that duplex microstructures within grains are absent, while M=1.0 represents that the scattering from the grain boundaries is neglected. It can be seen that the amplitudes of the variance curves decrease with increasing M. The maximum spatial variance amplitude occurs around 15 MHz, which implies the frequency range for materials with these types of microstructures would lie in the range of 10 to 20 MHz for greatest sensitivity to the length scales of the material. The backscatter amplitude is relatively low either due to weak scattering below 10 MHz or high attenuation above 20 MHz. Fig. 4.4b demonstrates the dependence of spatial variance on lamellar spacing d with fixed M=0.75 and L = 24 μm. The normalized SSR amplitude increases with increasing lamellar spacing. This spacing has only a minor effect on the associated maximum backscatter amplitude with respect to frequency. The trends shown here suggest that frequencies between 10 and 15 MHz may be useful for determining M, d, and L based on the range of values expected for railroad wheel steel.

4.3 Experiments

4.3.1 Backscatter Measurements

The tread surface of railroad wheels is typically quenched to improve the hardness and wear resistance. In order to examine the microstructure difference between an unquenched wheel (20 mm thickness) and a quenched wheel (25 mm thickness), eight rectangular regions (15 mm × 5 mm) were scanned (approximate scan areas are shown

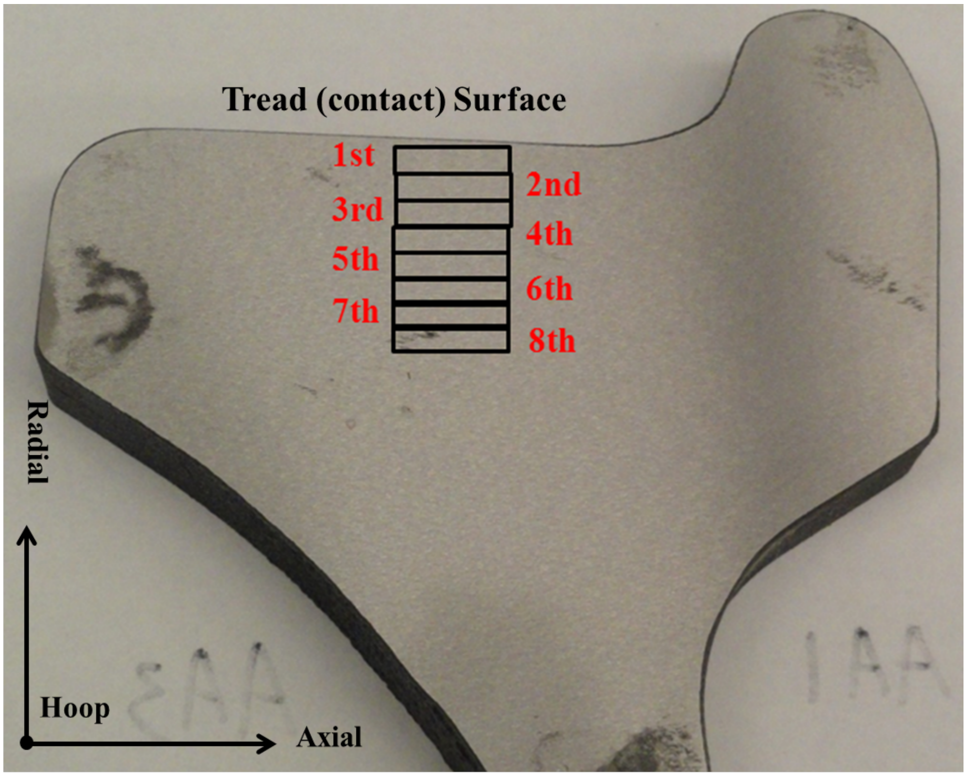

(a)

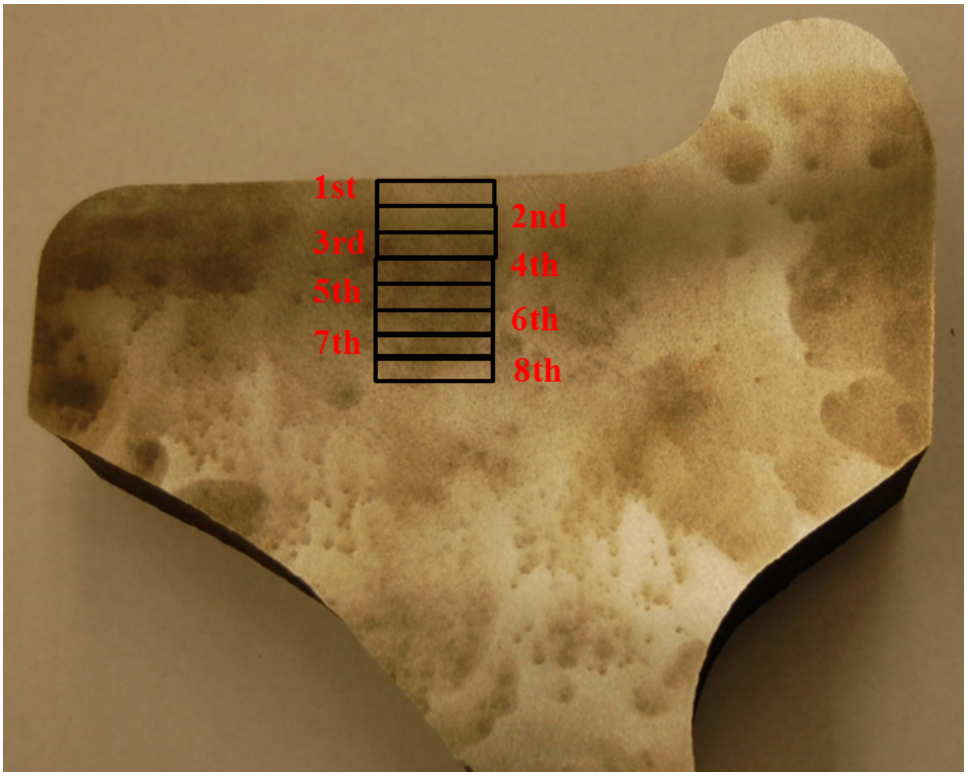

(b)

Figure 4.5: Cross section images of polished railroad wheel samples, (a) an unquenched wheel, (b) a quenched wheel.

in Figs. 4.5. These regions represent locations expected to have varying pearlite due to quenching. Both samples were scanned using a 15 MHz focused transducer (Panametrics V309, 3-inch focal length) and a 10 MHz focused transducer (Panametrics V327, 2-inch focal length, *Olympus Panametrics, Inc.*, Waltham, MA) with a focal depth in the material of 10 mm (scan step size = 0.25 mm; scan speed = 3.0 mm/s). Note that the focusing properties of the transducer were measured in advance and were included in the model. To obtain strong backscatter signals, a high gain (65 dB) was used (A/D sampling rate = 2 GHz). The number of scan locations for each area was about 1200. Fig. 4.6 shows a typical waveform from an individual measurement. The range of time of interest for the spatial variance calculation lies between the saturated front wall reflection and the back wall reflection. The experimental spatial variance of the acquired backscatter signals collected from various positions for each area is calculated by

$$\Phi(t) = \frac{1}{N}\sum_{i=1}^{N}(V_i(t) - b(t))^2 = \langle V^2 \rangle - \langle V \rangle^2, \tag{4.14}$$

where N is the number of spatial positions, $b(t) = \langle V \rangle$ is the ensemble average of the backscatter signals, $\langle V^2 \rangle$ is the ensemble average of the squared backscatter signals, $\langle V \rangle^2$ is the square of the mean backscatter signals.

Figs. 4.7a and 4.7b show the calculated spatial variance (10 MHz) from the tread surface to the deeper positions for both unquenched and quenched wheels, respectively. The first ~ 2 μs of each curve is saturated due to the large front wall reflection resulting from the high amplifier gain. At later times, the influence of the heterogeneous composition of the sample can be observed. In particular, in Fig. 4.7a for the unquenched wheel, the spatial variance is relatively constant over the 8 scan regions, a result that shows the uniformity of the material over the range examined.

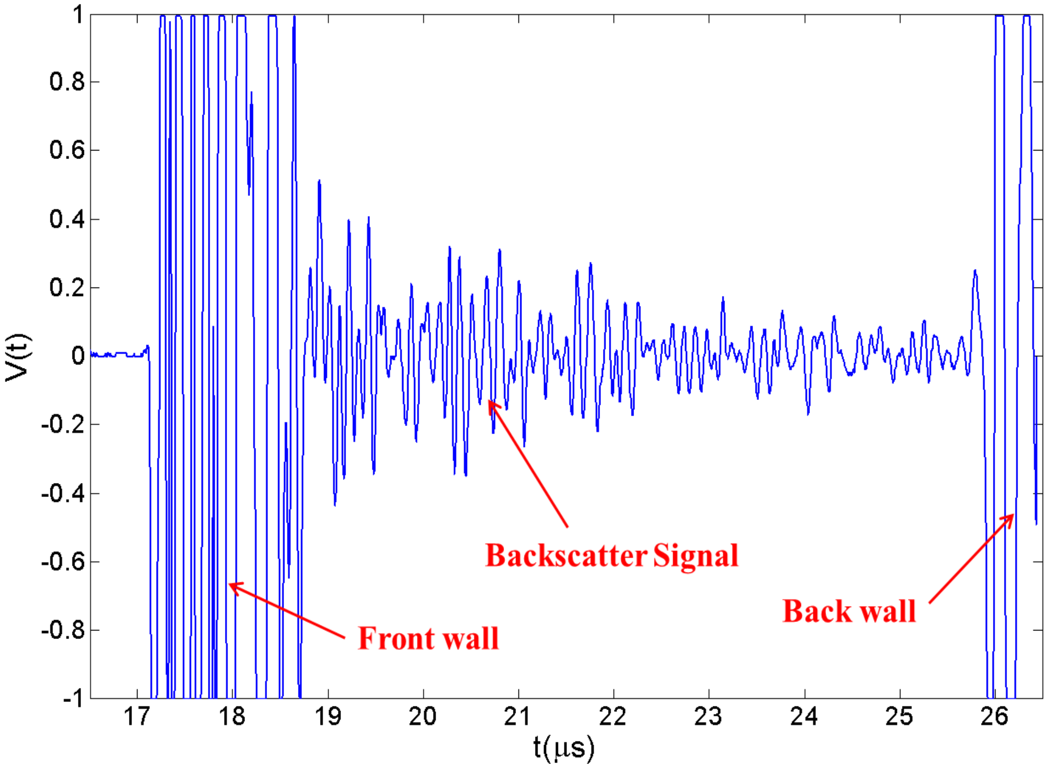

Figure 4.6: Example of a typical waveform included in the spatial variance calculations of Eq. (4.14). The part of the signal of primary interest lies between the front and back wall echoes and is due to scattering from the grains.

However, on the quenched wheel (Fig. 4.7b), the spatial variance amplitude drops dramatically near the quenched tread surface. A similar effect is observed for the 15 MHz measurements.

Fig. 4.8 illustrates the distribution of peak values of the spatial variance with depth from the tread surface for both the unquenched and quenched wheels from the 10 and 15 MHz measurements. The solid green and red lines represent the measured results for the unquenched wheel at 10 and 15 MHz transducers, respectively. while the dashed lines of the same colors indicate the results for the quenched wheel. For the unquenched wheel, It can be seen that the spatial variance amplitudes are relatively constant from the tread surface to deeper locations, which implies that

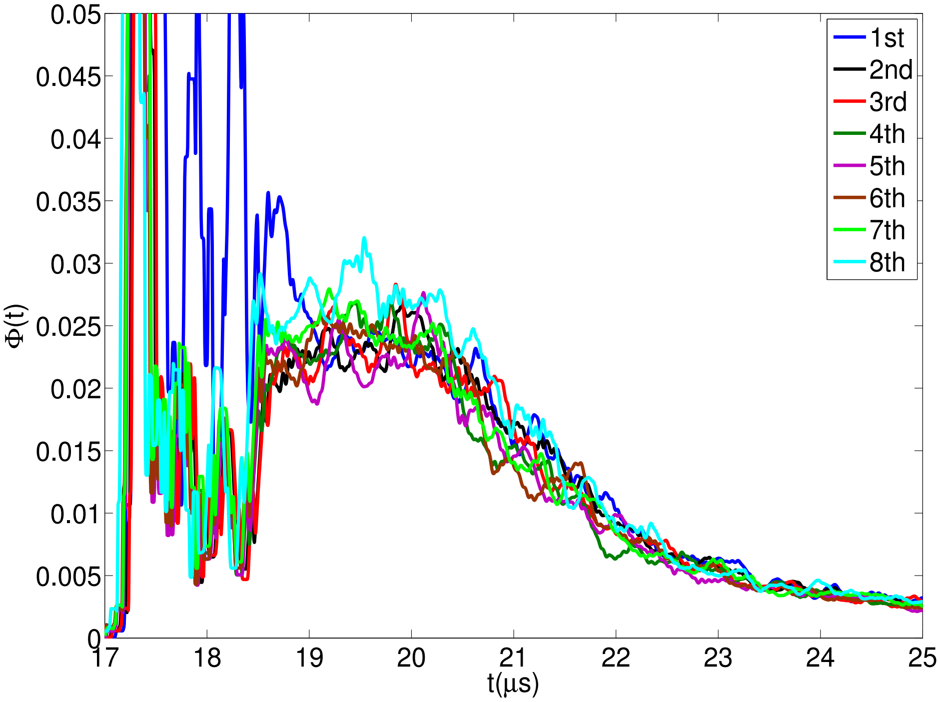

(a)

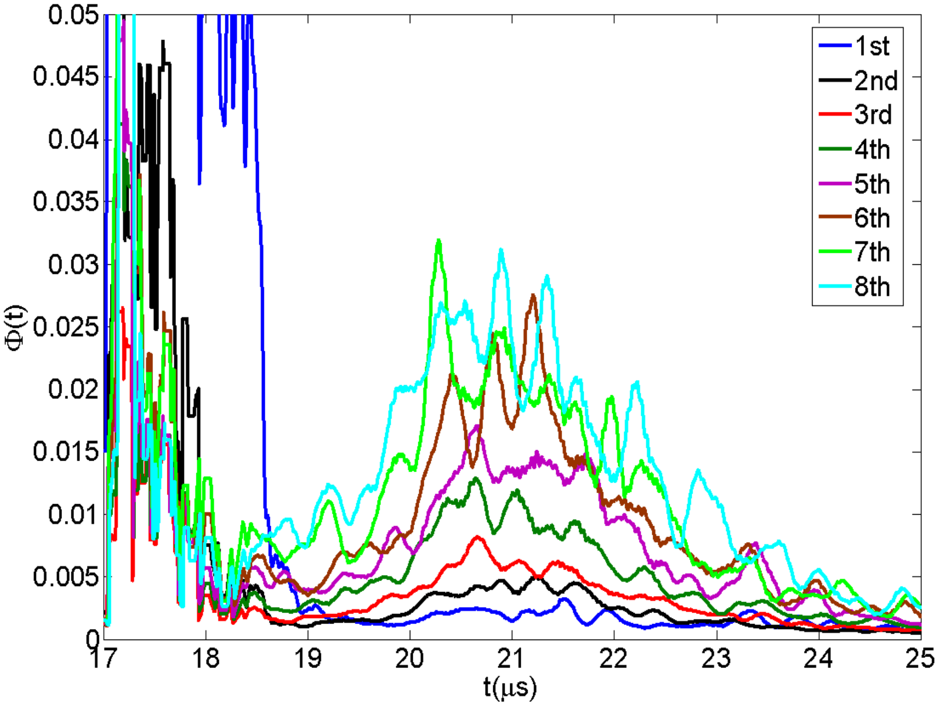

(b)

Figure 4.7: Spatial variance curves with a 10 MHz focused transducer, (a) for an unquenched wheel, (b) for a quenched wheel.

the grains and microstructure are relatively uniform along the entire cross section of this sample. After quenching, the spatial variance peak increases progressively with depth from the tread surface, a result that is attributed to the variation of the pearlite microstructure within grains as a result of the quenching. The amplitude difference between the unquenched wheel and quenched wheel is relatively small at deeper positions. This result indicates that the effect of the pearlite on ultrasonic scattering at deeper locations is negligible. Clearly, the ultrasonic scattering response is not only related to the lamellar duplex microstructure, but also highly dependent on the transducer frequency. However, it should be noted that the values shown in Fig. 4.8 are raw variance results and should not be used to make conclusions regarding the relative amount of scattering occurring at these two frequencies. The transducer properties and scattering model must be used for an accurate interpretation of the experiments. The theoretical SSR model given in Eq. (4.13) is now used to fit the experimental variance curves in order for the microstructural parameters of the model to be determined.

The spatial variance amplitudes shown in Fig. 4.8 can be used to quantify the microstructural parameters of correlation length (L) and lamellar space (d) using the model derived above. The constants shown in Table 4.1 are used and the wave velocity and attenuation were measured for both water (c_f = 1486 m/s; α_f(10 MHz) = .025 Np/cm; α_f(15 MHz) = .056 Np/cm) and the steel samples (c_L = 5973 m/s; α_L(10 MHz) = .055 Np/cm; α_L(15 MHz) = .06 Np/cm). The transducer was first calibrated to determine some important parameters such as V_{max} before testing [24], [46]. It was assumed that the grain size in both wheel samples was uniform and that only the pearlite phase was created during the quenching. The mean correlation length is found to be $L = 24$ μm as determined from measurements on the unquenched wheel with the existing SSR model given in Eq. (4.1). Then, the maximum of the experimental

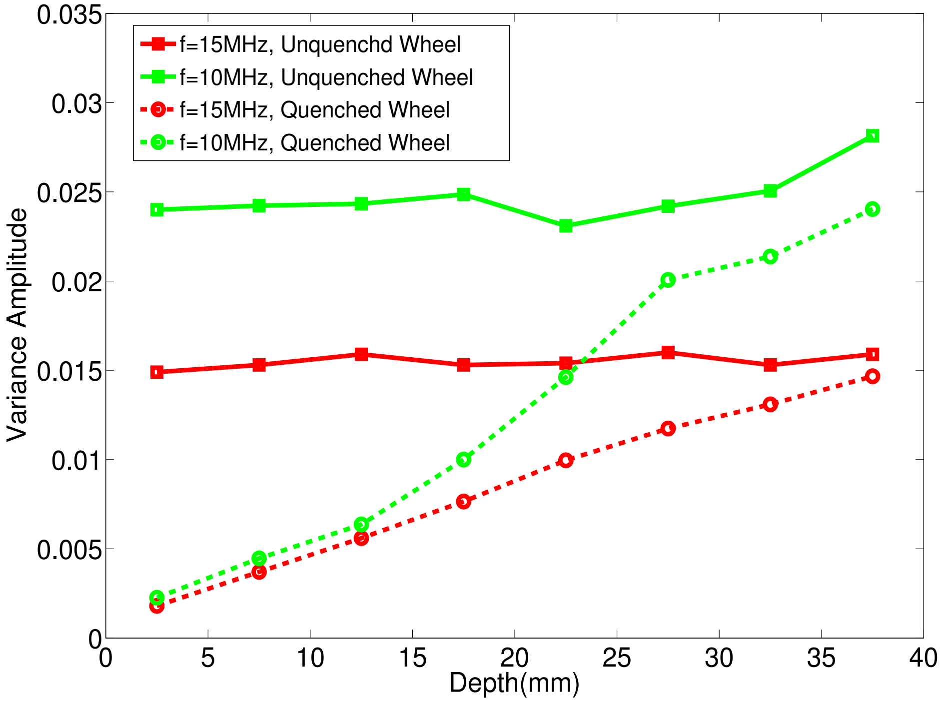

Figure 4.8: Distribution of spatial variance amplitudes from tread surface to the deeper location with 10 MHz and 15 MHz focused transducers.

spatial variance, $[\Phi^{LL}_{Exp}(t)]_{max}$, is used with Eq. (4.13) and Eq. (4.1) to estimate the lamellar spacing d. The quantity d appears in Eq. (4.13) in only one term, such that the experimental variance can be equated to the model and rearranged into an equation governing d. Following this procedure, it can be shown that d satisfies the quartic equation

$$A_1 d^4 + A_2 d^2 - A_3 d + A_4 = 0, \tag{4.15}$$

where

$$
\begin{aligned}
A_1 &= 4k_L^4\left[16R\pi^2k_L^4L^4 + 8R\pi^2k_L^2L^2 - (1-M)L^3 + R\pi^2\right];\\
A_2 &= \left[16R\pi^2k_L^4L^4 + 8R\pi^2k_L^2L^2 - (1-M)L^3 + R\pi^2\right](8k_L^4L^2 + 4k_L^2);\\
A_3 &= ML^2(1+4k_L^2L^2)^2;\\
A_4 &= \left[16R\pi^2k_L^4L^4 + 8R\pi^2k_L^2L^2 - (1-M)L^3 + R\pi^2\right](1 + 4k_L^4L^4 + 4k_L^2L^2), \quad (4.16)
\end{aligned}
$$

with $R = \frac{[\Phi_{Exp}^{LL}(t)]_{max}}{[\Phi^{LL}(t)]_{max}/\tilde{\eta}_{total}^{LL}}$, where $\tilde{\eta}_{total}^{LL} = \left[(1-M)\tilde{\eta}_r^{LL}(\theta_{ps}=\pi, k_L) + M\tilde{\eta}_w^{LL}(\theta_{ps}=\pi, k_L)\right]$. By fixing M and L, Eq. (4.15) will have constant variables A_1-A_4 and four solutions. Experience with the solution of Eq. (4.15) when applied to experimental data shows that only one root is physically meaningful. Thus, this root is chosen as the estimated lamellar spacing.

Fig. 4.9 shows the distribution of the estimated lamellar spacing, d, with depth from the tread surface for different values of M. The solid lines indicate the estimated results using a 15 MHz transducer, while the dashed lines are for a 10 MHz transducer. It can be observed that the estimated value of d increases from 0.5 μm to around 5.5 μm from the tread surface to deeper locations. The lamellar spacing decreases with decrease of the parameter M. Differences in the estimated value of d from the 10 and 15 MHz measurements become larger with depth. The reason for this result is not clear, but the higher frequency is expected to be more sensitive to the lamellar spacing such that the 15 MHz results may be more representative. In addition, the quench depth for these samples is in the range of 12 mm, a value that matches the transition depth observed for 15 MHz.

Optical analysis has also been done to observe the variation of lamellar duplex microstructure within grains. Two samples from the quenched wheel were polished and mounted for optical microscopy. One was taken near the tread surface and the

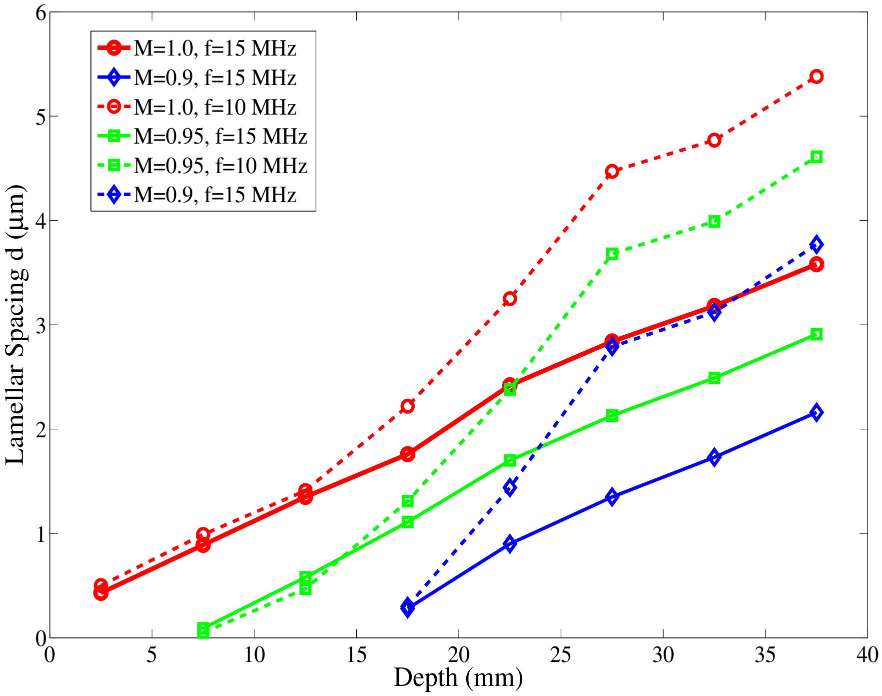

Figure 4.9: Distribution of calculated lamellar space d from tread surface to the deeper location.

other was removed from a depth of 30 mm from the tread surface. The sample surface was etched with 2.0 % nital solution for 30 seconds, followed by rinsing with ethanol and running water. Fig. 4.10a shows the micrograph of the fine pearlite phase near the tread surface and Fig. 4.10b shows a micrograph of the coarse pearlite phase. It can be observed that the fine pearlite phase has compact lamellar spacing due to the fastest cooling rate, while at the 30 mm-depth location, the pearlite phase exhibits much more coarse lamellar spacing due to the slower cooling rate. The average coarse lamellar spacing is measured around 3.5-4.5 μm which is much larger than that near the tread surface. The measured lamellar spacing agrees well with the values found from the ultrasonic backscatter approach.

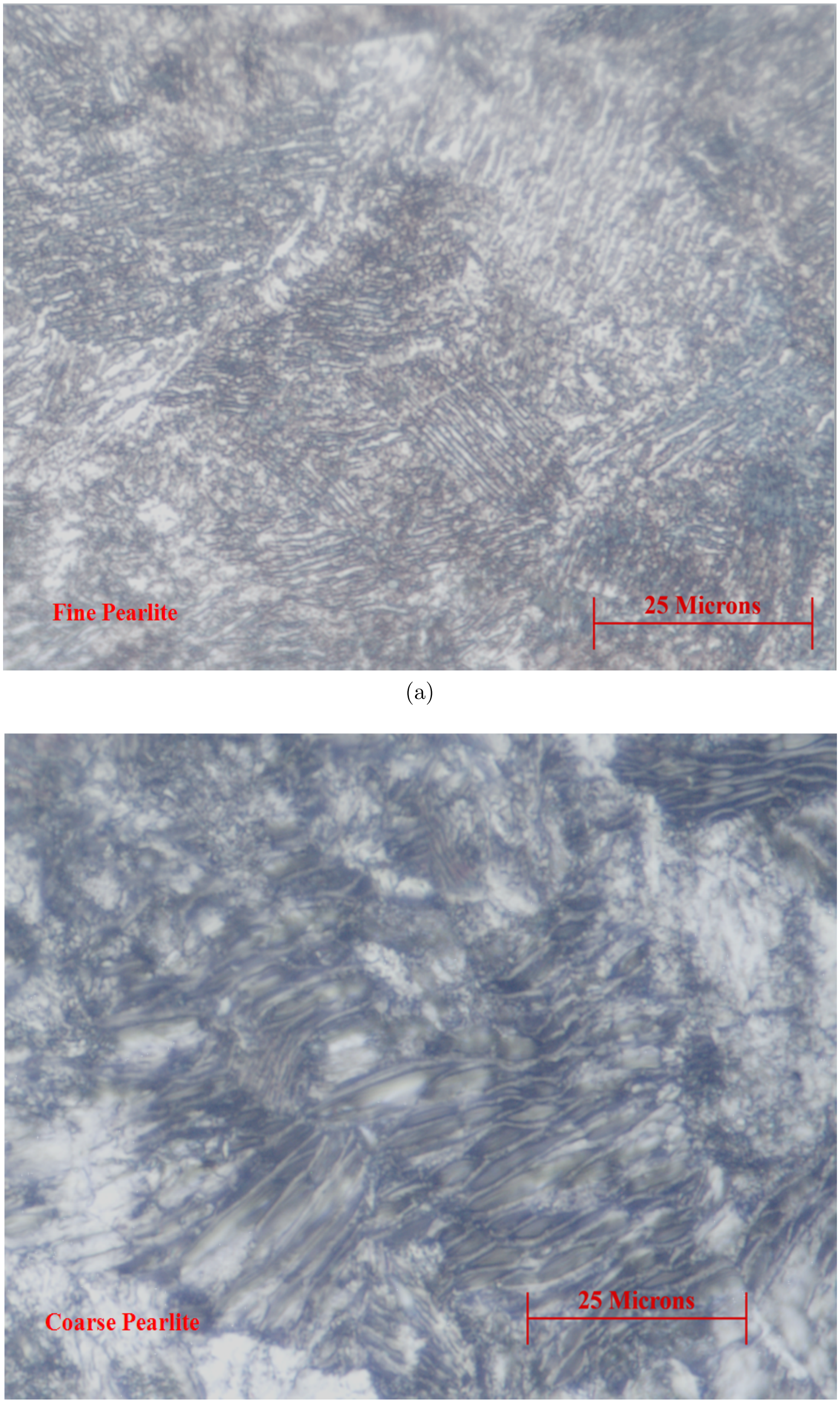

(a)

(b)

Figure 4.10: Micrographs of pearlite phase in a railroad wheel steel, (a) near the tread surface, (b) at a depth of 30 mm from the tread.

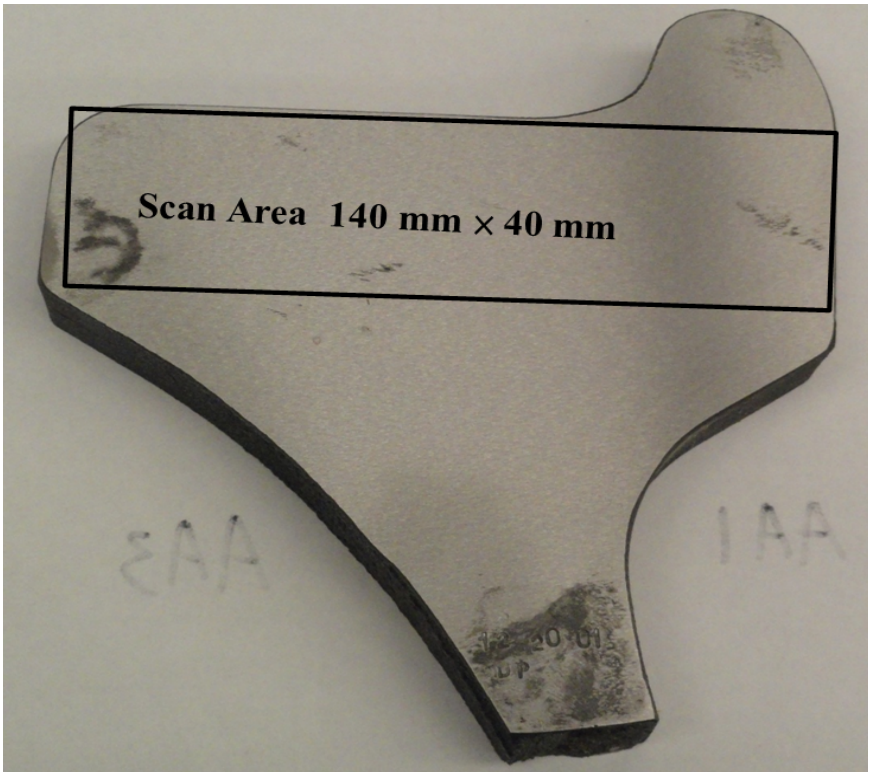

Figure 4.11: A cross section image of a quenched wheel sample.

4.3.2 Cross Section Mapping

To examine the variation of microstructure, both cross sections of the unquenched and quenched wheel samples were scanned using a 10 MHz focused transducer (Panametrics V327, 2-inch focal length, *Olympus Panametrics, Inc.*, Waltham, MA) focused at a depth of 10 mm. Fig. 4.11 shows the scan region on the polished cross section of a quenched wheel sample (scan step size = 0.25 mm; scan speed = 3.0 mm/s). The spatial variance curves were obtained from the waveforms by observing the energy between the front surface reflection and back surface reflection. A gate approximating the width of pulse was set to cover the focal depth to extract the maximum amplitudes of the reflective signals at each locations. The amplitudes are displayed with different colors.

Fig. 4.12a shows a C-scan image of an unquenched wheel sample. The color bar indicates the percentage of maximum amplitude of scattering with respect to the saturated front wall reflection. It can be observed that the higher scattering amplitude indicators are distributed uniformly and randomly in the whole cross section of the unquenched wheel sample. Fig. 4.12b demonstrates a C-scan image of the quenched wheel sample. A progressive increase of amplitudes from the quenched surfaces to central locations can be observed, an outcome which is attributed to the creation of the pearlite phase. The high amplitude indicators in the central location might result from the appearance of the larger grains formed via the heat treatment.

To quantify the distribution of grain size and/or microstructure from the surface to deeper locations, a 5 mm × 5 mm box shown in Fig. 4.11 including approximately

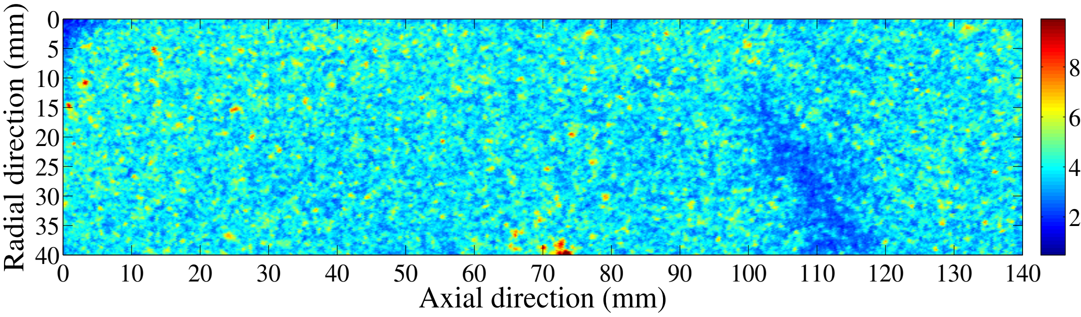

(a)

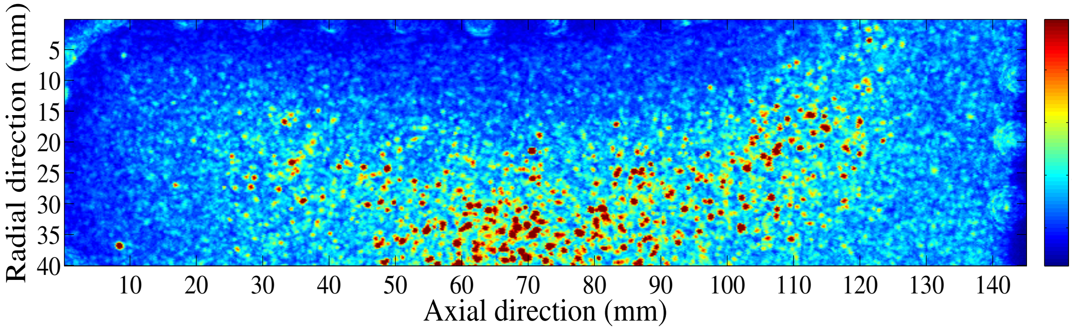

(b)

Figure 4.12: C-scan images of cross section of wheel slice samples, (a) before quenching, (b) after quenching.

600 positions was used for calculating the spatial variance curve. The spatial variance curves were fit using the theoretical model given in Eq. (4.13) to extract the variance amplitudes. The spatial variance amplitudes for the unquenched and quenched wheels are distributed in Figs. 4.13a and 4.13b, respectively, for which the color scale ranges from 0.002 to 0.032. By comparing these two variance images, it can be seen that the backscatter amplitude drops dramatically in the region near the quenched surface, an indication of the fine pearlite microstructure. The fine lamellar structure within the grains scatters the input energy less than the untransformed grains, an outcome that results in the lower backscatter amplitudes. The ultrasonic backscatter technique has sufficient sensitivity to distinguish the microstructural differences, an aspect that

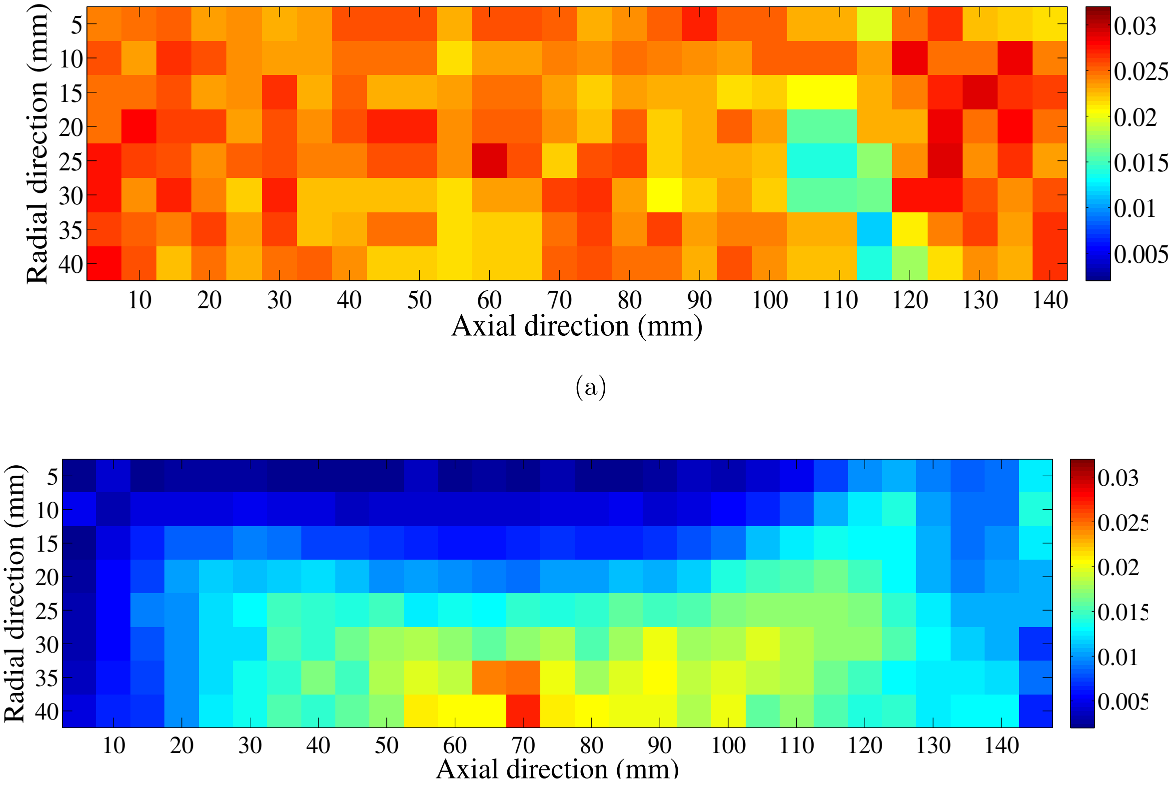

(a)

(b)

Figure 4.13: Variance amplitude distribution for cross section mapping of wheel samples, (a) before quenching, (b) after quenching.

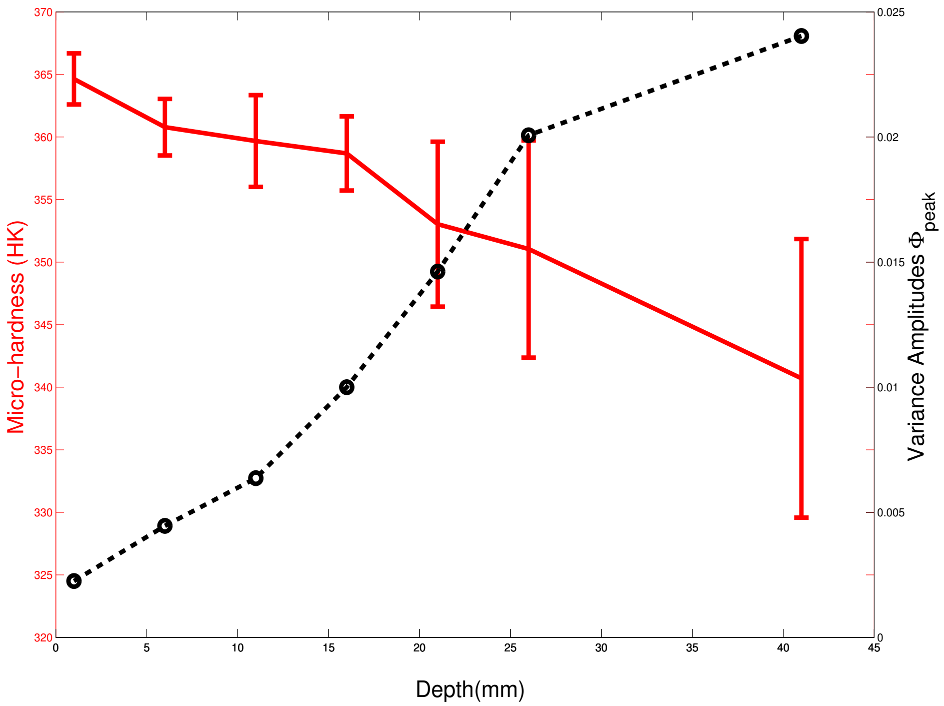

Figure 4.14: Comparison between the measured hardness and spatial variance amplitude from the tread surface to deeper positions.

could lead to improved quality control methods.

4.3.3 Ultrasonic Backscatter and Hardness

The lamellar duplex microstructure shown in Fig. 4.1 results in an improvement of the mechanical properties, such as the tensile strength and hardness. The connection between the ultrasonic backscatter and the hardness is investigated in the quenched wheel sample through experiments. The Knoop hardness test, a microhardness test for the brittle materials, is used to measure the hardness on the polished cross section of the quenched wheel steel sample. An elongated diamond pyramidal indenter was used to press into the polished surface of the test wheel material with a known 500 g load for a specified dwell time, and the resulting indentation was measured using a microscope. The geometry of this indenter is an extended pyramid with the length to width ratio being 7:1 and respective face angles are 172 degrees for the long edge and 130 degrees for the short edge. The depth of the indentation can be approximated as 1/30 of the long dimension. Multiple locations at the same depth from the tread surface were chosen to test the hardness. The length of the Knoop elongated pyramid indentation was measured. The distance between two random indentations is about two times bigger than the diagonal length of the previous indentation. The Knoop hardness HK measured at different depths is calculated by

$$HK = \frac{P}{C_P H}, \tag{4.17}$$

where P is the applied load, H is the length of indentation along the long axis, C_p is a correction factor related to the shape of the indenter (ideally 0.070279). Fig. 4.14 shows the measured hardness and the spatial variance peaks with depth from the tread surface to deeper locations. The error bar represents the standard deviation of the hardness measured at different locations at the same distance from the tread surface. It can be seen that the hardness near the tread surface is much larger and relative constant within about 15 mm depth which is attributed to the fine pearlite. The hardness value decreases progressively from 15 mm depth to deeper locations due to the coarse pearlite. By comparing the measured hardness with the variance amplitudes, a strong connection between the measured hardness and spatial variance peaks can be observed. Several additional observations can be also made. First, the fine lamellar duplex microstructure that scatters less energy can improve the hardness near the region of the quenched tread surface. Second, the higher spatial variance amplitude corresponds to the smaller hardness at deeper locations due to the coarse pearlite. Lastly, the ultrasonic backscatter measurement is more sensitive to the microstructural change. The connection between the hardness and the ultrasonic scatteing is so strong that diffuse ultrasonic backscatter can be applied not only for distinguishing the variation of microstructure, but also may be used to estimate the hardness of steel.

4.4 Summary

In this chapter, a new singly-scattered response (SSR) model that includes pearlite microstructure within grains has been developed based on the previous SSR model. Diffuse ultrasonic backscatter experiments were conducted in a water tank using 10 and 15 MHz transducers focused 10 mm deep in both unquenched and quenched railroad wheel sections. The spatial variance amplitude drops dramatically near the tread surface which is attributed to the fine lamellar spacing of the pearlite created by quenching. At deeper locations, the ultrasonic scattering variance amplitude changes little after quenching. The diffuse ultrasonic backscatter response from the fine pearlite at 15 MHz is much higher than that at 10 MHz, while the scattered response to the coarse pearlite at 15 MHz is much weaker than that from 10 MHz. The distribution of lamellar spacing with depth from the tread surface was also quantified with the newly developed SSR model. The calculated lamellar spacing within grains ranged from 0.5-5.5 μm. Optical analysis was also made to observe the microstructure and the results agree well with the ultrasonic approach.

The whole cross section (140 mm × 40 mm) of the wheel sample was scanned with a 10 MHz focused transducer focused at a depth of 10 mm. The spatial variance amplitudes on the whole cross section of both the unquenched and quenched wheel samples were mapped by calculating the spatial variance curve of each (5 mm × 5 mm) subarea and extracting the amplitudes after fitting with the Eq. (4.13). A progressive increase of the variance amplitudes was observed from the quenched surfaces (including the tread surface and the rim surface) to central locations due to the increasing lamellar spacing. It is also known that the lamellar duplex microstructure influences the mechanical properties of steel. A strong connection between ultrasonic backscatter and the hardness was obtained. The smaller variance peaks correspond to higher hardness. Diffuse ultrasonic backscatter provides a non-destructive method to evaluate the pearlite microstructure within grains, which can be implemented for quality control in conjunction with other manufacturing processes.

Chapter 5

Measurement of Quench Depth in Quenched Railroad Wheels

The increase of lamellar spacing with depth from the tread surface was observed in chapter 4. The developed SSR model that includes the effects of the lamellar spacing given by Eq. (4.13) is not applicable for the measurement from the tread surface due to the increase of lamellar spacing on the propagation path. In this chapter, the developed SSR model is expanded to include the gradation of lamellar duplex microstructure on the propagation path for application to railroad wheels. The effects of the graded duplex microstructure on ultrasonic scattering are investigated by comparing the spatial variance curve measured from the tread surface with that measured from the cross section. Measurement of the quench depth (well known as the thickness of the hardened layer) can be realized by fitting the spatial variance curve using the new modified SSR model. Because the quench depth plays an important role in the service performance of railroad wheels, nondestructive measurements of this depth are needed.

5.1 Theory

In chapter 4 the final expression of the SSR model for railroad wheel steel with uniform lamellar duplex microstructure within grains (pearlite phase) was given by Eq. (4.13). It shows that the lamellar spacing d exhibits a large spatial dependence with depth from the quenched surface to deeper locations due to the non-uniform cooling rate. When an ultrasonic wave is normally incidence on the tread surface of the sample, the lamellar spacing increases on the ultrasound propagation path. The depth-dependent lamellar space d results in the dependence of correlation function $\tilde{\eta}_w^{LL}$ on depth z as shown in Fig. 5.1a. The average spatial correlation function $\tilde{\eta}_w^{LL}(\theta_{ps} = \pi, k_L, z)$ shown in Eq. (4.11) is modified to include the dependence of lamellar duplex microstructure with depth on the acoustic propagation path

$$\tilde{\eta}_w^{LL}(\theta_{ps} = \pi, k_L, z) = \frac{L^2 d(z)}{\pi^2[1 + 2k_L^2(L^2 + d^2(z))]^2}. \tag{5.1}$$

By substituting Eq. (5.1) into Eq. (4.13), the SSR model that considers the gradation of lamellar spacing on the propagation path is given by

$$\begin{aligned}\Phi^{LL}(t) = {} & V_{max}^2 \frac{\pi}{8\sqrt{2}} \left(\frac{w(z_F)}{w_0}\right)^2 \left(\frac{\rho_L c_L^2}{\rho_f c_f^2} \frac{T_{fL} T_{Lf}}{R_{ff} D(\omega_0)}\right)^2 \exp\left(4\alpha_f z_F - 4\alpha_f z_f \frac{t^2}{\sigma^2}\right) \\ & \times \int_0^\infty \frac{w_0^2}{w^2(z)} \left[\frac{\pi}{2} \frac{\omega_0^4}{c_L^8} \frac{(1-M) L^3 [\Xi_{\cdots\hat{\mathbf{p}}\hat{\mathbf{p}}\hat{\mathbf{s}}\hat{\mathbf{s}}}^{\cdots\hat{\mathbf{p}}\hat{\mathbf{p}}\hat{\mathbf{s}}\hat{\mathbf{s}}}(\theta_{ps} = \pi)]_r}{\pi^2(1 + 4k_L^2 L^2)^2} + \frac{M L^2 d(z) [\Xi_{\cdots\hat{\mathbf{p}}\hat{\mathbf{p}}\hat{\mathbf{s}}\hat{\mathbf{s}}}^{\cdots\hat{\mathbf{p}}\hat{\mathbf{p}}\hat{\mathbf{s}}\hat{\mathbf{s}}}(\theta_{ps} = \pi)]_w}{\pi^2[1 + 2k_L^2(L^2 + d^2(z))]^2}\right] \\ & \times \exp\left[-4\alpha_L z - \frac{4z(z - tc_L)}{\sigma^2 c_L^2}\right] dz. \end{aligned} \tag{5.2}$$

Other parameters in Eq. (5.2) have been detailed in chapter 4. When the lamellar spacing d is depth-independent and approaches L, which means that the lamellar duplex microstructure is absent, Eq. (5.2) reduces to Eq. (4.1). Note that the inner product on the eighth-rank covariance tensor for lamellar duplex microstructure within grain $[\Xi^{\cdots\hat{\mathbf{p}}\hat{\mathbf{p}}\hat{\mathbf{s}}\hat{\mathbf{s}}}_{\cdots\hat{\mathbf{p}}\hat{\mathbf{p}}\hat{\mathbf{s}}\hat{\mathbf{s}}}(\theta_{ps} = \pi)]_w$ is assumed to be approximately equal to $[\Xi^{\cdots\hat{\mathbf{p}}\hat{\mathbf{p}}\hat{\mathbf{s}}\hat{\mathbf{s}}}_{\cdots\hat{\mathbf{p}}\hat{\mathbf{p}}\hat{\mathbf{s}}\hat{\mathbf{s}}}(\theta_{ps} = \pi)]_r$. Several trends in the behavior of this model can be observed.

5.2 Model Results

In this section, trends predicted by the model with respect to the microstructural parameters are examined. Several parameters given in Eq. (5.2) required for the model must first be specified (including the pulse width in time σ and the single-crystal elastic constants of steel). Table 4.1 shows some of the values used in the results that follow. Theoretical values were selected for wavespeed and values for attenuation come from [21] or water and from [7] for steel assuming a single phase material with a single correlation length.

Fig. 5.1a shows a schematic of the ultrasonic test of a railroad wheel steel sample with the graded lamellar spacing within grains. The wheel steel sample can be simplified by assuming it has a two-layered organization. The top layer is a fine duplex-microstructure layer characterized by the small lamellar spacing d. The depth of the top layer z_1 is defined as the quench depth. The bottom layer exhibits the coarse duplex microstructure. The transducer is focused within the top layer shown in Fig. 5.1a. The material path M_p, also known as the geometrical focus, is defined as the focal depth in the test material shown in Fig. 5.1a. W_p indicates the water path, a distance between the transducer surface and the sample surface. Here, the quantity W_p is equal to the parameter z_f in the Eq. (5.2). The relation between M_p and W_p is determined by $M_p = c_f(F - W_p)/c_L$, where F is the focal length of the transducer in water. Fig. 5.1b shows three different cases for the dependence of lamellar spacing d on depth z from the tread surface to deeper locations. For the example calculations, the quench depth z_1 is set to 12.5 mm and z_2 is equal to 40 mm. The lamellar

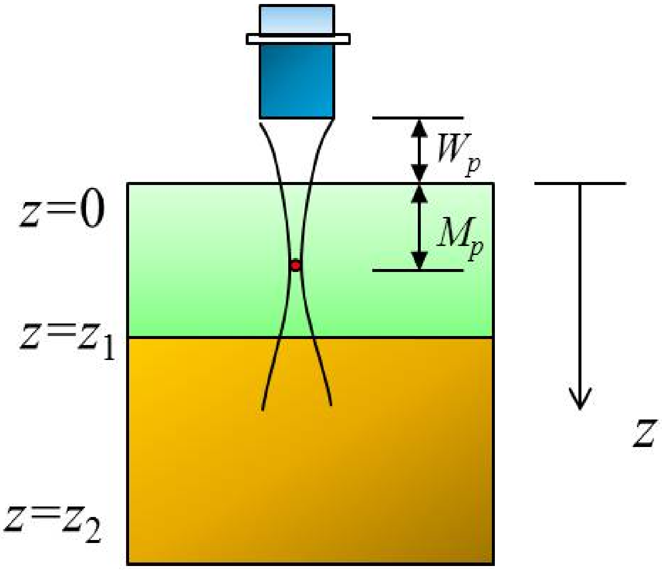

(a)

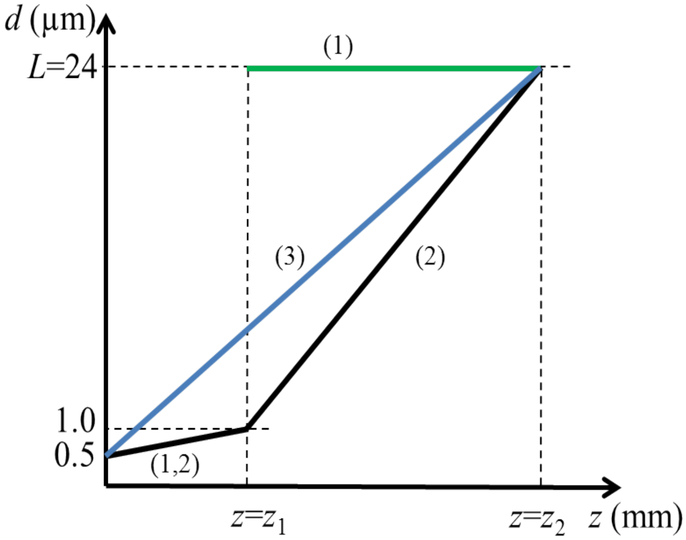

(b)

Figure 5.1: (a) Schematic of the ultrasonic testing of a railroad wheel sample using the normal incident ultrasound, (b) The dependence of lamellar spacing d on depth z.

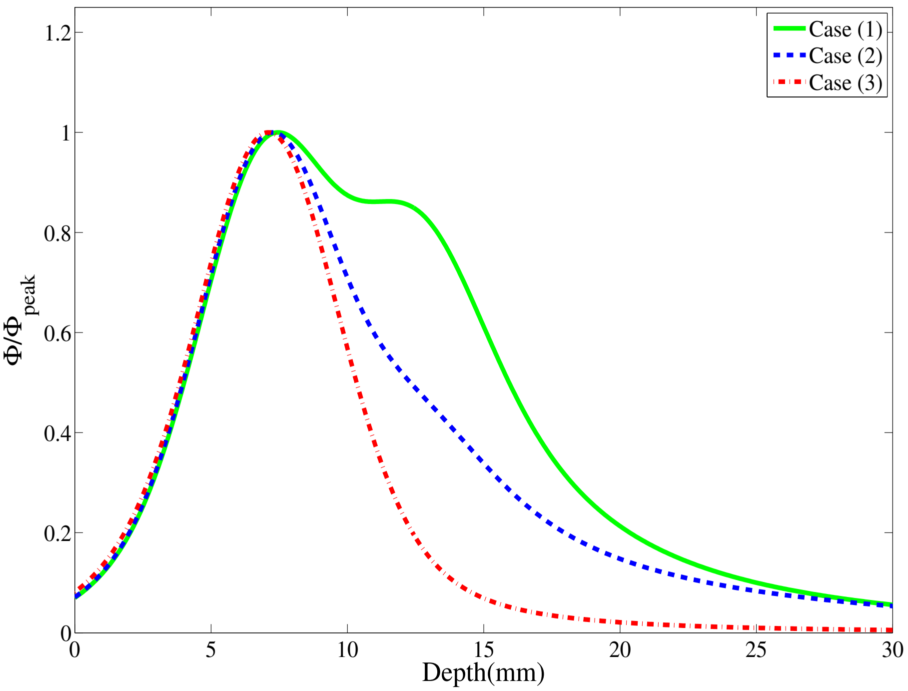

Figure 5.2: Normalized spatial variance curves with respect to different profiles shown in Fig. 5.1b of lamellar spacing distribution.

spacing d increases very slowly from 0.5 μm to 1.0 μm within the quench depth for cases (1) and (2), while the lamellar spacing d grows quickly with a linear function in the bottom layer for case (2). The duplex microstructure is absent when the lamellar spacing d equals L. For case (1), the lamellar duplex microstructure is absent ($d = L$) below the quench depth. In case (3), the lamellar spacing d increases linearly from 0.5 μm to 24 μm.

Fig. 5.2 shows the calculated scattering responses normalized by peak values with respect to these three cases, respectively. It can be seen that the width of the variance curve is largest with respect to case (1), in which the lamellar space d is assumed equal to the correlation length L (no duplex microstructure) in the bottom layer. The scattered response is also examined for different material paths M_p to investigate the

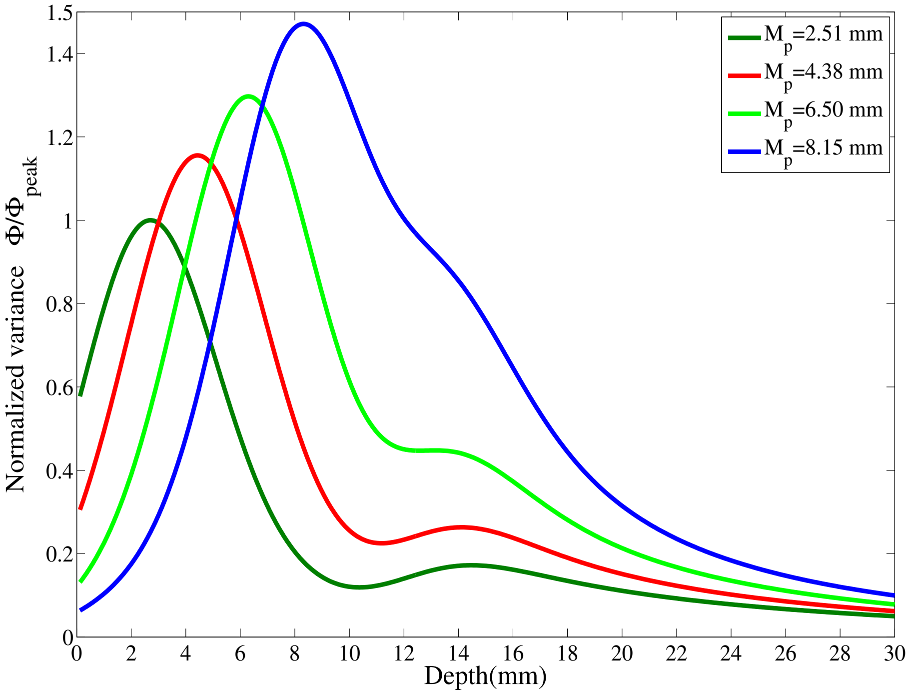

Figure 5.3: Normalized variance curves corresponding to different water paths (calculated using M=0.9 in Eq. (5.2)).

dependence of the variance amplitudes on varying lamellar spacing with respect to case (2).

Fig. 5.3 demonstrates the spatial variance curves normalized by the variance peak with respect to material path M_p=2.51 mm. The dependence of lamellar spacing d on depth z shown in the Fig. 5.1b is utilized in the model. Here the parameter M is chosen to be 0.9 as described in chapter 4. It can be seen that the spatial variance amplitude increases as the material path M_p increases, a result that is attributed to the stronger ultrasonic scattering due to the larger lamellar spacing at deeper locations. In addition, the width of the variance curve increases because of the influence of the coarser microstructure. The spatial variance peak also shifts to later times as the transducer focuses more deeply. In the next section, results from experiments are presented from both the tread surface and the cross section of a wheel sample. Then the SSR model for the graded microstructure is used to estimate the quench depth from the experiments.

5.3 Experiments

Experiments were conducted in a water immersion tank using a 10 MHz focused transducer (*Olympus NDT*, Newton, MA, V327-SU; 9.53 mm diameter; 50.4 mm focal length) focused 9.5 mm in a quenched railroad wheel steel sample. Figs. 5.4a and 5.4b show images of polished cross section and tread surface of a quenched railroad wheel sample, respectively. The experiments were performed by time-gating the acquired scattered signals so that the signal between the front and back surface reflections can be used. The scan step size was 0.25 mm and 1.0 mm for the tread surface and the cross section scan, respectively. The scan speed was set to 3.0 mm/s. Note that the focusing properties of the transducer were measured in advance and are included in the model. To obtain strong backscatter signals, a high gain (65 dB) was used (A/D sampling rate = 2 GHz). The number of scan locations was about 2400 and 1500 for the scan areas on the tread surface and cross section, respectively. The scan area on the cross section shown in Fig. 5.4a was similar to the focal depth of measurements from the tread surface illustrated in Fig. 5.4b. The spatial backscatter variance curves were calculated for each scan area according to Eq. (4.14).

Fig. 5.5 shows the spatial variance curves along with the curve fits using Eqs. (4.13) and (5.2), respectively. The travel time in steel is converted to values for material depth by simply multiplying by the measured wave velocity in steel (note that two travel depths are traversed in the backscatter experiments). The depth of the variance peak is not exactly equal to the pre-defined material path, a minor difference that

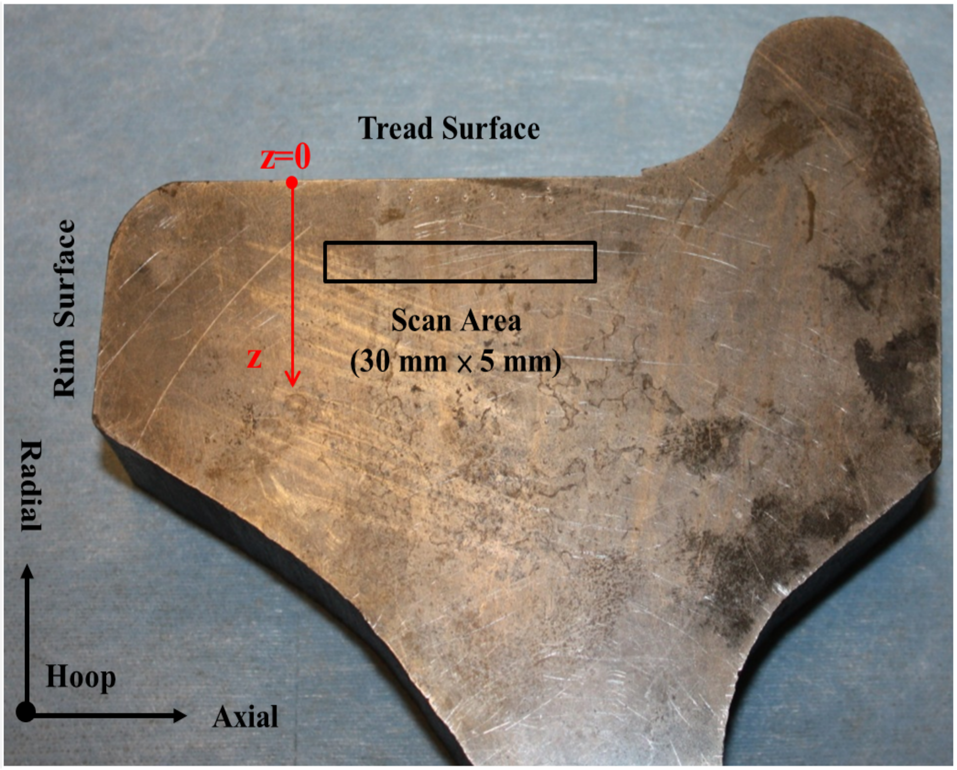

(a)

(b)

Figure 5.4: Images of a quenched railroad wheel sample produced by *Griffin Wheel, Inc.*, (a) cross section, (b) tread surface.

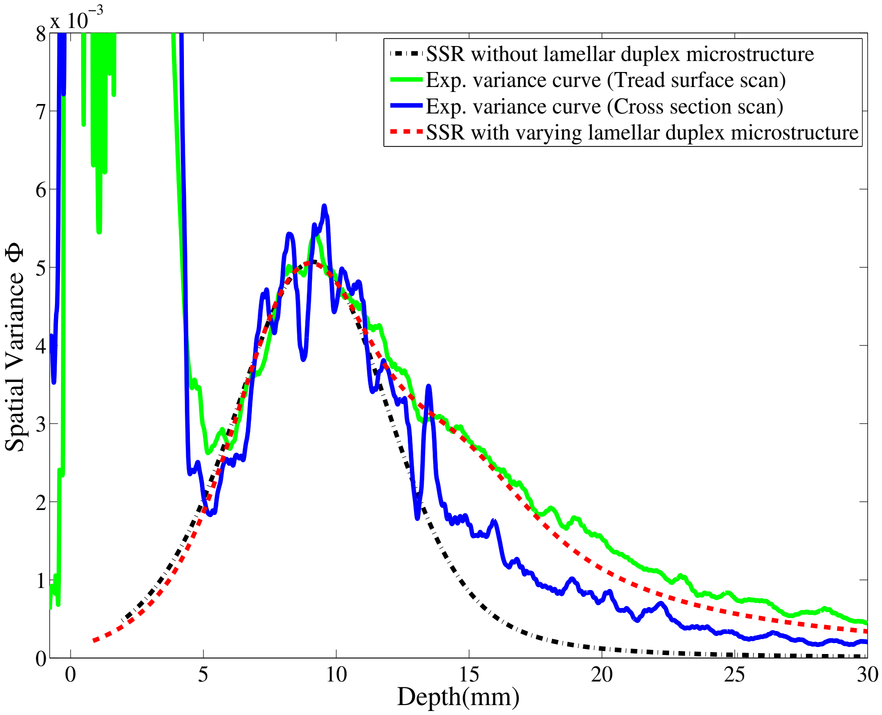

Figure 5.5: The spatial variance curves for tread surface and cross section scanning along with the fitting curves.

is attributed to the uncertainty of the wave speed and attenuation in the material. The solid blue and green lines represent the spatial variance curves of backscattered signals for the cross section and tread surface scans, respectively. It was observed in chapter 4 that the duplex microstructure increases progressively from the tread surface to deeper locations in the radial direction due to the decreasing cooling rate, while in the hoop direction, the duplex microstructure was essentially constant. By comparing the two spatial variance curves, the effects of the graded microstructure on ultrasonic scattering can be observed. Although the spatial variance maxima are very similar due to the nearly identical focal volumes, the difference between the two curves grows larger and larger for times after the peak. The width of the variance curve measured from the tread surface is larger than that measured from the cross

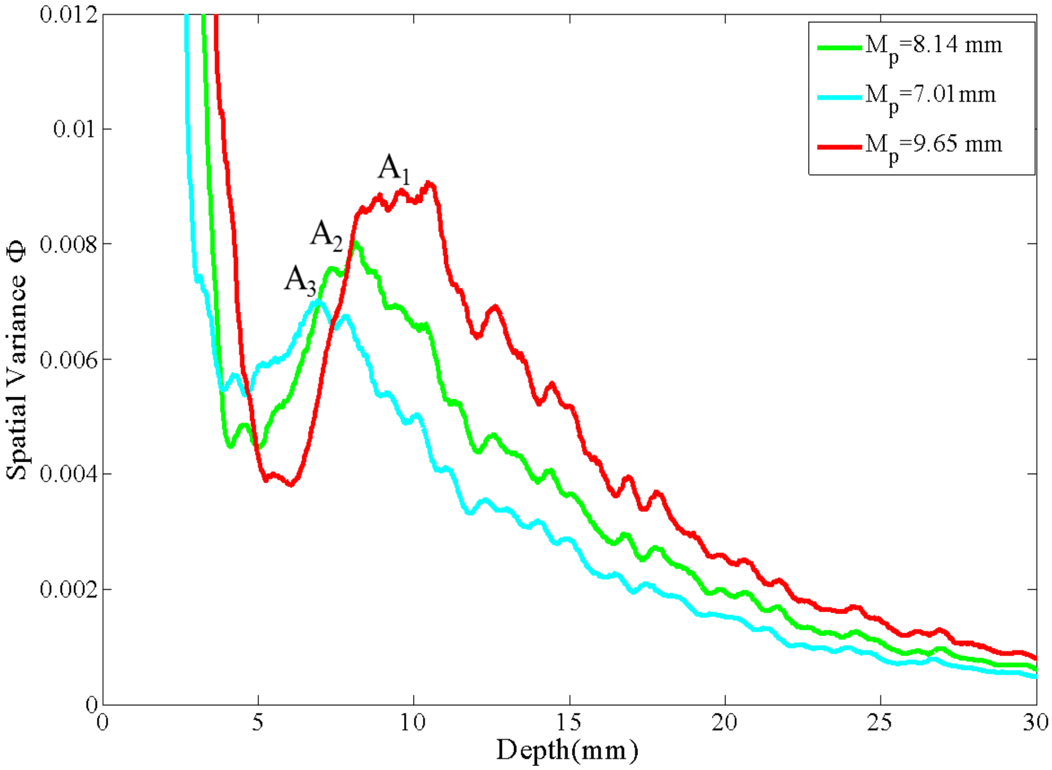

Figure 5.6: The spatial variance curves with respect to varying material paths. $A_i, (i = 1, 2, 3)$ represents the variance peak.

section, a result that is attributed to the stronger scattering from the larger lamellar spacing at deeper locations. The dashed black and red lines demonstrate the curve fits based on Eqs. (4.13) and (5.2), respectively. For these results, the wave velocity and attenuation were measured for both water (c_f = 1486 m/s; α_f = 0.025 Np/cm) and the steel sample (c_L = 5973 m/s; α_L = 0.045 Np/cm). The dependence of lamellar spacing d on z shown in Fig. 5.1b is utilized for the fits. The curve fits given by Eqs. (4.13) and (5.2) are adjusted to make the maxima approach the experimental variance peaks, respectively, assuming z_2 = 40 mm. The quench depth z_1 is varied to minimize the mean square error between the model given in Eq. (5.2) and the experimental curve. For the results shown in Fig. 5.5, the best fit values for z_1 is 12.5 mm. It can be seen that the theoretical SSR curve given by Eq. (5.2) matches well

Table 5.1: Measured variance peaks corresponding with different water paths.

Water Path W_p(mm)	12.6	18.6	23.1
Peak Locations (mm)	9.62	8.05	7.06
Peak Value	0.00894	0.00802	0.00703

with the spatial variance curve from the tread surface. A small mismatch between the experimental curves and the curve fits is observed around the curve tails (below 20 mm), which might be the result of multiple scattering. The result demonstrates the dependence of ultrasonic scattering on the lamellar microstructure with grains.

The tread surface was rescanned with increasing material paths to further verify the gradation of lamellar spacing in the radial direction and to estimate the quench depth z_1. Fig. 5.6 shows the spatial variance curves measured from the tread surface with respect to different material paths. It can be seen that the spatial variance amplitude increases when the material path increases (corresponding to a deeper focus). The variance peaks marked with A_1-A_3 shift to deeper locations (later times). The experimental results show a good agreement with the theoretical ones shown in Fig. 5.3. Table 5.1 shows the measured variance amplitudes and peak positions with respect to different material paths.

The mean square error between the experimental and the theoretical variance curves given in Eq. (5.2) is used to evaluate the curve fit while changing the quench depth z_1. Fig. 5.7 demonstrates the the distribution of the mean square error versus the quench depth z_1 with respect to different material paths. It can be seen that the estimated quench depth which corresponds to the minimum error shifts to a larger value as the material path increases. Fig. 5.8 shows the spatial variance curves normalized by the variance peaks with respect to different material paths along with the curve fits, respectively. The solid lines represent the experimental variance curves

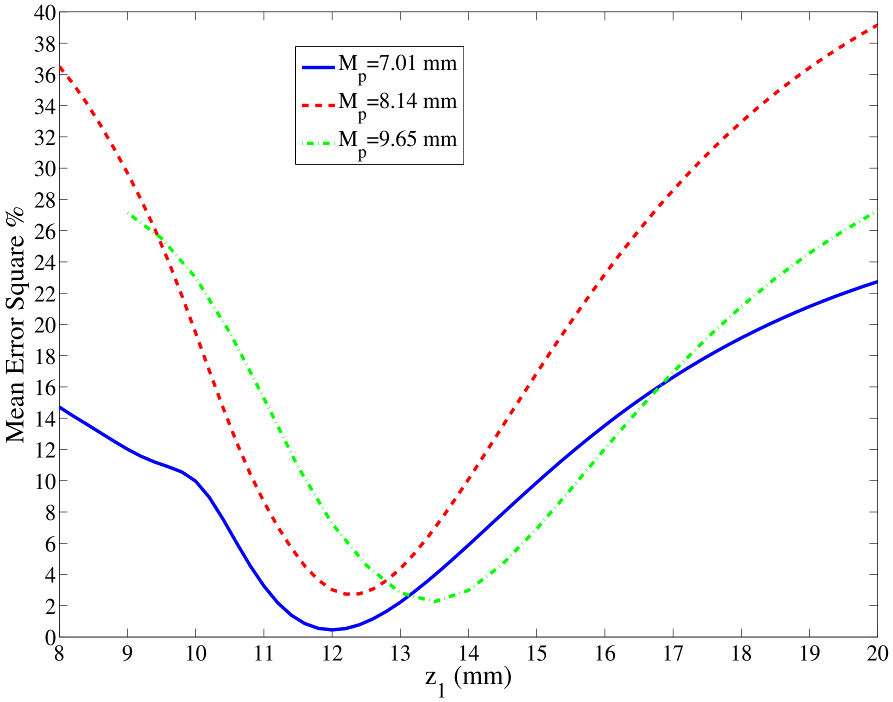

Figure 5.7: The mean error square between experimental variance curve and theoretical curve versus the quench depth z_1.

from the tread surface. The dashed lines indicate the curve fits based on Eq. (5.2). The dependence of lamellar spacing d on depth z shown in Fig. 5.1b is used for the fits. The quench depths z_1 for each fit are chosen to minimize the mean square error between the experimental curves and the model given by Eq. (5.2), respectively. The values of z_1 are equal to 12.0 mm, 12.2 mm and 13.4 mm with respect to the material paths M_p=7.01 mm, 8.14 mm and 9.65 mm, respectively. The sample thickness z_2 is equal to 40 mm. It can be seen that all the spatial variance curves with respect to different material paths match well with the curve fits given by Eq. (5.2), especially when the material path M_p is equal to 7.06 mm. This result shows a best fit for the experimental variance curve, and the error between the experimental curve and the curve fit is smallest. Deeper focal depths result in additional factors not included in

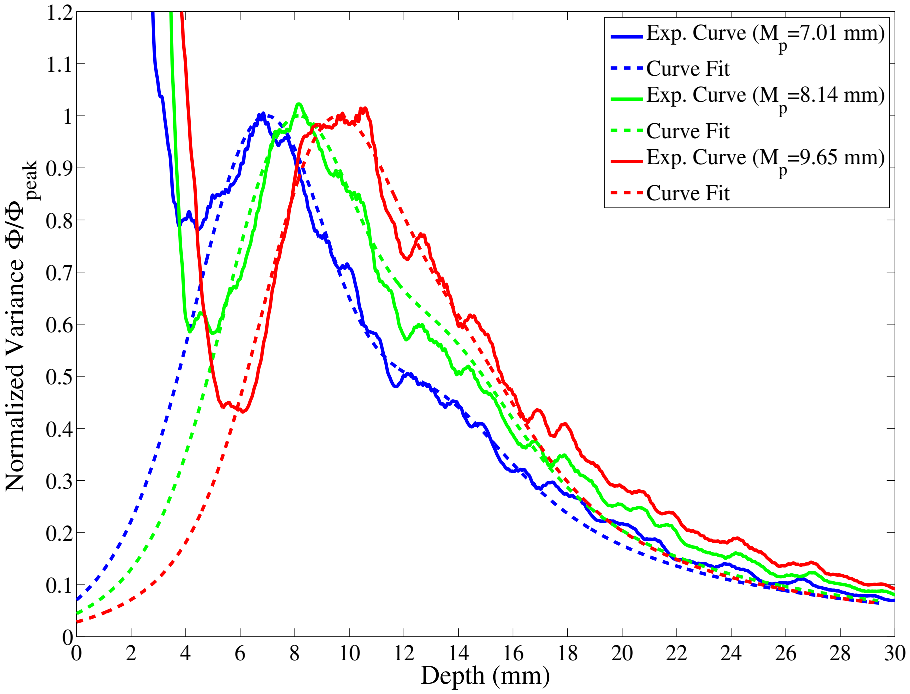

Figure 5.8: The normalized spatial variance curves and corresponding curve fits.

the present model.

By comparing three values of the quench depth z_1 obtained from the fitting procedure, it can also be observed that the chosen material depth can have a strong impact on the estimated quench depth. For these results, when the material depth is in the range of 7-8 mm, the estimated quench depth changes by less than 2 % and is very close to that measured using other methods [67]. However, at the larger material depth of 9.65 mm, the estimated quench depth has an error in z_1 of nearly 12 %. Thus, the most appropriate material path should lie in the range of 7-8 mm, suggesting an optimal material inspection depth of 58-64 % of the expected quench depth. If the material depth is too large, a significant error is observed in the quench depth estimate. The reasons for this error are still under investigation.

5.4 Summary

A modified singly-scattered response (SSR) model that accounts for the gradation of the duplex microstructure within grains in the propagation direction has been expanded based on the previous SSR model. An important parameter, the quench depth was introduced in the new SSR model. The fine lamellar duplex microstructure characterized by lamellar spacing d ($d << L$) appears within the quench depth, while the lamellar spacing d of the coarse duplex microstructure increases beneath the quench depth. Experiments were conducted in a water tank using a 10 MHz transducer incident normal to tread surface and cross section of a quenched railroad wheel slice sample, respectively. The effect of graded lamellar duplex microstructure on ultrasonic scattering has been observed by comparing the spatial variance curve from tread surface with that from the cross section. The spatial variance amplitudes were very similar due to the approximate match of the focal zones. The difference between the two spatial variance curves was larger after the variance peak, which is attributed to the stronger scattering from the increased lamellar spacing on the propagation path (in the radial direction).

The newly modified SSR model given in Eq. (5.2) fit the spatial variance curve from the tread surface much better than the SSR model without the microstructural gradation. As the water paths decrease (deeper focus), the spatial variance amplitudes increase and the variance peaks shift to deeper locations. The experimental results showed a good agreement with the theoretical model. Minimizing the mean square error between the experiments and the model allows the quench depth to be determined. The results demonstrate that the material path is an important parameter which can influence the accuracy of the quench depth measurement.

The results presented in this chapter show that the quench depth in railroad wheels can be accurately estimated using the diffuse ultrasonic backscatter technique. The quench depth is an important predictor of wheel performance during service and knowledge of the depth is very important. Thus, quality control applications may be possible during manufacturing to ensure the uniformity of the quench depth across a set of production parts.

Chapter 6

Ultrasonic Attenuation in Pearlitic Steel

The dependence of ultrasonic attenuation on the microstructure of materials has been investigated for many years. Attenuation in materials can be caused by both dissipation and scattering [54]. The attenuation by dissipation is attributed to the transformation of energy into heat due to the damping, viscosity, etc. The attenuation induced by scattering is caused by the grain boundaries due to the relative misorientation of the grains. In polycrystalline metals, scattering from grain boundaries is a major source of attenuation [55]. The scattering attenuation highly depends on the grain size, shape, texture and orientation distribution in polycrystalline materials, so that the grain size and the microstructure of polycrystalline materials can often be evaluated by measuring the ultrasonic attenuation [3].

Stanke and Kino [6] and Weaver [7] have developed general methods to model attenuation for equiaxed untextured polycrystalline media of cubic symmetry in all frequency ranges based on the second-order Keller approximation [56]. Ahmed and Thompson [9] extended the Stanke and Kino model [6] to cubic materials with elongated grains and the attenuations were numerically evaluated using an integral solution for the Green's function. Turner [10] and Yang et al. [11] used Weaver's approach [7] to develop attenuation models for textured materials with cubic and hexagonal symmetry grains, respectively. Han and Thompson [48] and Panetta and Thompson [58] studied backscatter and attenuation in titanium alloys with duplex microstructure. They focused on examining the contribution of a second phase called a colony in the large macrograins (prime β grains of cubic symmetry) to backscatter and attenuation. Lobkis and Rokhlin [49] and Yang et al. [66] considered microtextured regions (MTRs) (colonies in the Han and Thompson [48] as the largest size phase that is comprised of a secondary (small size phase) of prime crystallites. The contribution of those crystallites to ultrasonic backscatter and attenuation was neglected in [48]. In chapter 4, the effects of lamellar duplex microstructure in pearlitic steel on ultrasonic backscatter were investigated by comparing cross section measurements for both unquenched and quenched wheels. Chapter 5 discussed the dependence of ultrasonic scattering on the graded lamellar spacing with depth on the propagation path.

In this chapter, expressions for ultrasonic longitudinal and transverse wave attenuations are developed for pearlitic steel with lamellar duplex microstructure based on Weaver's scattering model [7]. The dependence of attenuation on lamellar spacing is studied theoretically and the longitudinal attenuation is measured from the tread surface to deeper locations in a quenched wheel sample. Then the longitudinal attenuation on the whole cross section of the quenched wheel sample is mapped, and the experimental results show a good agreement with the theoretical predictions.

6.1 Theoretical Model

One of the primary results of Weaver [7] was the derivation of attenuation for polycrystalline materials [6]. The general solution for longitudinal α_L and transverse α_T wave attenuations can be expressed as

$$\begin{aligned} \alpha_L &= \alpha_{LL} + \alpha_{LT}, \\ \alpha_T &= \alpha_{TL} + \alpha_{TT}, \end{aligned} \tag{6.1}$$

where

$$\begin{aligned} \alpha_{LL} &= \frac{\pi^2\omega^4}{2c_L^8}\int_{-1}^{+1} \tilde{\eta}^{LL}(\theta_{ps})N_1(\theta_{ps})d\cos\theta_{ps}, \\ \alpha_{LT} &= \frac{\pi^2\omega^4}{2c_L^3c_T^5}\int_{-1}^{+1} \tilde{\eta}^{LT}(\theta_{ps})(N_2(\theta_{ps}) - N_1(\theta_{ps}))d\cos\theta_{ps}, \\ \alpha_{TL} &= \frac{1}{2}(\frac{c_T}{c_L})^2\alpha_{LT}, \\ \alpha_{TT} &= \frac{\pi^2\omega^4}{4c_T^8}\int_{-1}^{+1} \tilde{\eta}^{TT}(\theta_{ps})(N_3(\theta_{ps}) - 2N_2(\theta_{ps}) + N_1(\theta_{ps}))d\cos\theta_{ps}. \end{aligned} \tag{6.2}$$

In Eqs. (6.1) and (6.2), the integrals account for the energy lost in all directions due to scattering. It should be understood that the attenuation described above is not due to a dissipative process. The loss is due entirely to the accumulating phase differences between the disturbances in different heterogeneities that results in destructive interference when averaging over the ensemble. The expressions of attenuation described above can be regarded as due to the scattering of energy out of the incident beam. $\tilde{\eta}^{PQ}, (PQ = LL, TT, LT)$ are the spatial Fourier transforms of the spatial correlation function $w(r) = \exp(-\frac{r}{L})$. This function describes the probability that two randomly chosen points at distance r fall within the same grain, where L is the spatial correlation length (usually associated with the grain size). These transforms are given by

$$\begin{aligned}
\tilde{\eta}^{LL}(\theta_{ps}) &\equiv \tilde{\eta}(\hat{\mathbf{p}}\omega/c_L - \hat{\mathbf{s}}\omega/c_L) = \frac{L^3}{\pi^2[1+2k_L^2L^2(1-\cos\theta_{ps})]^2}, \\
\tilde{\eta}^{TT}(\theta_{ps}) &\equiv \tilde{\eta}(\hat{\mathbf{p}}\omega/c_T - \hat{\mathbf{s}}\omega/c_T) = \frac{L^3}{\pi^2[1+2k_T^2L^2(1-\cos\theta_{ps})]^2}, \\
\tilde{\eta}^{TL}(\theta_{ps}) &\equiv \tilde{\eta}^{LT}(\theta_{ps}) \equiv \tilde{\eta}(\hat{\mathbf{p}}\omega/c_L - \hat{\mathbf{s}}\omega/c_T) = \frac{L^3}{\pi^2(1+k_T^2L^2+k_L^2L^2-2k_Lk_TL^2\cos\theta_{ps})^2}.
\end{aligned} \tag{6.3}$$

where $k_L = \omega/c_L$ and $k_T = \omega/c_T$ are the wavenumbers of longitudinal and transverse waves, respectively. The terms $N_1(\theta_{ps})$, $N_2(\theta_{ps})$ and $N_3(\theta_{ps})$ are the inner products [7] on the eighth-rank covariance tensor $\Xi_{ijkl}^{\alpha\beta\gamma\delta} = \langle C_{\alpha\beta\gamma\delta}C_{ijkl}\rangle - \langle C_{\alpha\beta\gamma\delta}\rangle\langle C_{ijkl}\rangle$. For a crystal with cubic symmetry the inner products are written as [7]

$$\begin{aligned}
N_1(\theta_{ps}) &\equiv \Xi_{ijkl}^{\alpha\beta\gamma\delta}\hat{p}_\alpha\hat{p}_i\hat{s}_\beta\hat{s}_j\hat{p}_\gamma\hat{p}_k\hat{s}_\delta\hat{s}_l \\
&= \frac{\nu^2}{\rho^2}\left(\frac{9}{525}+\frac{6}{525}\cos^2\theta_{ps}+\frac{1}{525}\cos^4\theta_{ps}\right). \\
N_2(\theta_{ps}) &\equiv \Xi_{ijkl}^{\alpha\beta\gamma\delta}\hat{p}_\alpha\hat{p}_i\hat{s}_\beta\hat{s}_j\hat{p}_\gamma\hat{p}_k\delta_{\delta l} \\
&= \frac{\nu^2}{\rho^2}\left(\frac{24}{525}+\frac{12}{525}\cos^2\theta_{ps}\right), \\
N_3(\theta_{ps}) &\equiv \Xi_{ijkl}^{\alpha\beta\gamma\delta}\delta_{\alpha i}\hat{p}_\beta\hat{p}_j\hat{s}_\gamma\hat{s}_k\delta_{\delta l} \\
&= \frac{\nu^2}{\rho^2}\left(\frac{63}{525}+\frac{21}{525}\cos^2\theta_{ps}\right),
\end{aligned} \tag{6.4}$$

where $\nu = c_{11} - c_{12} - 2c_{44}$ is the single crystal anisotropy factor and ρ is the material density.

The correlation functions $\tilde{\eta}^{PQ}(\theta_{ps}), (PQ = LL, TT, LT)$ and the inner products $N_i(\theta_{ps}), (i = 1, 2, 3)$ are applicable only for materials with single-phase polycrystalline grains. The duplex microstructure within grains exhibited in some structural metals is expected to influence the scattering attenuation significantly.

As shown in chapters 4 and 5, a significant dependence of ultrasonic backscatter on lamellar duplex microstructure within grains in railroad wheel steel has been observed. In those chapters, the M-factor model developed by Lobkis et al. [49], [50] for application to the titanium alloy with the duplex microstructure within grains was also used to modify the backscatter coefficient for pearlitic steel, in which the contribution to ultrasonic backscatter from the lamellar duplex crystallites was considered. That approach is used here as well. A schematic of lamellar duplex microstructure (pearlite phase) within grains is shown in Fig. 4.2. k_x and k_y represent the wave numbers in the lamellar plane and normal to the plane, respectively. The final expressions of longitudinal and transverse attenuation coefficients for materials which include the duplex microstructure then are modified as [49], [50], [66]

$$
\begin{aligned}
\alpha^{LL} &= \frac{\pi^2\omega^4}{2c_L^8}\int_{-1}^{+1}\left[(1-M)\tilde{\eta}_r^{LL}(\theta_{ps})N_1^{(r)}(\theta_{ps}) + M\tilde{\eta}_w^{LL}(\theta_{ps})N_1^{(w)}(\theta_{ps})\right] d\cos\theta_{ps},\\
\alpha^{LT} &= \frac{\pi^2\omega^4}{2c_L^3c_T^5}\int_{-1}^{+1}\Bigg[\,(1-M)\tilde{\eta}_r^{LT}(\theta_{ps})(N_2^{(r)}(\theta_{ps}) - N_1^{(r)}(\theta_{ps}))\\
&\qquad\qquad + M\tilde{\eta}_w^{LT}(\theta_{ps})(N_2^{(w)}(\theta_{ps}) - N_1^{(w)}(\theta_{ps}))\,\Bigg] d\cos\theta_{ps},\\
\alpha^{TT} &= \frac{\pi^2\omega^4}{2c_T^8}\int_{-1}^{+1}\Bigg[\,(1-M)\tilde{\eta}_r^{TT}(\theta_{ps})\Big(N_3^{(r)}(\theta_{ps}) - 2N_2^{(r)}(\theta_{ps}) + N_1^{(r)}(\theta_{ps})\Big)\\
&\quad + M\tilde{\eta}_w^{TT}(\theta_{ps})\Big(N_3^{(w)}(\theta_{ps}) - 2N_2^{(w)}(\theta_{ps}) + N_1^{(w)}(\theta_{ps})\Big)\,\Bigg] d\cos\theta_{ps},
\end{aligned}
\tag{6.5}
$$

where $\tilde{\eta}_w^{PQ}(\theta_{ps})$, $(PQ = LL, TT, LT)$ represent the Fourier transforms of the correlation functions for lamellar duplex microstructure within grains. The subscripts r and w indicate the terms for grain boundaries and duplex microstructure within grains, respectively. The general correlation function for the ellipsoidal grain [50] is used for lamellar duplex microstructure within an individual grain shown in Fig. 4.2. In this case,

$$\begin{aligned}
\tilde{\eta}^{LL}(k) &= \frac{a_x a_y a_z}{\pi^2 \left\{ 1 + 2\displaystyle\sum_{x,y,z}^{3} (k_i^L)^2 (1 - \cos\theta_{ps}) a_i^2 \right\}} \\
&= \frac{a_x a_y a_z}{\pi^2 \left[1 + (1 - \cos\theta_{ps}) k_L^2 \langle l^2 \rangle\right]^2}, \\
\tilde{\eta}^{TT}(k) &= \frac{a_x a_y a_z}{\pi^2 \left\{ 1 + 2\displaystyle\sum_{x,y,z}^{3} (k_i^T)^2 (1 - \cos\theta_{ps}) a_i^2 \right\}} \\
&= \frac{a_x a_y a_z}{\pi^2 \left[1 + (1 - \cos\theta_{ps}) k_T^2 \langle l^2 \rangle\right]^2}, \\
\tilde{\eta}^{LT}(k) &= \frac{a_x a_y a_z}{\pi^2 \left\{ 1 + \displaystyle\sum_{x,y,z}^{3} [(k_i^L)^2 + (k_i^T)^2] (1 - \cos\theta_{ps}) a_i^2 \right\}} \\
&= \frac{a_x a_y a_z}{\pi^2 \left[1 + (k_L^2 + k_T^2 - 2k_L k_T \cos\theta_{ps}) \langle l^2 \rangle\right]^2},
\end{aligned} \tag{6.6}$$

where a_x, a_y and a_z are the correlation lengths of the duplex crystallite within microtextural regions (MTRs) in the x, y and z directions, respectively [50]. The denominator in Eq. (6.6) may be given by $[1 + (1 - \cos\theta_{ps})k^2\langle l^2\rangle]^2$ where $\langle l \rangle = \sqrt{n_x^2 a_x^2 + n_y^2 a_y^2 + n_z^2 a_z^2}$ is defined as the interaction length. It is the effective interactive length in the direction of wave propagation and $\hat{\mathbf{n}}$ is the wave vector normal. As described in chapter 4, a_x and a_z are assumed independent of the positions within an individual grain. In that case, it can be assumed $a_x = a_z = L$ and $a_y = d$ for the duplex crystallites in the x, z and y directions, respectively. Here, the duplex crystallites within grains are also assumed to be oriented randomly such that the angle θ shown in Fig. 4.2 varies with equal probability between 0 to π. The square average of the interaction length is given by

$$\langle l^2 \rangle = \frac{1}{\pi}\int_0^{\pi} (\sin^2\theta L^2 + \cos^2\theta d^2)d\theta = (L^2+d^2)/2. \tag{6.7}$$

Substituting Eq. (6.7) into Eq. (6.6) the average spatial correlation functions for lamellar duplex microstructure can be expressed as [67]

$$\begin{aligned}
\tilde{\eta}_w^{LL}(\theta_{ps}) &= \frac{L^2 d}{\pi^2[1+(1-\cos\theta_{ps})k_L^2(L^2+d^2)]^2}, \\
\tilde{\eta}_w^{TT}(\theta_{ps}) &= \frac{L^2 d}{\pi^2[1+(1-\cos\theta_{ps})k_T^2(L^2+d^2)]^2}, \\
\tilde{\eta}_w^{LT}(\theta_{ps}) &= \frac{L^2 d}{\pi^2[1+(k_L^2+k_T^2-2k_Lk_T\cos\theta_{ps})(L^2+d^2)/2]^2}.
\end{aligned} \tag{6.8}$$

By substituting Eqs. (6.3) and (6.8) into the Eq. (6.5), the final attenuation coefficients for materials with lamellar duplex microstructure within grains can be expressed as

$$\begin{aligned}
\alpha_{LL} &= \frac{\omega^4}{2c_L^8}\int_{-1}^{+1}\Bigg[\frac{(1-M)L^3N_1^{(r)}(\theta_{ps})}{[1+2k_L^2L^2(1-\cos\theta_{ps})]^2} \\
&\qquad + \frac{ML^2dN_1^{(w)}(\theta_{ps})}{[1+(1-\cos\theta_{ps})k_L^2(L^2+d^2)]^2}\Bigg]d\cos\theta_{ps}, \\
\alpha_{LT} &= \frac{\omega^4}{2c_L^3c_T^5}\int_{-1}^{+1}\Bigg[\frac{(1-M)L^3(N_2^{(r)}(\theta_{ps})-N_1^{(r)}(\theta_{ps}))}{[1+k_T^2L^2+k_L^2L^2-2k_Lk_TL^2\cos\theta_{ps}]^2} \\
&\qquad + \frac{ML^2d(N_2^{(w)}(\theta_{ps})-N_1^{(w)}(\theta_{ps}))}{[1+(k_L^2+k_T^2-2k_Lk_T\cos\theta_{ps})(L^2+d^2)/2]^2}\Bigg]d\cos\theta_{ps}, \\
\alpha_{TT} &= \frac{\omega^4}{2c_T^8}\int_{-1}^{+1}\Bigg[\frac{(1-M)L^3\left(N_3^{(r)}(\theta_{ps})-2N_2^{(r)}(\theta_{ps})+N_1^{(r)}(\theta_{ps})\right)}{[1+2k_T^2L^2(1-\cos\theta_{ps})]^2} \\
&\qquad + \frac{ML^2d\left(N_3^{(w)}(\theta_{ps})-2N_2^{(w)}(\theta_{ps})+N_1^{(w)}(\theta_{ps})\right)}{[1+(1-\cos\theta_{ps})k_T^2(L^2+d^2)]^2}\Bigg]d\cos\theta_{ps}, \\
\alpha_{TL} &= \frac{c_T^2}{2c_L^2}\alpha_{LT}.
\end{aligned} \tag{6.9}$$

When the lamellar spacing d approaches L (the lamellar duplex microstructure is absent), Eqs. (6.9) reduce to the previous theoretical attenuation expressions for a single phase material [7]. In the next section, the dependence of ultrasonic attenuation on the parameter M and the lamellar spacing d is discussed based on the developed model given by Eqs. (6.9).

6.2 Model Results

In order to show example results, several parameters given in Eqs. (6.1) and (6.9) required for the model must be first be determined (including the sound speeds in water and in steel as well as the single crystal elastic constants of pure iron). The numerical values used in the model are listed in Table 6.1. The inner products $N_1^{(w)}(\theta_{ps})$, $N_2^{(w)}(\theta_{ps})$ and $N_3^{(w)}(\theta_{ps})$ on the eighth-rank covariance tensor for lamellar duplex microstructure within grains are assumed to be equal to $N_1^{(r)}(\theta_{ps})$, $N_2^{(r)}(\theta_{ps})$ and $N_3^{(r)}(\theta_{ps})$. Fig. 6.1 shows the calculated attenuation quantities α_{LL}, α_{LT} and α_{TT} as a function of frequency by fixing L=24 μm, d=2.0 μm and M=0.9. It can be seen that all the quantities increase with frequency following a similar trend. The attenuation α_{LT} is much higher than α_{LL}, while α_{TT} is much larger than α_{TL}, results that indicate that the longitudinal-to-transverse attenuation α_{LT} and the transverse-

Table 6.1: Single crystal elastic constants of iron used in the formulation of attenuation given in Eqs. (6.9).

Elastic Constants c_{ij} (GPa)			Velocity (m/s)		
c_{11}	c_{12}	c_{13}	c_f	c_L	c_T
229.3	134.1	116.7	1486	5973	3250

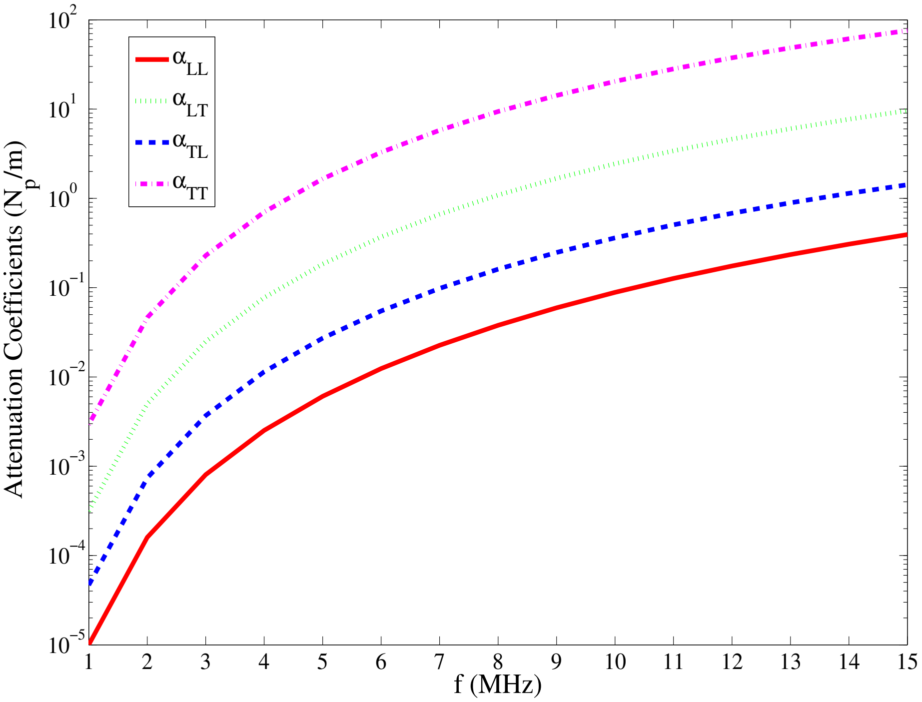

Figure 6.1: The attenuation components α_{LL}, α_{LT}, α_{TL} and α_{TT} versus frequency. (L=24 μm, d=2.0 μm and M=0.9)

.

to-transverse attenuation α_{TT} are the primary contributors to the longitudinal and transverse attenuations, respectively.

The attenuation coefficients given by Eq. (6.9) contain three unknown variables M, d and L. The dependence of attenuation coefficients on the parameter M and the lamellar spacing d are investigated by fixing $L = 24$ μm. Figs. 6.2a and 6.2b show the calculated longitudinal and transverse attenuation coefficients versus frequency by varying the parameter M and the lamellar spacing d, respectively. The parameter $M = 0$ indicates that duplex microstructure within grains is absent, $M = 1.0$ indicates that the scattering from grain boundaries is neglected. It can be seen that both longitudinal and transverse attenuation coefficients follow a similar trend with increasing either the parameter M or the lamellar spacing d.

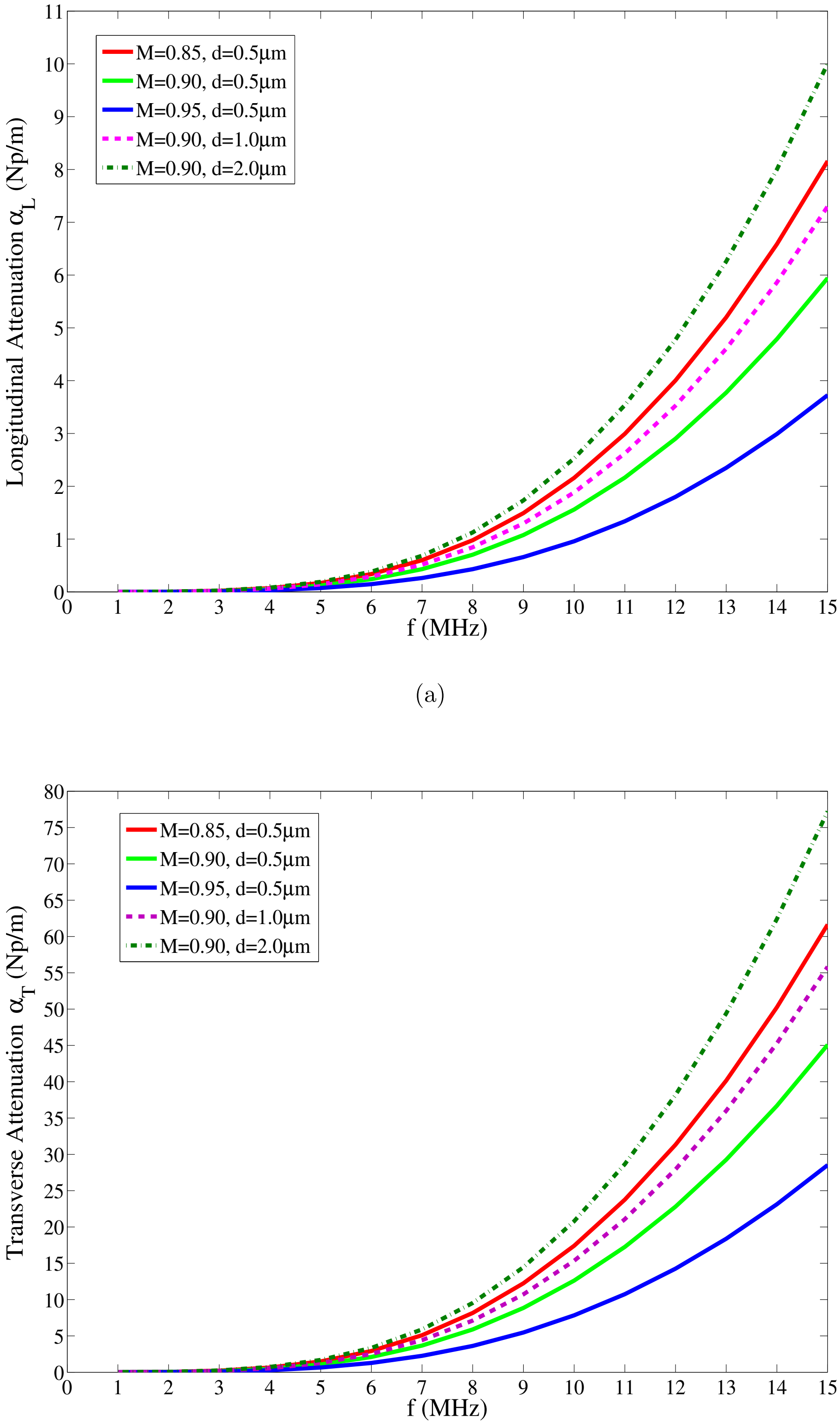

(a)

(b)

Figure 6.2: The effects of the parameters M and d on (a) longitudinal attenuation, (b) transversal attenuation (L=24 μm).

6.3 Experiments

The longitudinal attenuation was measured from the tread surface to deeper locations to examine the influence of pearlite on the longitudinal attenuation. Attenuation measurements were conducted by the pulse-echo immersion technique at normal incidence to the cross section of a quenched railroad wheel sample shown in Fig. 6.3. The thickness of the wheel sample was measured as 12.51 mm with a digital micrometer. The sample was prepared by grinding using the SiC papers through 600 grit. The polishing was performed using a SiC paper through 1500 grit. Ultrasonic pulses generated by a DPR 300 pulser/receiver (*Imaginant and JSR Ultrasonics*, Pittsford, NY) were transmitted and received by the same transducer operating in pulse-echo mode. A low gain (25 dB) was used (A/D sampling rate = 2 GHz). An unfocused plane wave transducer (model: Panametrics A327S, 0.375 inch element diameter, *Olympus*

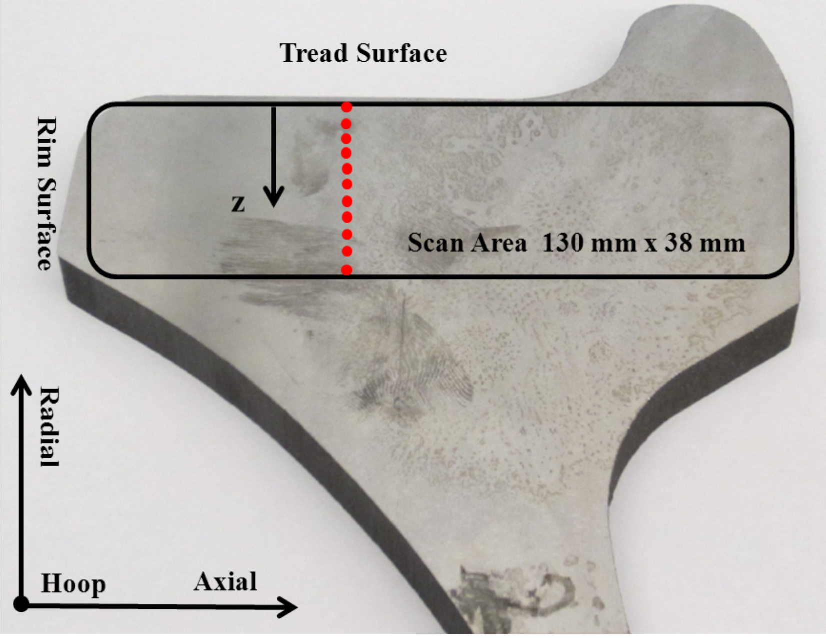

Figure 6.3: An image of cross section of an unquenched railroad wheel sample (manufactured by *Griffin Wheel. Inc.*).

Panametrics, Inc., Waltham, MA) with 10 MHz central frequency was used in the experiment. The transducer was set 50 mm away from the top surface of the wheel sample and aligned carefully to normal incidence. Fig. 6.4 demonstrates a front wall reflected from the top surface and four successive backwalls reflected from the back surface. Four gates marked with different colors indicate the times for the Fourier transform calculation. Fig. 6.5 shows the frequency spectra of the reflected successive

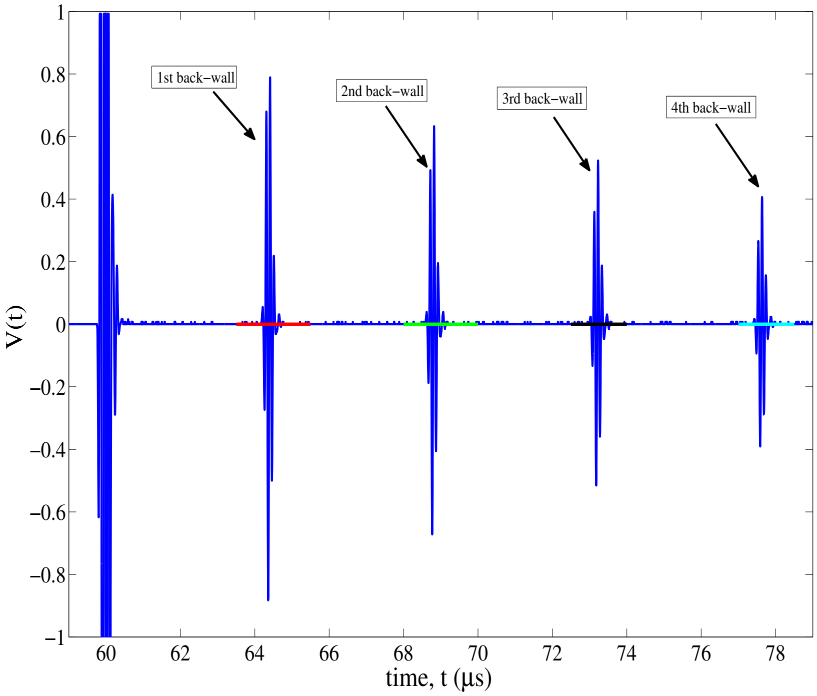

Figure 6.4: Signal used for attenuation calculation (An unfocused transducer with 10 MHz central frequency).

backwall reflections. Longitudinal attenuation α_L is obtained by calculating the ratio of the spectral component of the first backwall reflection wave to that of the second one. The attenuation, α_L is determined by [53],

$$\alpha_L = \frac{1}{2h}\left[\ln\frac{|E_1(\omega)|}{|E_2(\omega)|} - \ln\left(\frac{D_{R_1}(\omega)}{D_{R_2}(\omega)R_{12}^2}\right)\right], \tag{6.10}$$

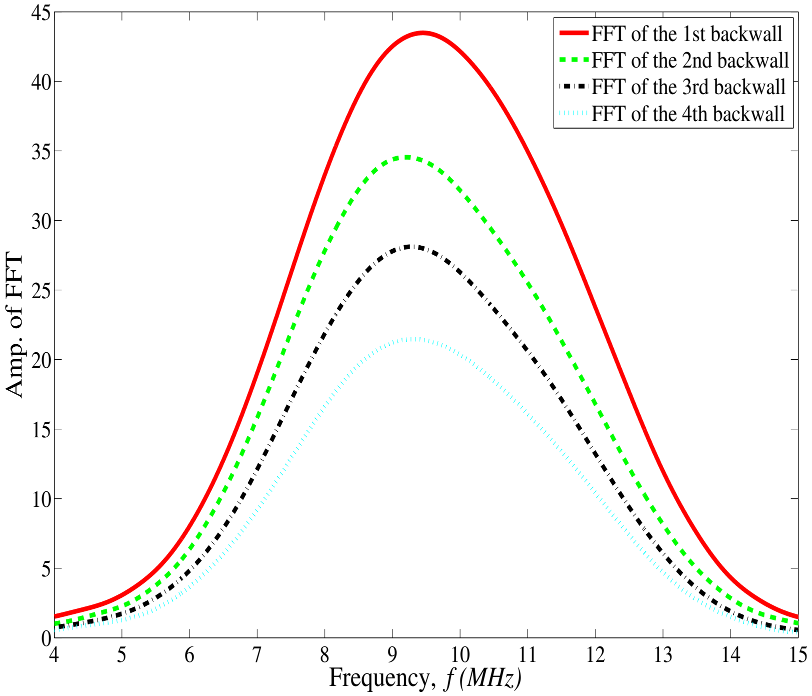

Figure 6.5: FFT of the back wall reflections shown in Fig. 6.4.

where $E_1(\omega)$ and $E_2(\omega)$ are the frequency spectra of the first and second reflections from the back surface shown in Fig. 6.5, and h is the thickness of the wheel sample. The second term in Eq. 6.10 indicates the energy lost due to diffraction at the back surface. D_{R_1} and D_{R_2} are the Lommel diffraction corrections at the first and second backwall reflections, respectively [72]. $R_{12} = (\rho_L c_L - \rho_f c_f)/(\rho_L c_L + \rho_f c_f)$ defines the reflection coefficient. The subscripts 1 and 2 designate water and sample, respectively. The red circles shown in Figure 6.3 which are about two inches away from the rim surface represent the locations where the longitudinal attenuation was measured. Fig. 6.6 shows the measured longitudinal attenuation α_L versus frequency for different depths z from the tread surface. It can be seen that the measured longitudinal attenuation is smallest near the tread surface and increases at deeper locations. This result is attributed to the stronger scattering from the increasing lamellar spacing

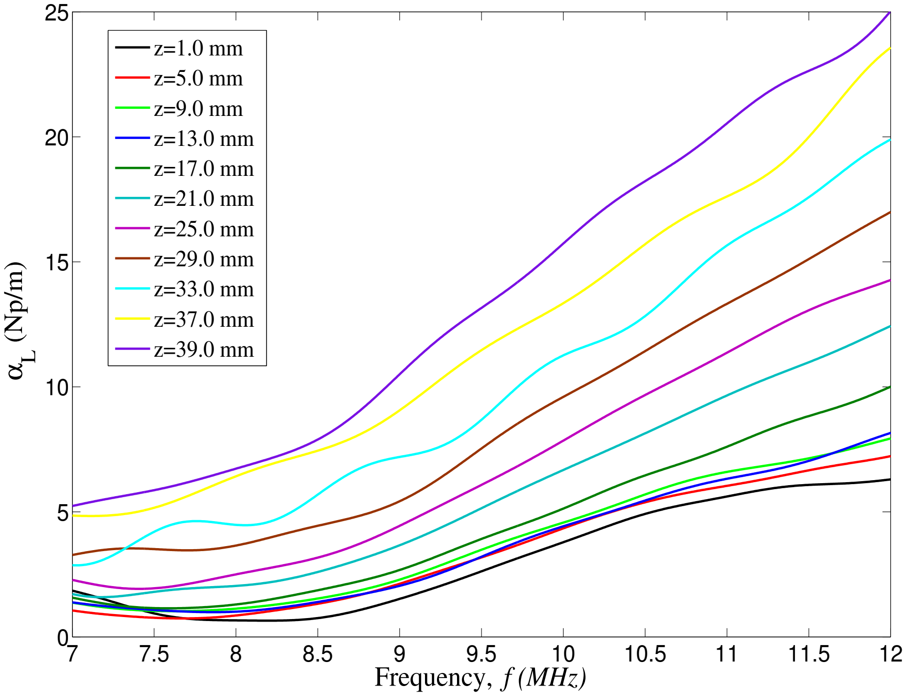

Figure 6.6: Experimental attenuation versus frequency with respect to different positions (shown in Fig 6.3).

within grains. By comparing Fig. 6.2a with Fig. 6.6, it can be observed that not only the profiles of the theoretical longitudinal attenuation based on Eqs. (6.9) agree with the experimental ones, but also the values of the calculated longitudinal attenuation are close to those from experiments.

Fig. 6.7 shows the distribution from the tread surface to deeper locations of the longitudinal attenuation at 10 MHz. The solid green line represents the measured longitudinal attenuation. It can be seen clearly that the longitudinal attenuation increases from the tread surface to deeper locations. The value of longitudinal attenuation is relatively constant within around 13 mm depth, which implies that the pearlite microstructure is relatively uniform. This depth is consistent with the quench depth in a railroad wheel which was obtained from the spatial variance curve from

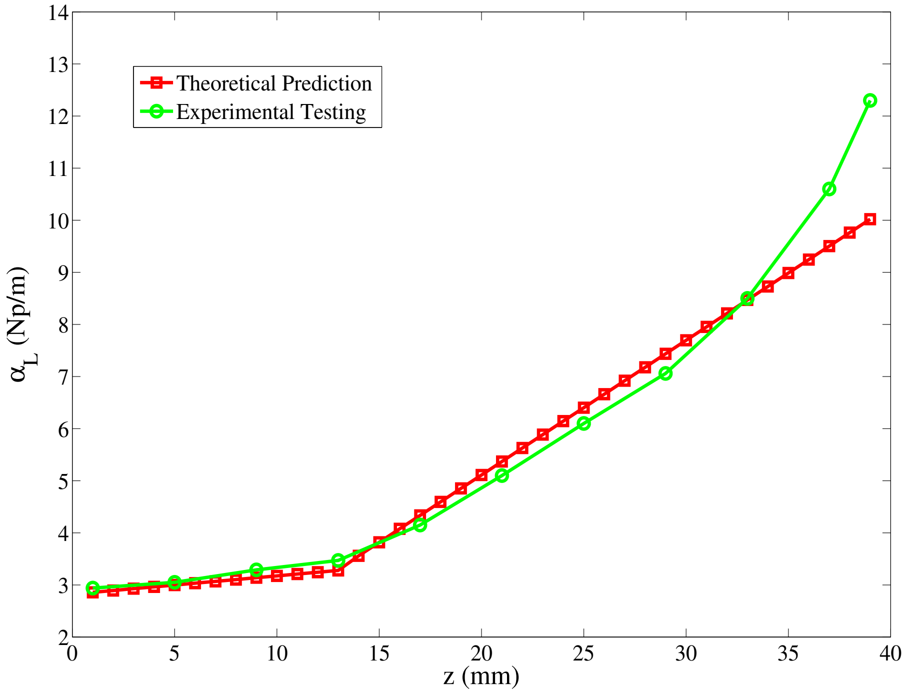

Figure 6.7: Distribution of attenuation coefficients from quenched surface to deeper locations with respect to f=10 MHz.

the tread surface given in chapter 5. Beneath the quench depth, the longitudinal scattering attenuation increases linearly due to the coarse lamellar spacing. The red line demonstrates the longitudinal attenuation calculated by Eqs. (6.9). The correlation length L was chosen as 24 μm based on the ultrasonic backscatter measurements from an unquenched wheel while fixing M=0.9. The lamellar spacing d ranges from 0.5 μm to 1.0 μm within the quench depth, then it increases linearly from 1.0 μm 24 μm along the z direction as described in chapters 4 and 5. At deeper locations, it is considered that the lamellar spacing d approaches L, which implies that the lamellar duplex microstructure is absent. By comparing these two curves, it can be seen that the theoretical predictions show a good agreement with the experimental results for depths less than 32 mm. The difference between the two curves increases after this depth, a result which might be attributed to larger grains at deeper locations or much lower scattering from pearlite within grains compared to the scattering from grain boundaries due to the large lamellar spacing ($d \approx L$). More work is needed to identify the source of this difference.

To map the distribution of the longitudinal attenuation, the cross section of the quenched wheel sample was scanned using an unfocused transducer with a 10 MHz central frequency (Panametrics A327s, *Olympus Panametrics, Inc.*). The scan area (130 mm × 38 mm) is shown in Fig. 6.3, with the scan resolution and speed set to 4.0 mm/step and 1.0 mm/s, respectively. Fig. 6.8 demonstrates the distribution of the measured longitudinal attenuation (10 MHz) with respect to positions on the whole cross section of the quenched wheel sample. The color bar ranges from 2.75 to 12.5 Np/m. The results show that the longitudinal attenuation increases from the quenched surfaces (including both the tread surface and rim surface) to deeper locations. The dashed red line shown in Fig. 6.8 corresponds with the longitudinal attenuation illustrated in Fig. 6.8. The experimental results demonstrate a large dependence of the ultrasonic longitudinal attenuation on lamellar duplex microstructure (pearlite phase) within grains.

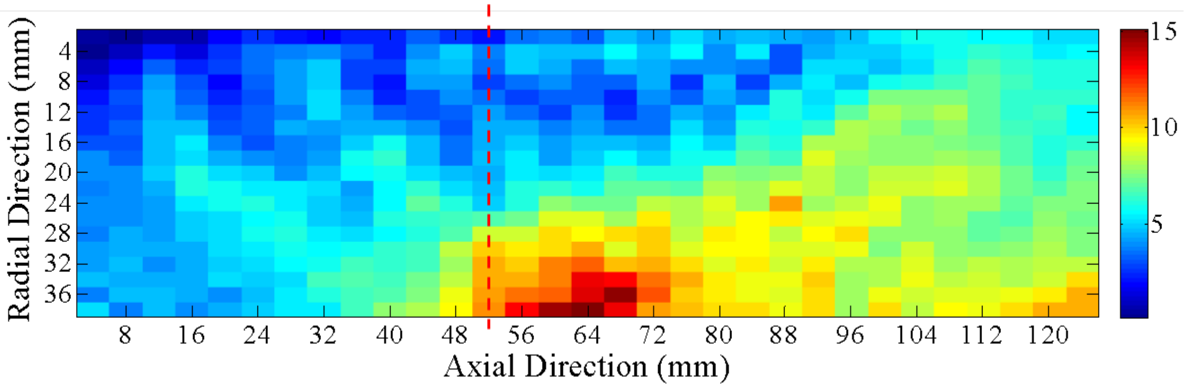

Figure 6.8: Attenuation map of the cross section of a quenched railroad wheel sample.

6.4 Summary

In this chapter, expressions for ultrasonic longitudinal and transverse attenuations were developed based on the Weaver's scattering attenuation model [7] for pearlitic railroad wheel steel. The dependence of the lamellar spacing on ultrasonic longitudinal and transverse attenuation was investigated. The attenuation measurements were conducted in a water tank using an unfocused transducer with a central frequency 10 MHz on the cross section of a quenched railroad wheel sample. The results show that the measured longitudinal attenuation drops dramatically near the tread surface, an outcome that is attributed to the fine lamellar duplex microstructure (pearlite phase) created via the quenching process. The longitudinal attenuation value remains relatively constant within the quench depth (about 13 mm), which is consistent with diffuse ultrasonic backscatter measurements from the tread surface presented in chapter 5. Then it increases approximately linearly due to the change in lamellar spacing. The experimental results demonstrate a good agreement with the theoretical prediction. The whole cross section of the quenched wheel sample was scanned to display the distribution of the longitudinal attenuation as a function of positions. Ultrasonic attenuation gives an important non-destructive method to evaluate duplex microstructure within grains which can be implemented for quality control in conjunction with other manufacturing processes.

Chapter 7

Mode-converted Diffuse Backscatter in Pearlitic Steel

In chapters 4, 5 and 6, the effects of lamellar duplex microstructure within grains on ultrasonic scattering were studied using the L-L mode in a pulse-echo configuration. In this chapter, a new mode-converted (longitudinal-to-transverse, L-T) singly-scattered response (SSR) model is expanded based on the previous L-T SSR model developed by Hu et al. [69] for application to pearlitic steel. The effects of lamellar spacing on ultrasonic scattering are investigated using both the L-L ultrasonic backscatter and the L-T ultrasonic backscatter measured in two different directions, respectively. The experimental results show that the L-T variance amplitudes measured on the cross section of a quenched wheel sample exhibit a large dependence on the measurement direction, a result which is attributed to an angular variation of the effective interaction lengths in different directions. The lamellar spacing d and the correlation length L can be estimated simultaneously with the developed L-T scattering model and the L-T variance amplitudes measured in two directions.

7.1 Theoretical Model

Chapters 4 and 5 described a new SSR model that included the lamellar duplex microstructure within grains using the (longitudinal-to-longitudinal, L-L) mode based on the previous SSR model described in chapter 3 for applications to quenched pearlitic steel. Recently, Hu et al. [69] developed a mode-converted (longitudinal-to-transverse, L-T) SSR model to examine how the normal incidence longitudinal wave converts to the scattered shear waves at grain boundaries. Fig. 7.1 shows a schematic of the mode-converted (L-T) SSR model using a pitch-catch transducer configuration. The normal incidence transducer behaves as a source transducer, while the oblique incidence one functions as the receiving transducer. The quantities $z_{f\xi}$ and z_ξ, $(\xi = S, R)$ represent the water and material paths for the source and receiving transducers, respectively. Fig. 7.2 demonstrates the coordinate systems defined in the model. $\mathbf{x}$ and $\mathbf{X}$ represent the longitudinal and transverse wave paths, respectively.

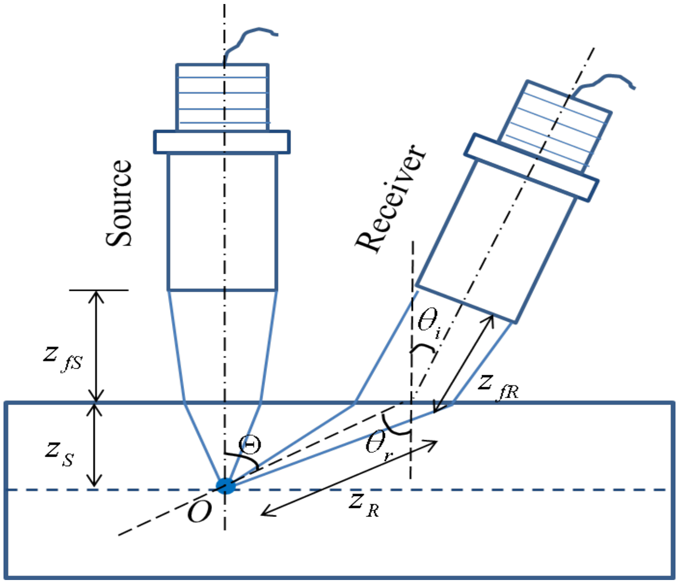

Figure 7.1: A schematic of the mode-converted (L-T) ultrasonic backscatter using a pitch-catch transducer configuration (adapted from [69]).

The relationship between the two coordinates is given by

$$\left\{\begin{aligned} X &= x\cos\Theta + z\sin\Theta - z_s\sin\Theta, \\ Y &= y, \\ z &= -x\sin\Theta + z\cos\Theta + z_s\sin^2\Theta/\cos\Theta, \end{aligned}\right. \tag{7.1}$$

where Θ is defined as the angle between the normal incident longitudinal wave unit vector $\hat{\mathbf{p}}_0$ and the scattered shear wave unit vector $\hat{\mathbf{s}}_0$. The mode-converted L-T model reduces to the L-L model described in chapter 3 when $\Theta = 0$. The unit vector $\hat{\mathbf{s}}_\perp$ represents the polarization direction of the scattered shear wave. θ_i and θ_r indicate the incident and refraction angles for the receiving transducer, respectively. The coordinates $\mathbf{x}$ and $\mathbf{X}$ represent the longitudinal and transverse propagation paths for the source and receiving transducers. The final expression of the mode-converted L-T

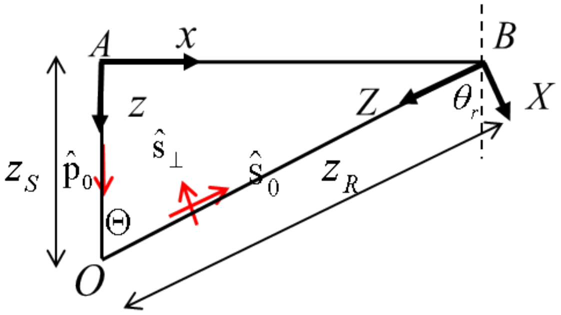

Figure 7.2: The geometrical relationship for coordinate transformation.

SSR model is given by [69]

$$\begin{aligned}
\Phi^{LT}(t) = \Phi_0^{LT} K^{LT} \int_0^\infty dz \int_{-\infty}^{\infty} dx \exp(-\frac{t^2}{\sigma_S^2}) \frac{w_{0R}^2}{w(z) w_1(Z) \sqrt{w^2(z) + w_2^2(Z)}} \\
\times \exp\left[-\frac{2x^2}{w^2(z)} - \frac{2X^2}{w_1^2(z)} - \frac{2z^2}{\sigma_S^2 c_L^2} - \frac{2Z^2}{\sigma_S^2 c_T^2} + \frac{4Zt}{\sigma_S^2 c_T} \right] \\
\times \exp\left[\frac{1}{\sigma_S^2} \left(\frac{Z}{c_T} - \frac{z}{c_L} \right)^2 - \frac{2t}{\sigma_S^2} (\frac{Z}{c_T} - \frac{z}{c_L}) - 2\alpha_L z - 2\alpha_T Z \right],
\end{aligned} \tag{7.2}$$

with

$$\begin{aligned}
\Phi_0^{LT} = V_{max}^S V_{max}^R \frac{\pi \sqrt{\pi} \omega_0^4 \sigma_S}{8 \sigma_R c_L^4 c_T^4} \frac{w(z_{FS}) w(z_{FR})}{w_{0R}^2} \left(\frac{\rho c_L c_T}{\rho_f c_f^2} \right)^2 \\
\times \frac{\cos^2(\Theta - \theta_i) T_{fL}^2 T_{Tf}^2}{R_{ff}^2 D_S(\omega_0) D_R(\omega_0)} \\
\times \exp(2\alpha_f z_{FS} + 2\alpha_f z_{FR} - 2\alpha_f z_{fS} - 2\alpha_f z_{fR}).
\end{aligned} \tag{7.3}$$

The integration is over both x and z coordinates in contrast with the single integral in the normal incidence L-L SSR model due to the symmetry. Here, ρ_f and c_f are the density and wave speed in the fluid, respectively, and ρ, c_L and c_T are the density, longitudinal and shear wave speeds in solid, respectively. $\sigma_\xi, (\xi = S, R)$ represents the temporal pulse width for the source or receiving transducers. $D_\xi(\omega_0), (\xi = S, R)$ are the diffraction corrections for the source and receiving transducers [8], respectively. $T_{Tf} = 4\rho_f^2 c_f^2/(\rho^2 c_T^2 + \rho\rho_f c_f c_T)$ is the transmission coefficient from the shear mode in the solid to the fluid for the receiving transducer. $w_{0\xi}, (\xi = S, R)$ are the effective initial beam widths of the source and receiver transducers, respectively. $w(z)$ and $w_i(z)(i = 1, 2)$ represent the widths of the Gaussian profile for the source and receiving transducers in x, y directions in terms of the propagation depth z, respectively. For the normal incidence L-L mode at a planar surface utilized in chapters 4 and 5, the Gaussian beam widths are equal, $w(z) = w_i(z)$. $w(z_{F\xi}), (\xi = S, R)$ are the Gaussian beam widths at the focal length for the source and receiver transducers, respectively, and $z_{F\xi}, (\xi = S, R)$ are the water paths between the transducer faces and a planar reflector for the source and receiving transducers, respectively, from which the reflected amplitudes $V^{\xi}_{max}, (\xi = S, R)$ are measured during calibration. All other terms have already been described in chapter 4.

The L-T backscatter coefficient is written as

$$K^{LT} = \tilde{\eta}^{LT}(\pi - \Theta)\Xi^{\cdots\hat{\mathbf{p}}_0\hat{\mathbf{p}}_0\hat{\mathbf{s}}_0\hat{\mathbf{s}}_\perp}_{\cdots\hat{\mathbf{p}}_0\hat{\mathbf{p}}_0\hat{\mathbf{s}}_0\hat{\mathbf{s}}_\perp}(\pi - \Theta). \tag{7.4}$$

It contains two terms. The spatial Fourier transform of the correlation function $\eta(\mathbf{x} - \mathbf{y})$ which describes the probability that two randomly chosen points, $\mathbf{x}$ and $\mathbf{y}$, lie in a region of the material that has uniform properties, and is given by

$$\tilde{\eta}^{LT}(\pi - \Theta) = \frac{L^3}{\pi^2[1 + k_T^2 L^2 + k_L^2 L^2 - 2k_L k_T L^2 \cos(\pi - \Theta)]^2}, \tag{7.5}$$

where L is is defined as the spatial correlation length (usually associated with the grain size). The covariance function can be written as

$$\Xi^{\cdots\hat{\mathbf{p}}_0\hat{\mathbf{p}}_0\hat{\mathbf{s}}_0\hat{\mathbf{s}}_\perp}_{\cdots\hat{\mathbf{p}}_0\hat{\mathbf{p}}_0\hat{\mathbf{s}}_0\hat{\mathbf{s}}_\perp}(\pi - \Theta) = \frac{\nu^2}{\rho^2}\left[\frac{10}{525} + \frac{\cos^2(\pi - \Theta)}{525} - \frac{\cos^4(\pi - \Theta)}{525}\right]. \tag{7.6}$$

In chapters 4, 5 and 6, it was observed that the duplex microstructure within grains in pearlitic steel influenced the ultrasonic scattering significantly. The backscatter coefficient K^{LT} given in Eq. (7.4) is only applicable for texture free materials with single-phase polycrystalline grains. Thus it must be modified here to include the contribution from the duplex microstructure within grains. Fig. 7.3a demonstrates a schematic of the lamellar duplex microstructure in an individual spherical grain.

Figs. 7.3b and 7.3c show the cross sectional features of the spherical grain with lamellar duplex microstructure in the 1-3 and 1-2 planes, respectively. It can be observed that the cross section features are not only related to the orientation angle θ, but also are dependent on the inspection direction. By applying the M-factor backscatter model stated in chapters 4, 5 and 6 for the pearlitic steel, the total backscatter coefficient accounting for the misorientation of duplex microstructure within grains is modified as

$$\begin{aligned} K_i^{LT} &= (1-M)\tilde{\eta}_r^{LT}(\pi-\Theta)[\Xi^{\cdots\hat{\mathbf{p}}_0\hat{\mathbf{p}}_0\hat{\mathbf{s}}_0\hat{\mathbf{s}}_\perp}_{\cdots\hat{\mathbf{p}}_0\hat{\mathbf{p}}_0\hat{\mathbf{s}}_0\hat{\mathbf{s}}_\perp}(\pi-\Theta)]_r \\ &+ M\tilde{\eta}_{w_i}^{LT}(\pi-\Theta)[\Xi^{\cdots\hat{\mathbf{p}}_0\hat{\mathbf{p}}_0\hat{\mathbf{s}}_0\hat{\mathbf{s}}_\perp}_{\cdots\hat{\mathbf{p}}_0\hat{\mathbf{p}}_0\hat{\mathbf{s}}_0\hat{\mathbf{s}}_\perp}(\pi-\Theta)]_{w_i}, \end{aligned} \tag{7.7}$$

where $\tilde{\eta}_{w_i}^{LT}(\pi-\Theta)$ is the spatial Fourier transform of the correlation function for the duplex microstructure shown in Figs. 7.3b and 7.3c. As described in chapter 4, the correlation function for ellipsoidal grains [49], [50] $\tilde{\eta}(k) = \frac{a_x a_y a_z}{\pi^2(1+4k_x^2a_x^2+4k_y^2a_y^2+4k_z^2a_z^2)}$ is adapted for the lamellar crystallites. In this case, the spatial scales a_x, a_z and a_y are redefined as $a_x = a_z = L$ and $a_y = d$.

Following the approach stated in Eq. (4.9) in chapter 4, the spatial correlation function $\tilde{\eta}_{w_i}^{LT}(\pi-\Theta)$ for the microstructure shown in Fig. 7.3a is written as

$$\begin{aligned} \tilde{\eta}_{w_i}^{LT}(\pi-\Theta) &= \frac{a_x a_y a_z}{\pi^2(1+4k_x^2a_x^2+4k_y^2a_y^2+4k_z^2a_z^2)} \\ &= \frac{L^2 d}{\pi^2\left[1+(k_L^2+k_T^2-2k_Lk_T\cos(\pi-\Theta))\langle l_i^2\rangle\right]^2}, \end{aligned} \tag{7.8}$$

where the quantities $\langle l_i\rangle, (i=1,2)$ define the average 'interaction lengths', which are the effective scale lengths in the direction of wave propagation as shown in Figs 7.3b and 7.3c, respectively. Here, the duplex crystallites within grains are assumed to

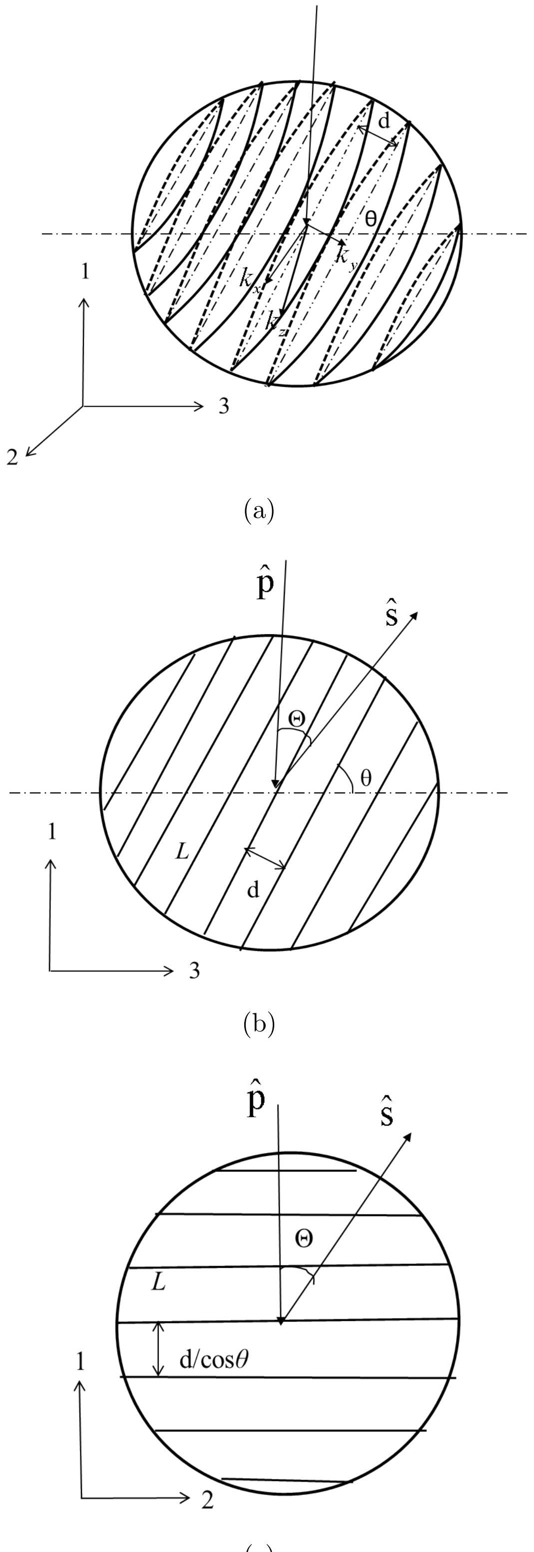

(a)

(b)

(c)

Figure 7.3: Schematics of lamellar duplex microstructure within an individual grain (pearlite phase), (a) a 3D model, (b) the cross section feature sliced in the 1-3 plane, (c) the cross section feature sliced in the 1-2 plane.

be oriented randomly such that the angle θ shown in Fig. 7.3b varies with equal probability between 0 and π. The squares of the effective interaction lengths are then averaged [50] giving

$$\begin{aligned}
\langle l_1^2 \rangle &= \frac{1}{\pi}\int_0^{\pi} (\sin^2\theta L^2 + \cos^2\theta d^2) d\theta \\
&= (L^2 + d^2)/2, \\
\langle l_2^2 \rangle &= \frac{1}{\pi}\int_0^{\pi} \frac{d^2}{\cos^2\theta} d\theta \\
&= \frac{1}{\pi}(\int_0^{\theta_0} \frac{d^2}{\cos^2\theta} d\theta + \int_{\theta_0}^{\pi-\theta_0} \frac{d^2}{\cos^2\theta} d\theta + \int_{\pi-\theta_0}^{\pi} \frac{d^2}{\cos^2\theta} d\theta) \\
&= \frac{1}{\pi}\left[L^2(\pi - 2\theta_0) + 2d^2\frac{\sin\theta_0}{\cos\theta_0} \right] \\
&= \frac{1}{\pi}\left[L^2(\pi - 2\arccos(d/L)) + 2d\sqrt{L^2 - d^2} \right], \qquad (7.9)
\end{aligned}$$

where $\theta_0 = \arccos d/L$, when the angle θ ranges from θ_0 to $\pi - \theta_0$, $d/\cos\theta \approx L$.

Substituting Eq. (7.9) into Eq. (7.8) the average spatial correlation function $\tilde{\eta}_{w_i}^{LT}$ for lamellar microstructure features shown in Figs. 7.3b and 7.3c can be written as

$$\begin{aligned}
\tilde{\eta}_{w_1}^{LT}(\pi - \Theta) &= \frac{L^2 d}{\pi^2 \left[1 + (k_L^2 + k_T^2 - 2k_L k_T \cos(\pi - \Theta))(L^2 + d^2)/2\right]^2}, \\
\tilde{\eta}_{w_2}^{LT}(\pi - \Theta)& \\
= \frac{L^2 d}{\pi^2 \left\{1 + (k_L^2 + k_T^2 - 2k_L k_T \cos(\pi - \Theta)) \left[L^2(\pi - 2\arccos(d/L)) + 2d\sqrt{L^2 - d^2}\right]/\pi\right\}^2}&. \qquad (7.10)
\end{aligned}$$

By substituting Eqs. (7.6) and (7.10) into the Eq. (7.7), the total backscatter coefficients for the two L-T cases shown in Figs. 7.3b and 7.3c can be written as

$$\begin{aligned}
K_1^{LT} &= \frac{(1-M)L^3[\Xi^{\cdots\hat{\mathbf{p}}_0\hat{\mathbf{p}}_0\hat{\mathbf{s}}_0\hat{\mathbf{s}}_\perp}_{\cdots\hat{\mathbf{p}}_0\hat{\mathbf{p}}_0\hat{\mathbf{s}}_0\hat{\mathbf{s}}_\perp}(\pi-\Theta)]_r}{\pi^2[1+k_T^2L^2+k_L^2L^2-2k_Lk_TL^2\cos(\pi-\Theta)]^2} \\
&+ \frac{ML^2d[\Xi^{\cdots\hat{\mathbf{p}}_0\hat{\mathbf{p}}_0\hat{\mathbf{s}}_0\hat{\mathbf{s}}_\perp}_{\cdots\hat{\mathbf{p}}_0\hat{\mathbf{p}}_0\hat{\mathbf{s}}_0\hat{\mathbf{s}}_\perp}(\pi-\Theta)]_{w_1}}{\pi^2\left[1+(k_L^2+k_T^2-2k_Lk_T\cos(\pi-\Theta))(L^2+d^2)/2\right]^2}, \\
K_2^{LT} &= \frac{(1-M)L^3[\Xi^{\cdots\hat{\mathbf{p}}_0\hat{\mathbf{p}}_0\hat{\mathbf{s}}_0\hat{\mathbf{s}}_\perp}_{\cdots\hat{\mathbf{p}}_0\hat{\mathbf{p}}_0\hat{\mathbf{s}}_0\hat{\mathbf{s}}_\perp}(\pi-\Theta)]_r}{\pi^2[1+k_T^2L^2+k_L^2L^2-2k_Lk_TL^2\cos(\pi-\Theta)]^2} \\
&+ \frac{ML^2d[\Xi^{\cdots\hat{\mathbf{p}}_0\hat{\mathbf{p}}_0\hat{\mathbf{s}}_0\hat{\mathbf{s}}_\perp}_{\cdots\hat{\mathbf{p}}_0\hat{\mathbf{p}}_0\hat{\mathbf{s}}_0\hat{\mathbf{s}}_\perp}(\pi-\Theta)]_{w_2}}{\pi^2\left\{1+(k_L^2+k_T^2-2k_Lk_T\cos(\pi-\Theta))\left[L^2(\pi-2\arccos(d/L))+2d\sqrt{L^2-d^2}\right]/\pi\right\}^2}.
\end{aligned} \tag{7.11}$$

Substituting the backscatter coefficient given in Eq. (7.2) to Eqs. (7.11), the mode-converted SSR model that includes the dependence of ultrasonic scattering on the pearlite, can be expressed as

$$\begin{aligned}
\Phi_i^{LT}(t) &= \Phi_0^{LT}K_i^{LT}\int_0^\infty dz\int_{-\infty}^\infty dx\exp(-\frac{t^2}{\sigma_S^2})\frac{w_{0R}^2}{w(z)w_1(Z)\sqrt{w^2(z)+w_2^2(Z)}} \\
&\times\exp\left[-\frac{2x^2}{w^2(z)}-\frac{2X^2}{w_1^2(z)}-\frac{2z^2}{\sigma_S^2c_L^2}-\frac{2Z^2}{\sigma_S^2c_T^2}+\frac{4Zt}{\sigma_S^2c_T}\right] \\
&\times\exp\left[\frac{1}{\sigma_S^2}\left(\frac{Z}{c_T}-\frac{z}{c_L}\right)^2-\frac{2t}{\sigma_S^2}(\frac{Z}{c_T}-\frac{z}{c_L})-2\alpha_Lz-2\alpha_TZ\right].
\end{aligned} \tag{7.12}$$

When the lamellar spacing d approaches L, (i.e, the lamellar duplex microstructure is absent), Eq. (7.12) reduces to the theoretical SSR model for a single phase given in Eq. (7.2). Note that the inner product on the eighth-rank covariance tensor for lamellar duplex microstructure within a grain $[\Xi^{\cdots\hat{\mathbf{p}}_0\hat{\mathbf{p}}_0\hat{\mathbf{s}}_0\hat{\mathbf{s}}_\perp}_{\cdots\hat{\mathbf{p}}_0\hat{\mathbf{p}}_0\hat{\mathbf{s}}_0\hat{\mathbf{s}}_\perp}(\pi-\Theta)]_{w_i}$ is assumed equal to the same quantity when the lamellae are absent, $[\Xi^{\cdots\hat{\mathbf{p}}_0\hat{\mathbf{p}}_0\hat{\mathbf{s}}_0\hat{\mathbf{s}}_\perp}_{\cdots\hat{\mathbf{p}}_0\hat{\mathbf{p}}_0\hat{\mathbf{s}}_0\hat{\mathbf{s}}_\perp}(\pi-\Theta)]_r$. Several trends in the behavior of this model can be observed.

7.2 Model Results

In this section, trends predicted by the model with respect to the microstructural parameters are examined. Several parameters given in Eq. (7.12) required for the model must first be specified (including the pulse duration and the single-crystal elastic constants of steel). Table 4.1 shows some of the values used in the results that follow. Theoretical values of wave speed and attenuation in water were selected from [70] and the attenuation in the pearlitic steel is estimated as discussed in chapter 6 .

Fig. 7.4 shows the dependence of the spatial variance amplitudes on lamellar spacing d for both the mode-converted L-T scattering mode given by Eq. (7.12) and the L-L mode discussed in chapter 4. It can be seen that the variance amplitudes

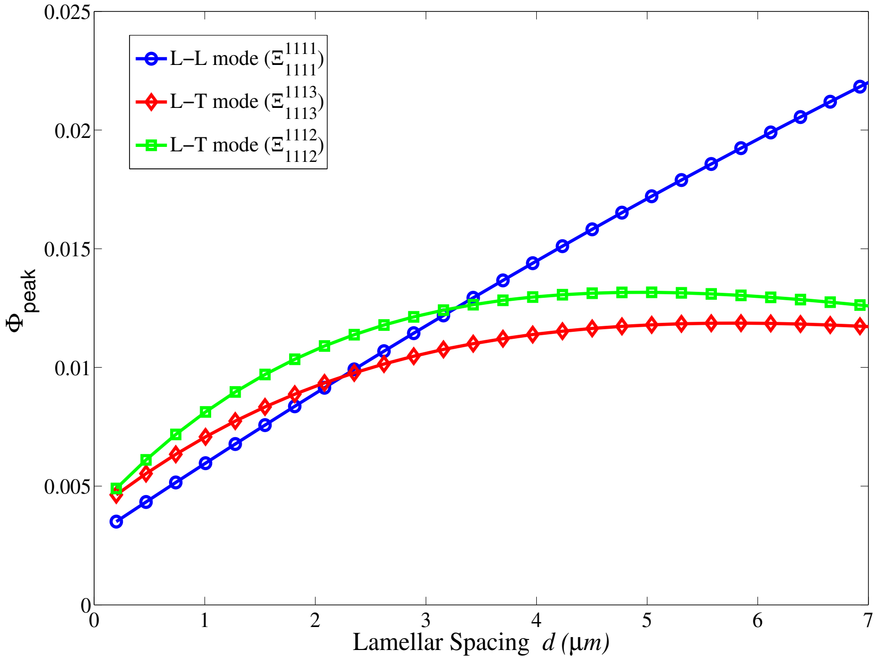

Figure 7.4: The variance amplitudes versus the lamellar spacing d, the angle $\theta_0 = \arccos d/L$ shown in Eq. (7.9) varies with increasing d, while L=24 μm, M=0.9.

estimated using the L-T modes are higher than that calculated using the L-L mode with respect to the small lamellar spacing, while the variance amplitudes using the L-L mode are much higher than that using the L-T modes when the lamellar spacing is large.

Fig. 7.5 demonstrates the dependence of the attenuation coefficients on lamellar spacing which was detailed in chapter 6. It can be seen that the difference between the α_L and α_T is significant with respect to large lamellar spacing compared with the small lamellar spacing. The much higher transverse attenuation decreases the L-T variance amplitudes more significantly compared with the L-L variance amplitudes when the lamellar spacing is large.

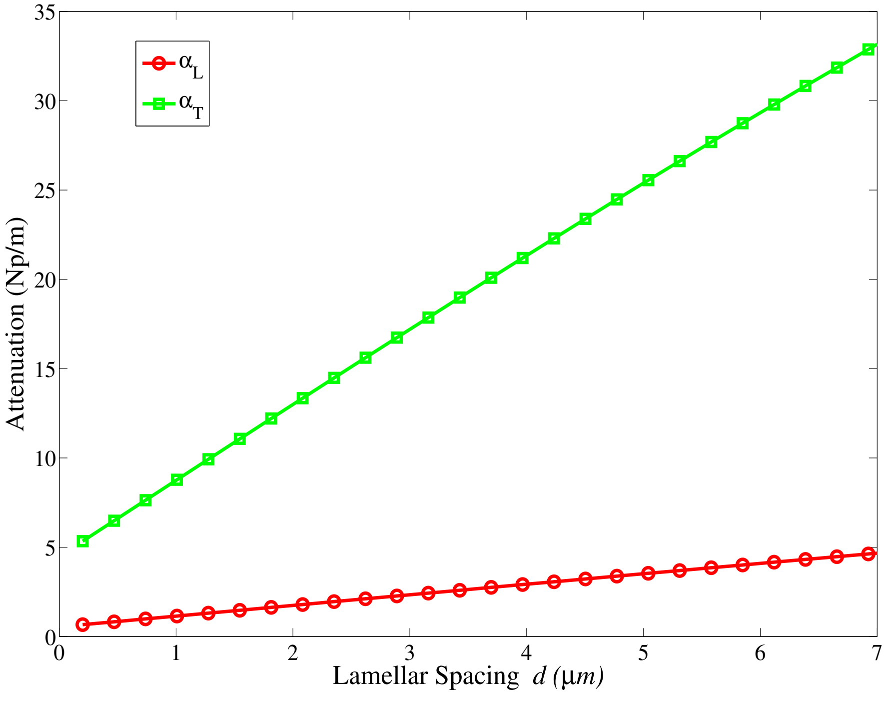

Figure 7.5: The attenuation coefficients versus the lamellar spacing d (L=24 μm, M=0.9).

By comparing the variance amplitudes calculated using the L-T model for the duplex features shown in Figs. 7.4b and 7.4c, it can be observed that the variance amplitudes calculated in the 1-2 and 1-3 planes are very similar for small lamellar spacing, but the two curves split gradually as the lamellar spacing increases. Fig. 7.6 shows the backscatter coefficients calculated given by Eq. (7.11) while increasing the lamellar spacing d. The separation between the two curves is observed as the lamellar spacing increases, an outcome that could explain the splitting of the variance amplitudes shown in Fig. 7.4. The slopes of the L-T variance curves shown in Fig. 7.4 decrease with increasing the lamellar spacing, a result that is attributed to the increasing shear attenuation demonstrated in Fig. 7.5. In the next section, results from

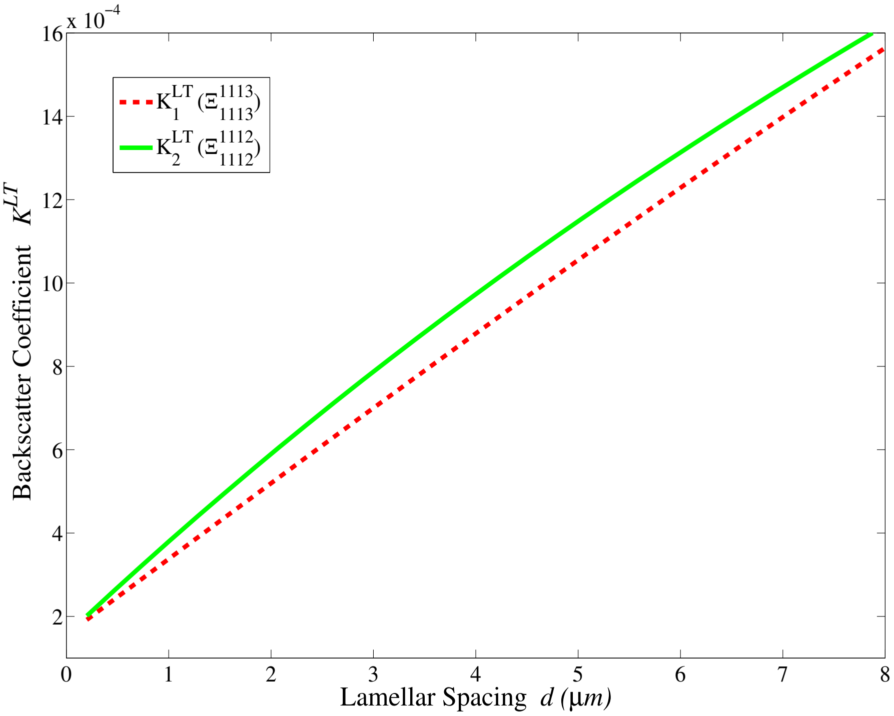

Figure 7.6: The backscatter coefficient including lamellar microstructure within grains given in Eq. (7.11) versus the lamellar spacing d (L=24 μm, M=0.9).

experiments are presented from the cross section of a quenched wheel sample using both the L-L SSR mode and L-T SSR modes measured in two directions. Then the mode-converted (L-T) SSR model given in Eq. (7.12) is used to fit the experimental variance curves, from which the lamellar spacing d and the correlation length L can be found.

7.3 Experiments

A pitch-catch configuration was used for the diffuse mode-converted (L-T) ultrasonic backscatter experiment. Ultrasonic longitudinal pulse waves, generated by a DPR 300 pulser/receiver (*Imaginant and JSR Ultrasonics*, Pittsford, NY), were transmitted from a normally incident source transducer into a test sample and scattered shear waves were received by a receiver transducer. The experimental spatial variance for a collection of ultrasonic backscattered signals captured from various positions was defined in Eq. (4.14). Experiments were performed in a water immersion tank using two 10 MHz focused transducers (V327 9.53 mm diameter; 50.4 mm focal length; *Olympus NDT*, Newton, MA) focused 7.5 mm in a quenched railroad wheel steel sample (annealed to remove the residual stress) [72]. The scan speed was 3.0 mm/s and scan step sizes were 0.25 mm (in the radial direction), 0.50 mm (in the axial direction). A high gain (65 dB) was used to obtain strong backscatter signals (A/D sampling rate = 2 GHz). Fig. 7.7 shows the experimental setup for the mode-converted diffuse ultrasonic backscatter measurement in a pitch-catch configuration. The normally incident transducer is the source transducer, and the oblique one acts as a receiver. Both transducers focus at the same depth. The cross section of the wheel sample shown in Fig. 7.8 was scanned using both the L-L SSR mode and the L-T SSR modes measured in two planes (parallel and perpendicular to the tread surface),

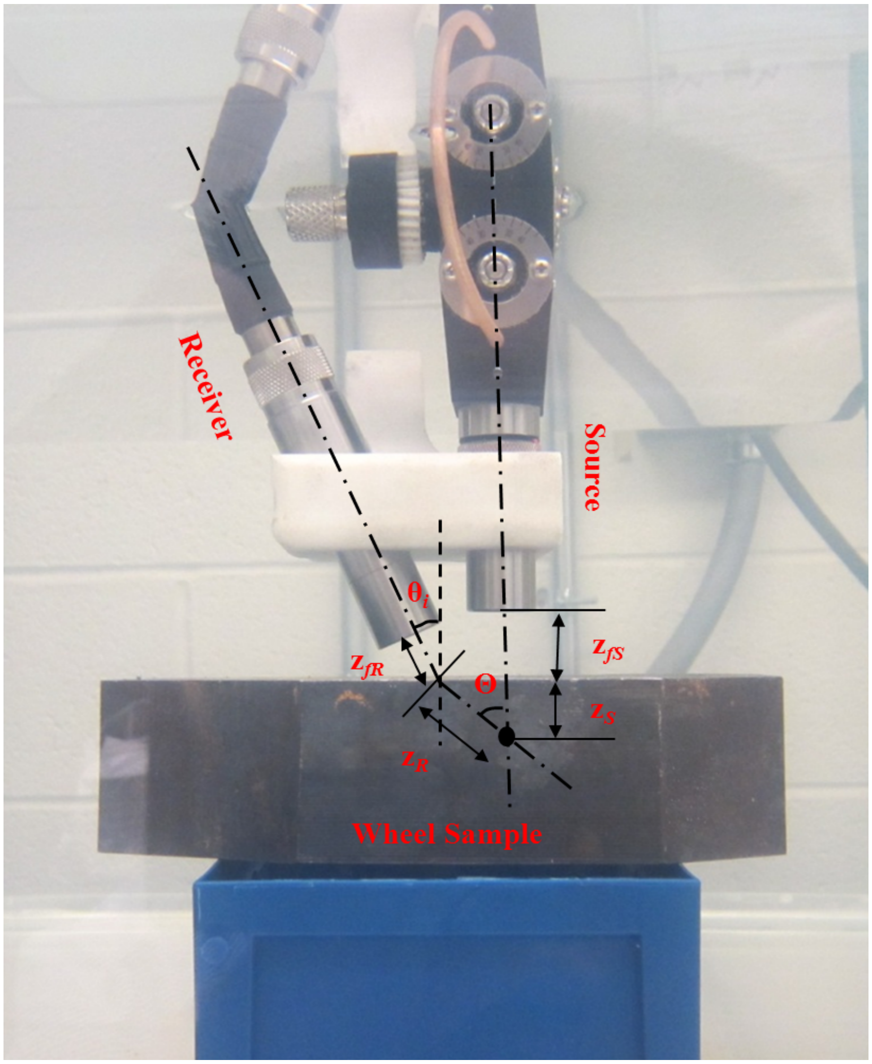

Figure 7.7: The experimental setup for the mode-converted diffuse ultrasonic backscatter in a pitch-catch configuration.

respectively.

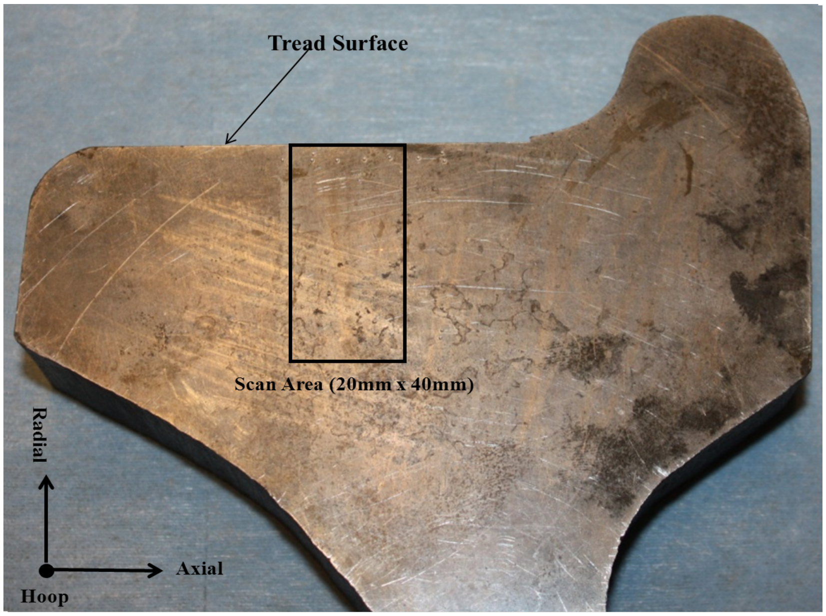

Figure 7.8: The cross section image of a wheel sample annealed to remove the residual stress.

The scan region shown in Fig. 7.8 was divided into 14 subregions (20 mm × 3 mm) from the tread surface to deeper locations to calculate the spatial variance curves according to Eq. (4.14), respectively. Each area contained about 480 waveforms. Figs. 7.9a and 7.9b demonstrate the spatial variance curves of the collected backscatter signals for the subregions close to the tread surface and at deeper locations (around 30 mm deep from the tread), respectively. It can be observed that the L-T variance peaks measured in two directions are very similar and much higher than the L-L variance peak at the subregion near the tread surface, while the L-L variance peak is higher than the L-T variance peaks at the deeper location, a result which may be attributed to the higher transverse attenuation α_T compared with the longitudinal attenuation α_L. The L-T variance peak measured in the hoop-radial plane (perpendicular to the tread surface) is higher than that measured in the hoop-axial plane (parallel to the tread surface), a result attributed to the difference of the effective interaction lengths given by Eq. (7.9).

The experimental spatial variance curves shown in Figs. 7.9a and 7.9b are fit with the L-T model given by Eq. (7.12) and the L-L model described in chapter 4 to determine the variance amplitudes for each subregion. Fig. 7.10 demonstrates this distribution from the tread surface to deeper locations. It can be seen that the variance amplitudes measured in both the L-T and L-L modes show an increasing trend with depth from the tread surface. The mode-converted L-T ultrasonic backscatter is much higher than the L-L ultrasonic backscatter with respect to the small lamellar spacing close to the tread surface, and the difference between the L-T and L-L ultrasonic scattering decreases with depth from the tread surface. The L-L ultrasonic scattering exceeds the L-T ultrasonic scattering and the difference becomes larger and larger when it is over 25 mm from the tread surface. By comparing the L-T variance amplitudes measured in two planes, it can be seen that the two curves split up from the locations close to the tread surface. The difference between two L-T variance amplitudes measured in the hoop-radial and hoop-axial planes increases progressively with depth, a result that is attributed to the increasing difference of the effective interaction lengths. The experimental results show the same trend as the theoretical prediction shown in Fig 7.4. By comparing Fig 7.4 and 7.10, it can be seen that the difference between the two measured L-T variance amplitudes at deeper location is much larger than the theoretical prediction. Clearly the orientations of lamellae differ from the model. More studies are required to verify the reason.

The mode-converted (L-T) variance amplitudes measured in the two directions shown in Fig. 7.10 can be used to quantify the microstructural parameters of correlation length L and lamellar spacing d with the L-T model given in Eq. (7.12). When the L-T experiment measured in the hoop-axial plane was switched to the hoop-radial

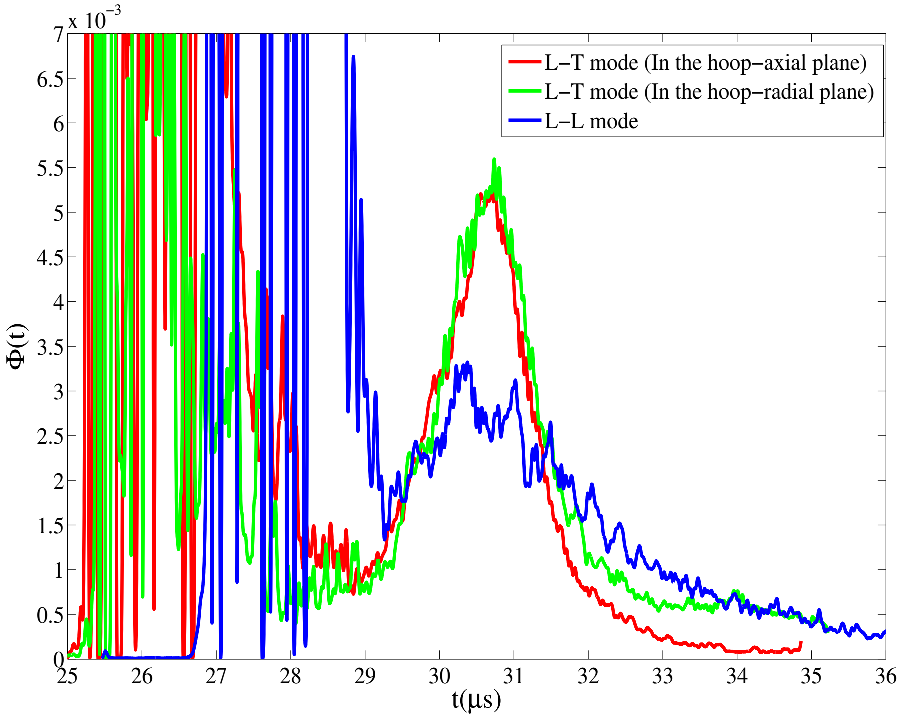

(a)

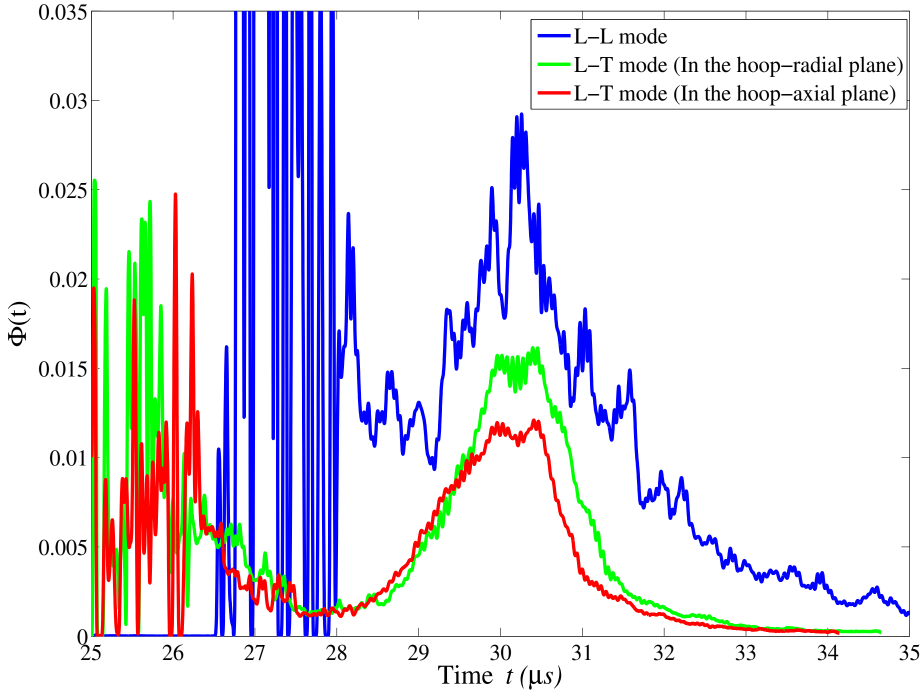

(b)

Figure 7.9: Experimental spatial variance curves of ultrasonic backscattered signals, (a) near the tread surface, (b) 30 mm from the tread.

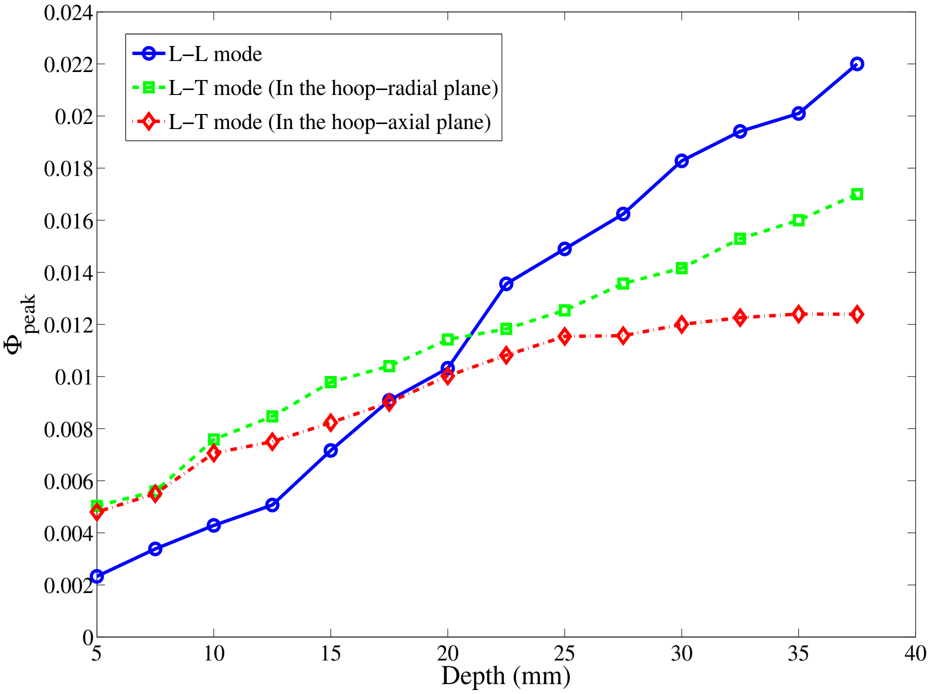

Figure 7.10: Distribution of variance amplitudes from the tread surface to deeper locations.

plane, only the backscatter coefficient K_i^{LT} in terms of the lamellar spacing d and the correlation length L given by Eqs. (7.11) is changed. The other constants used in the calculation are shown in Table 4.1, and the wave velocity and attenuation for water were measured as c_f=1486 m/s; α_f=.025 Np/cm. The wave speed for the steel sample was measured c_L=5973 m/s. As discussed in chapter 6, the attenuation exhibits a strong dependence on lamellar spacing d. The longitudinal attenuation α_L in the wheel sample was measured with depth from the tread surface as shown in Fig. 6.7. The transverse attenuation α_T was estimated based on the developed attenuation model which was discussed in chapter 6. The transducers were first calibrated to determine some important parameters such as $V_{max}^{\xi}, (\xi = S, R)$ before testing as stated in chapter 4.

The maximum of the experimental spatial variance $[\Phi_i^{LT}(t)]^{Exp}_{max}$ was used with Eq. (7.12) and Eqs. (7.13) to estimate the lamellar spacing d and the correlation length L simultaneously. The quantities d and L appear in Eqs. (7.13) in two terms, such that the experimental variance measured with L-T mode in two directions can be equated to the model and rearranged into a set of equations governing d and L. Following this procedure, it can be shown that d and L satisfy the equations

$$\begin{aligned}
&\frac{(1-M)L^3}{\pi^2[1+k_T^2L^2+k_L^2L^2-2k_Lk_TL^2\cos(\pi-\Theta)]^2}\\
&+\frac{ML^2d}{\pi^2\left[1+(k_L^2+k_T^2-2k_Lk_T\cos(\pi-\Theta))(L^2+d^2)/2\right]^2}=R_1,\\
&\frac{(1-M)L^3}{\pi^2[1+k_T^2L^2+k_L^2L^2-2k_Lk_TL^2\cos(\pi-\Theta)]^2}\\
&+\frac{ML^2d}{\pi^2\left\{1+(k_L^2+k_T^2-2k_Lk_T\cos(\pi-\Theta))\left[L^2(\pi-2\arccos(d/L))+2d\sqrt{L^2-d^2}\right]/\pi\right\}^2}=R_2
\end{aligned} \tag{7.13}$$

where $R_i = \frac{[\Phi_i^{LT}(t)]^{Exp}_{max}}{[\Phi_i^{LT}(t)]_{max}/\tilde{\eta}_i^{total}}$, and $[\Phi_i^{LT}(t)]^{Exp}_{max}$ represents the two obtained variance peaks measured by the L-T experiments shown in Fig. 7.10. $i = 1$ represents the L-T experiment measured in the hoop-axial plane, while $i = 2$ indicates the L-T measurement in the hoop-radial plane. $\tilde{\eta}_i^{total} = (1-M)\tilde{\eta}_r^{LT}(\pi-\Theta) + M\tilde{\eta}_{w_i}^{LT}(\pi-\Theta)$. The lamellar spacing d and the correlation length L can be obtained by solving an equation set given by Eqs. (7.13) while fixing $M = 0.9$. Experience with the solution of Eqs. (7.13) when applied to experimental data shows that only one root is physically meaningful. Fig. 7.11 shows two curves of lamellar spacing d versus the correlation length L based on Eqs. (7.13) using the variance amplitudes at a scan subregion measured in two directions. The intersection point of the two $d-L$ curves

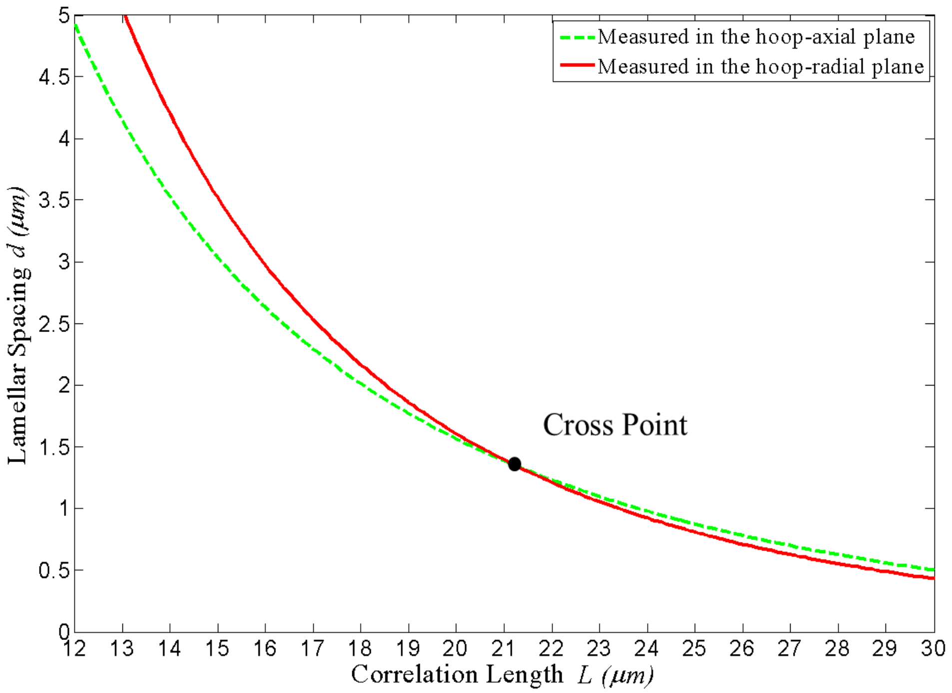

Figure 7.11: The calculated lamellar spacing d versus the correlation length L using the variance amplitudes measured in two directions.

shown in Fig. 7.11 corresponds with the final solution of the lamellar spacing d and the correlation length L. Thus, the lamellar spacing d and the correlation length L can be obtained simultaneously with the L-T model given by Eq. (7.12) and the L-T variance peaks measured in two directions.

Fig. 7.12 shows the distribution of the calculated lamellar spacing d and the correlation length L, with depth from the tread surface. The red line represents the estimated lamellar spacing, while the green line indicates the calculated correlation length. It can be seen that the calculated lamellar spacing d increases from 0.3 μm to around 7.0 μm with depth from the tread surface, a result that matches well with the optical observations shown in Figs. 4.10a and 4.10b. The estimated correlation length L varies from around 20 μm to 30 μm. The average correlation length in the whole wheel sample is about 23.2 mm.

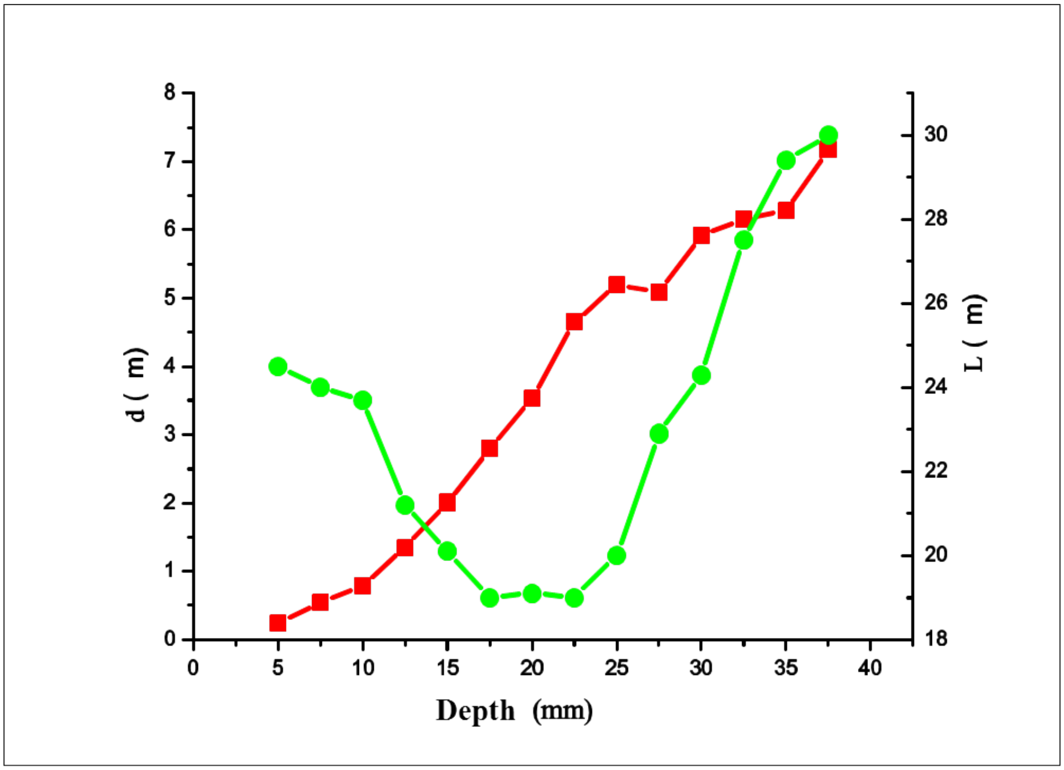

Figure 7.12: Distribution of the calculated lamellar spacing *d* and the correlation length *L* with depth from the tread surface to deeper locations (M=0.9).

7.4 Summary

A mode-converted (longitudinal-to-transverse, L-T) SSR model that accounts for pearlite microstructure within grains has been developed based on the previous L-T SSR model. Diffuse ultrasonic backscatter experiments were conducted in a water tank using two 10 MHz transducers focused 7.5 mm deep in a quenched railroad wheel sample with both the L-L and L-T modes. The experimental results show that the variance amplitudes measured with the L-L mode are smaller than those measured with the L-T mode near the tread surface and two L-T variance amplitude measured in the hoop-radial and hoop-axial planes are very similar. At deeper locations, the L-L variance amplitudes are much larger than the L-T variance amplitudes, a result which may be attributed to the much higher transverse attenuation in comparison with the longitudinal attenuation. The variance amplitudes measured in the hoop-radial plane are larger than those measured in the hoop-axial plane, which might result from different interaction lengths within these two planes due to the large lamellar spacing as well as the specific orientation due to the non-uniform cooling rate.

In addition, the difference of variance amplitude increases progressively from the tread surface to deeper locations due to the increasing lamellar spacing. The experimental results demonstrate the same trend as the theoretical predictions. The distributions of lamellar spacing and the correlation length with depth from the tread surface were also quantified with the newly developed L-T SSR model. The calculated lamellar spacing within grains ranged from 0.3-7.0 μm. The correlation length varies from 20-30 μm, the average value is around 23.2 μm. The mode-converted ultrasonic backscatter exhibits very strong sensitivity such that minor microstructural differences can be distinguished in different directions. Thus, it seems that this approach can be applicable for examining the grain elongation, orientation of duplex microstructure and texture that result from manufacturing.

Chapter 8

Dependence of Ultrasonic Backscatter on Stress

The theory of acoustoelasticity refers to the relationship between wave propagation speed in a deformable medium and the state of stress present. This relationship considers the influence of finite strains or wave displacements superimposed on a deformed medium. Usually, linear-elastic approximations are not adequate to describe material responses in applications experiencing sufficiently large strains. In such cases, the acoustoelastic formalism considers nonlinear strain energy terms up to the third-order to describe the effect properly [75], [76]. The higher-order strain energy terms introduce the use of third-order elastic constants into the constitutive equations. These theoretical developments led to the application of acoustoelasticity as a method of extracting higher-order material constants in a variety of materials [77], [78].

Other continuing developments have been made using the acoustoelastic effect for stress measurement [79], [80], [81]. Many researchers have applied wavespeed measurements of ultrasonic propagation modes to extract residual stress information in welded joints using multiple elastic waves, such as the longitudinal critically refracted

(Lcr) elastic wave [82], [83], [84], and the leaky Lamb wave [85], [86]. Recently, Turner and Ghoshal [39] presented a theoretical basis to extract stress information from polycrystalline microstructures by considering second-order grain statistics through the covariance of elastic moduli fluctuations, an eighth-rank tensor. The covariance tensor had been included in previously developed ultrasonic grain scattering models and is proportional to the attenuation and backscatter coefficient [24], [30] - [33], [46]. However, these models did not consider any stress dependency. Kube et al. [40] confirmed the stress dependence of the covariance tensor by investigating the change of the spatial variance amplitude using an applied uniaxial load on a 1018 steel block.

In this chapter, the influence of stress on ultrasonic scattering in a steel sample is investigated by comparing the spatial variance amplitudes of the collected ultrasonic backscatter signals under uniaxial load with and without stress. Normally incident ultrasound is utilized to examine the dependence of ultrasonic scattering on stress. Based on the experimental observations, the ultrasonic backscatter technique is applied for measuring residual stress introduced by water quenching in steel samples. The change of the spatial variance amplitudes after removing the residual stress via annealing is calculated, a quantity that can be transferred to the residual stress value according to the developed stress-dependent backscatter model. The diffuse backscatter technique exhibits strong sensitivity to the stress (including applied stress and residual stress), an outcome that may be applicable for stress measurement in the future.

8.1 Stress-dependent Ultrasonic Backscatter Coefficient

Ultrasonic scattering is used to describe the multitude of reflections from grain boundaries comprising a polycrystalline material. Scattering models are used to quantify the strength of the scattering emanating from the assumed randomly oriented grains. The strength of the scattering is dependent on the degree of crystalline anisotropy inherent within the grains. In chapter 3, Eq. (3.43) gave a time-dependent spatial variance model of ultrasonic backscatter measurement with respect to an assumption of a singly-scattered response (SSR) to microstructural properties. It may be written as

$$\Phi_{SSR} = R(\mathrm{V})\tilde{\eta}(L)\Xi(\mathbf{T})\exp\left(-\frac{t^2}{\sigma^2}\right)I_0(t), \tag{8.1}$$

where $R(\mathrm{V})$ is the amplitude coefficient which is dependent on the excitation transducer voltage and can be determined through a calibration process. $\tilde{\eta}(L)$ is the spatial Fourier transform of two-point correlation function with a correlation length L. $\Xi(\mathbf{T})$ is called the covariance tensor which is a function of elastic constants of material and stress tensor, $\mathbf{T}$. The time-dependent term $\exp\left(-\frac{t^2}{\sigma^2}\right)$ describes the input Gaussian beam, and σ denotes the pulse width. The term $I_0(t)$ is an integral that accounts for changes in the focal profile as a function of material depth. In contrast to the change of covariance tensor Ξ, the change in the attenuation and wavespeed due to the stress is neglected. The covariance of the effective (stress-dependent) elastic moduli is defined as [39].

$$\Xi_{ijkl}^{\alpha\beta\gamma\delta} = \langle G_{ijkl}G_{\alpha\beta\gamma\delta}\rangle - \langle G_{ijkl}\rangle\langle G_{\alpha\beta\gamma\delta}\rangle, \tag{8.2}$$

where G_{ijkl} is the load-dependent effective elastic moduli within the medium. For a single crystal, it can be written in terms of the second-order elastic moduli C_{ijkl} and the third-order elastic moduli C_{ijklmn}, as $G_{ijkl} = C_{ijkl} + (\delta_{jl}\delta_{kP}\delta_{iQ} + 2C_{ijkr}S_{lrPQ} + C_{ijklmn}S_{mnPQ})T_{PQ}$, where $S_{ijkl} = C^{-1}_{ijkl}$ is the second-order compliance tensor, and T_{PQ} is the stress tensor. The second-order elastic moduli can be written as [39]

$$C_{ijkl} = C^{I}_{ijkl} + \nu\delta_{ijkl} = C^{I}_{ijkl} + \nu\sum_{n=1}^{3} a_{in}a_{jn}a_{kn}a_{ln}, \tag{8.3}$$

where $\nu = c_{11} - c_{12} - 2c_{44}$ is the anisotropy coefficient for a material with cubic crystal symmetry, C^{I}_{ijkl} is the isotropic fourth-rank tensor, and a_{ij} is the rotation matrix between crystal and laboratory axes. The third-order elastic moduli can be expressed as [36]

$$C_{ijklmn} = C^{I}_{ijklmn} + d_1E^{1}_{ijklmn} + d_2E^{2}_{ijklmn} + d_3E^{3}_{ijklmn}, \tag{8.4}$$

where d_1, d_2 and d_3 are three anisotropy constants defined by the independent third-order elastic constants. The base tensors $\mathbf{E}^{i}, (i = 1, 2, 3)$ are written in terms of the components of the rotation matrix. Equation (8.2) can be expanded and written in condensed form in terms of the magnitude of an applied uniaxial stress as

$$\Xi(T) = K_0 + K_1T + K_2T^2, \tag{8.5}$$

where K_0, K_1 and K_2 are load independent constants related to directionality of the applied stress as well as the components $ijkl$ and $\alpha\beta\gamma\delta$. The covariance tensor in Eq. (8.5) determines the magnitude of the backscatter coefficient and makes a connection between the stress $\mathbf{T}$ and the strength of ultrasonic scattering.

To illustrate the stress influence on ultrasonic scattering, only the simplest case is considered of a stress-free polycrystalline sample (with cubic crystal symmetry) subject to an applied uniaxial load in the 1-direction. The longitudinal-to-longitudinal

(L-L) mode using normal incidence ultrasound is used to examine the impact of stress on the scattering. The covariance tensors Ξ_{1111}^{1111}, and Ξ_{3333}^{3333} correspond with the L-L experiments for which the propagation vector $\hat{\mathbf{p}}$ is parallel and perpendicular to the loading axis, respectively. Table 8.1 shows the single crystal second- and third-order elastic constants for pure iron [31]. Table 8.2 lists the numerical values of K_0, K_1 and K_2 with respect to covariance tensors Ξ_{1111}^{1111}, and Ξ_{3333}^{3333} for pure iron given by Eq. (8.5) [39]. Several observations can be made from the results [39]. First, the positive value of K_2 will increase the scattering under either compressive or tensile stress. Second, the negative values of K_1 will increase the backscatter amplitude under compressive stress for the L-L Ξ_{1111}^{1111} mode, while for the L-L Ξ_{3333}^{3333} mode, the positive value will decrease the backscatter amplitude under a compressive stress. Lastly, because the ratio of K_1 to K_2 is so large the scattering is expected to be nearly linear under low load (<500 MPa).

Table 8.1: Single crystal second - and third-order elastic constants (GPa) for pure iron.

Material	C_{11}	C_{12}	C_{44}	C_{111}	C_{112}	C_{123}	C_{144}	C_{166}	C_{456}
Iron	229.3	134.1	116.7	-2720	-608	-578	-836	-530	-720

Table 8.2: Theoretical backscatter coefficients of pure iron [39].

Mode	K_0(GPa^2)	K_1(GPa)	K_2
Ξ_{1111}^{1111}	582.1	-341.4	80.76
Ξ_{3333}^{3333}	582.1	159.1	27.86

8.2 Experiments

8.2.1 Uniaxial Stress on a 1018 Steel Block

The backscatter experiments were performed in a water immersion tank using a 10 MHz transducer (V327-SU; 9.53 mm diameter; 50 mm focal depth; *Olympus NDT*, Newton, MA) focused 9.0 mm in a block (3 inch × 4 inch × 12 inch) of annealed 1018 steel. Fig. 8.1 shows the experimental setup of the backscatter measurement under a uniaxial load with the L-L Ξ_{3333}^{3333} mode. The ultrasonic propagation direction was normal to the steel block but perpendicular to the loading direction. The scattered signals were obtained from the waveforms by observing the energy between the front and back surface reflections. The spatial variance was determined from the collection of backscatter signals obtained at 400 different locations (within a 60 mm × 60 mm area) while keeping a fixed distance between the transducer and the material.

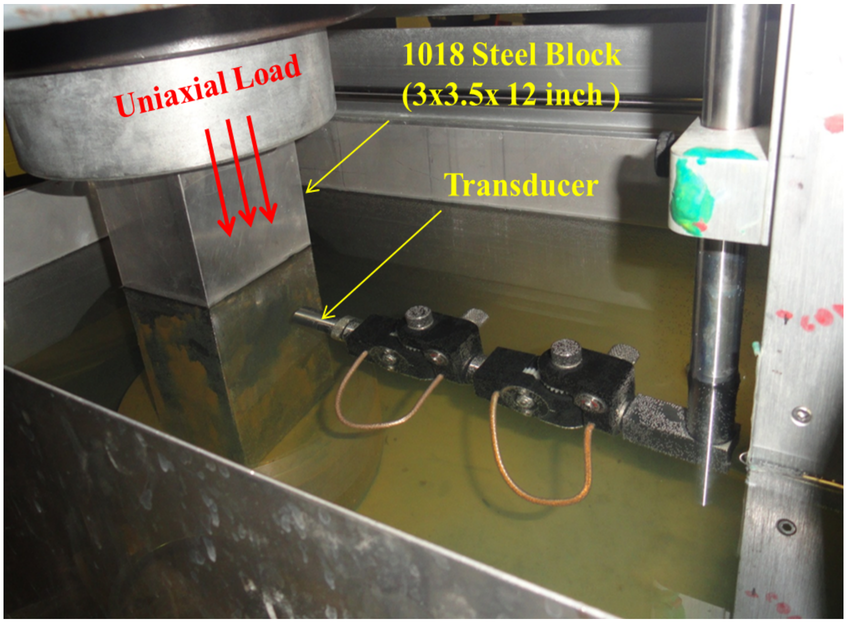

Figure 8.1: Experimental setup for the backscatter measurement under a uniaxial load.

To investigate the dependence of ultrasonic backscatter signals on applied load, the sample was loaded uniaxially at a constant loading rate of 178 kN/min to a maximum load of 1780 kN. At each increment of 222.4 kN for the loading step, the load was held constant. A 60 mm × 60 mm area on the side surface of the loaded steel sample was scanned at a constant speed during each holding period. The scan was performed with a step size of 3 mm to ensure the independence of individual measurements. Then the spatial variance of the waveforms was calculated using a collection of 400 waveforms. The loading process was repeated over a set of three loading trials performed on separate days to observe the experimental repeatability. Each spatial variance response was fit using Eq. (8.1) to extract the spatial variance peak as a function of stress. Fig. 8.2 shows the dependence of the spatial variance peak on applied load for the three trials. The experimental results show a decreasing

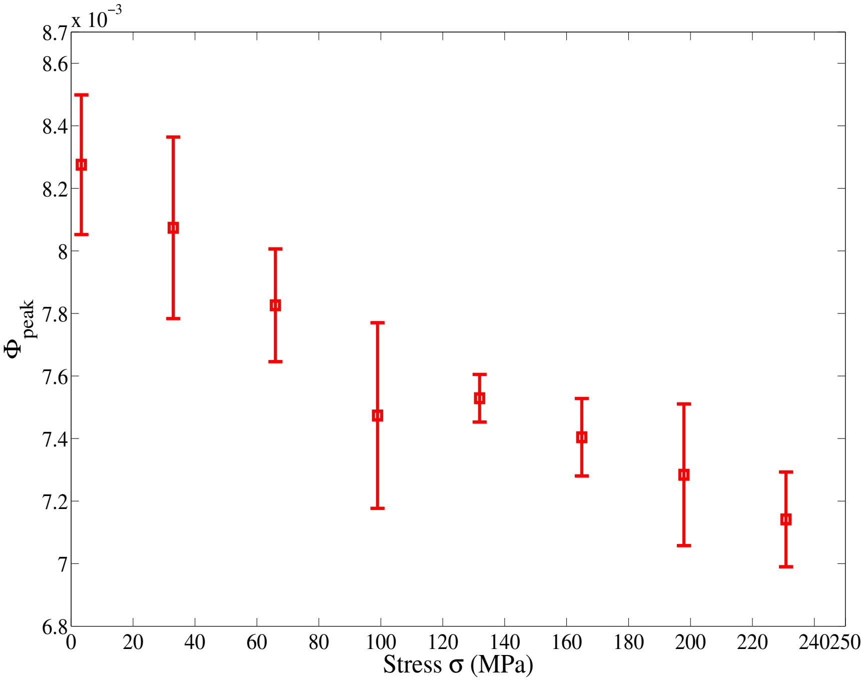

Figure 8.2: The measured spatial variance peaks versus applied loads.

trend with increasing compressive stress as predicted from the theory.

This backscatter technique has many applications in the area of nondestructive stress measurement techniques. Compared with previous ultrasonic stress measurement techniques based on wave propagation speed, this technique is much more sensitive to applied load, the results shown in Fig. 8.2 change by 12.6 %, while the waves speed perpendicular to a compression load in rail steel was found to change by 0.32 % over a similar loading of about -260 MPa. This approach can potentially overcome some of the experimental hindrances inherent in wave speed measurements (e.g., grain texture/microstructural effects, material geometry, residual stresses), such that an absolute stress measurement may be possible. In the next subsection, the estimation of residual stress in a wheel steel sample is performed using this approach.

8.2.2 Effects of Residual Stress on Ultrasonic Backscatter

The residual stress generated via heat treatment such as water quenching plays an important role in determining the service lifetime of railroad wheels. A compressive residual stress can stop initiation and propagation of minor cracks, while a tensile residual stress could speed up the growth of cracks, which could result in the splitting of the rim vertically from wheels. Therefore, determining the residual stress in railroad wheels is crucial for ensuring that the manufacturing processes were all optimal.

A 50 mm thick wheel slice was cut from a new wheel, and both the rim surface and cross section surfaces were polished to reduce the wave distortion from the surface roughness. Due to the complexity of the residual stress state in the railroad wheel, several assumptions regarding the stress based on the quenching process are made. First, it is assumed that there is no shear stress, only normal compressive stress. Second, it is assumed that the residual stress in the hoop direction (normal to the cross section surface) is completely released by cutting and polishing the cross section surfaces, such that only the residual stress in the cross section plane remains. Third, the residual stress in the axial direction is much higher than the residual stress along the radial direction. The primary residual stress in the railroad wheel is marked with red arrows shown in Fig. 8.3a. Both the cross section and rim surface were scanned using the ultrasonic L-L mode using a 10 MHz focused transducer (*Panametrics* V327, 2-inch focal length, *Olympus panametrics, Inc.*, Waltham, MA) with a focal depth in the material of 9.0 mm (scan step size = 1.0 mm and 0.25 mm for measurement of the

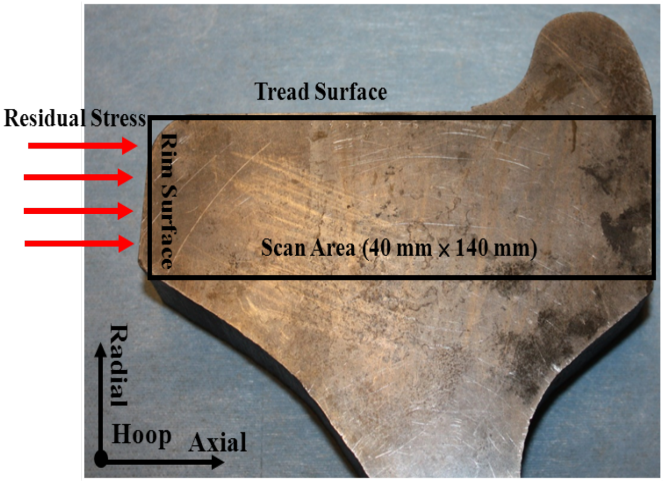

(a)

(b)

Figure 8.3: (a) Cross section and (b) rim surface images of a 50 mm thick wheel sample.

rim surface and the cross section, respectively; scan speed = 3.0 mm/s). Figs. 8.3a and 8.3b show the scan areas on the polished cross section and rim surface, respectively. The spatial variance curves were calculated by using the collected ultrasonic signals measured from the rim surface and the cross section surface. Next the whole wheel sample was annealed to remove the residual stress. The annealing procedure included heating the sample to 550 °C, maintaining the temperature for 3 hours, then switching off the heat and cooling the sample slowly to room temperature within the oven. Here only the residual stress was removed completely while the grain sizes and microstructure did not change during annealing. The cross section and rim surfaces were rescanned with the same experimental settings, and the spatial variance curves were recalculated after annealing.

Fig. 8.4 shows the spatial variance curves measured from the rim surface of the wheel sample before and after annealing along with the theoretical curve fits given by Eq. (8.1). The solid lines are the experimental variance curves, while the dashed lines are the theoretical response. It can be seen that the variance curve profile does not change, only the variance amplitude decreases by around 12.0 % after releasing the residual stress, a result that implies that the grain size and microstructure did not change during annealing. The result also agrees well with the expectation for iron that the release of the compressive residual stress will result in a decrease of the variance amplitudes for the L-L Ξ_{1111}^{1111} mode.

The whole cross section shown in Fig. 8.3 was scanned and the spatial variance curve for each 5 mm × 5 mm subarea containing about 400 waveforms was calculated before and after removing residual stress. The variance curves were fit with Eq. (8.1). Figs. 8.5a and 8.5b show the spatial variance maxima with colors before and after annealing. By comparing these two images, it can be observed that releasing the residual stress does not change the distribution pattern of variance amplitudes, an

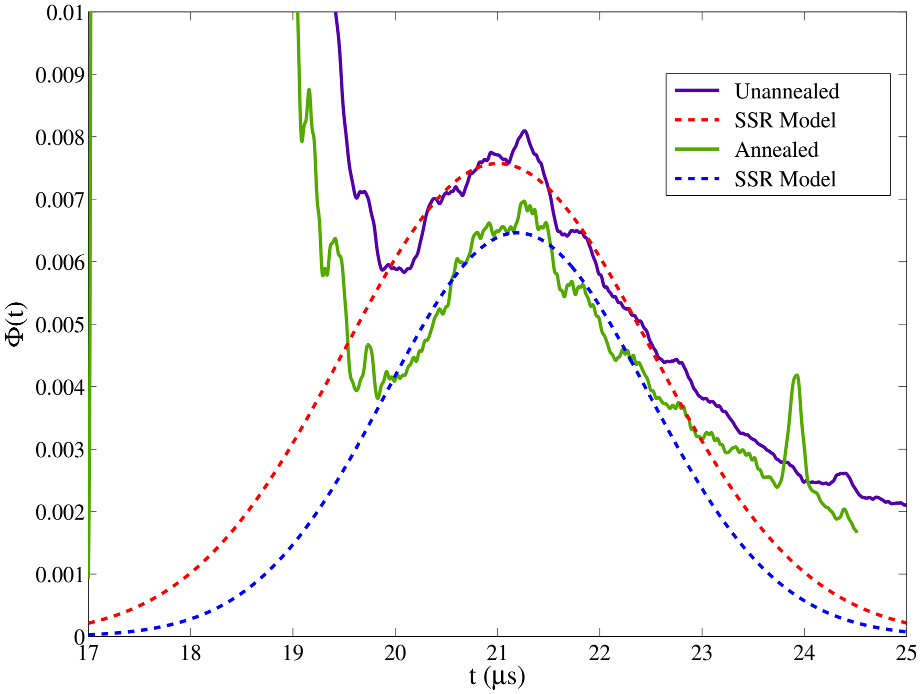

Figure 8.4: The variation of spatial variance amplitudes after annealing from the rim surface.

outcome that indicates that the microstructure does not change by annealing. The progressive increase of variance amplitudes from the quenched surface (tread and rim surfaces) to deeper locations shown in Fig. 8.5 is attributed to the increase of lamellar spacing instead of residual stress.

To quantify the changes of the variance amplitudes after removing the residual stress, three locations (about 15 mm, 20 mm and 25 mm away from the rim surface, respectively) marked with red dashed lines in Fig. 8.5b were chosen for comparison. Fig. 8.6 shows the change of spatial variance amplitudes for three locations with and without residual stress. It can be seen that the increase of variance amplitudes appears at almost all the positions. The result indicates that the primary residual stress is compressive according to the stress-dependent backscatter model given by Eq. (8.5)

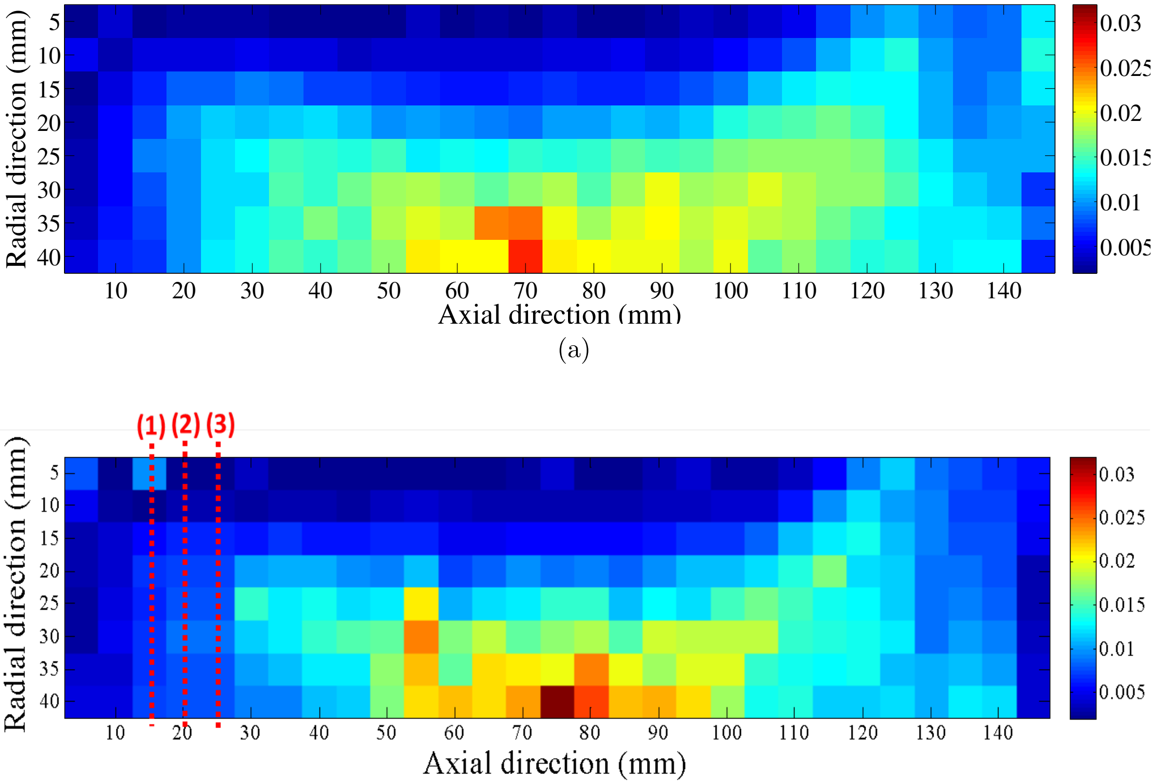

(a)

(b)

Figure 8.5: Variance amplitude distribution on the cross section of the wheel slice,(a) before annealing, (b) after annealing.

for the L-L (Ξ^{3333}_{3333}) mode. The point marked with a red circle in Fig. 8.6 indicates a decrease of the spatial variance amplitude, a result that might be attributed to tensile residual stress at this location. The average variance amplitude increases by about 8.0 % after removing residual stress. In contrast to that measured from the rim surface using the L-L (Ξ^{1111}_{1111}) mode, the result demonstrates an opposite trend. The experimental results match the theoretical predictions given by the Eq. (8.5) that a compressive residual stress will increase the variance amplitudes for which the ultrasound propagates parallel to the residual stress (Ξ^{1111}_{1111}), while it will decrease the variance amplitudes if the propagation direction of ultrasound is perpendicular to the residual stress (Ξ^{3333}_{3333}).

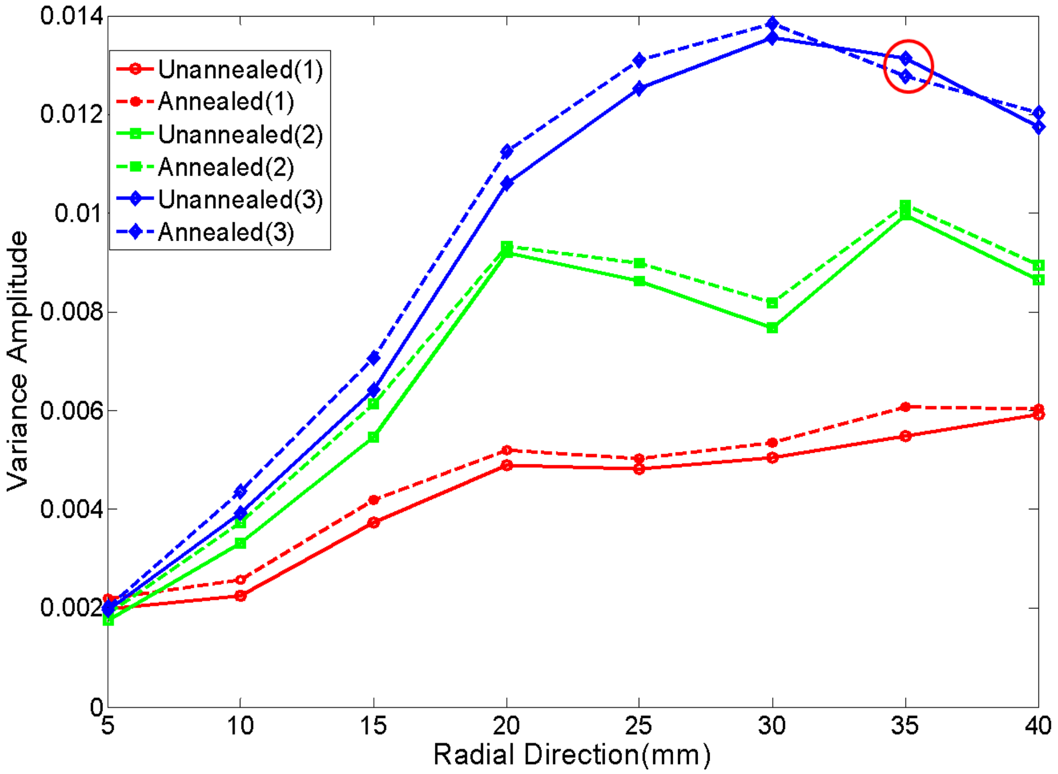

Figure 8.6: Comparison of spatial variance curves before and after annealing measured from the cross section.

The residual stress along the axial direction is estimated based on the variation of spatial variance amplitudes and the stress-dependent backscatter model. The numerical value of the residual stress along the axial direction is around -200 MPa at the depth of 9 mm from the rim surface. Lonsdale et al. [73] measured the axial residual stress in the wheel sample with the X-ray diffraction system. The measured value is about -130 MPa at about 50 mm depth from the rim surface. The mismatch between X-ray measurement and ultrasonic measurement might be attributed to several reasons: First, both wheel samples are not from the same quenched wheel. Second, the measurement positions are not identical. The residual stress near the rim surface should be much larger than that at a deeper location. Third, the second and third order elastic constants of single crystal of pure iron are utilized for estimating residual stress. Lastly, the real residual stress status in a quenched wheel is more complicated than the assumptions used here. More studies are required on residual stress measurements in quenched wheels.

8.2.3 Water Quenching

In this subsection, water quenching is used to study residual stress. A 1080 steel block was quenched unidirectionally with running water to generate residual stress. The measurement of residual stress was realized by quantifying the variation of spatial variance amplitudes using the L-L mode after releasing residual stress via annealing. The quenched surface of the 1080 steel block was scanned before and after relieving residual stress. The residual stress in the 1080 steel block along the quenching direction was estimated according to the change of spatial variance amplitude and the developed stress-dependent backscatter coefficients of pure iron.

The surface of a 1080 steel sample was prepared by polishing with fine sand paper before diffuse backscatter experiments. Fig. 8.7 shows an image of the polished quench surface of the block. The polished quench surface was scanned using a 10 MHz focused transducer with a focal depth in the material of 9.0 mm (scan step size = 0.25 mm; scan speed = 3.0 mm/s). The scan area was 40 mm × 40 mm. The spatial variance of the collected backscatter signals was calculated with a collection of over 5000 waveforms. The red solid line in Fig. 8.9 represents the spatial variance curve for the whole scan area shown in Fig. 8.7.

Fig. 8.8 shows the experimental setup for the water quench. The 1080 steel sample was heated up to 850 °C and held at that temperature for 3 hours in an oven. Then it was placed on the bridge and water was used to quench the sample surface. The area shown in Fig. 8.7 was rescanned with the same experimental settings after

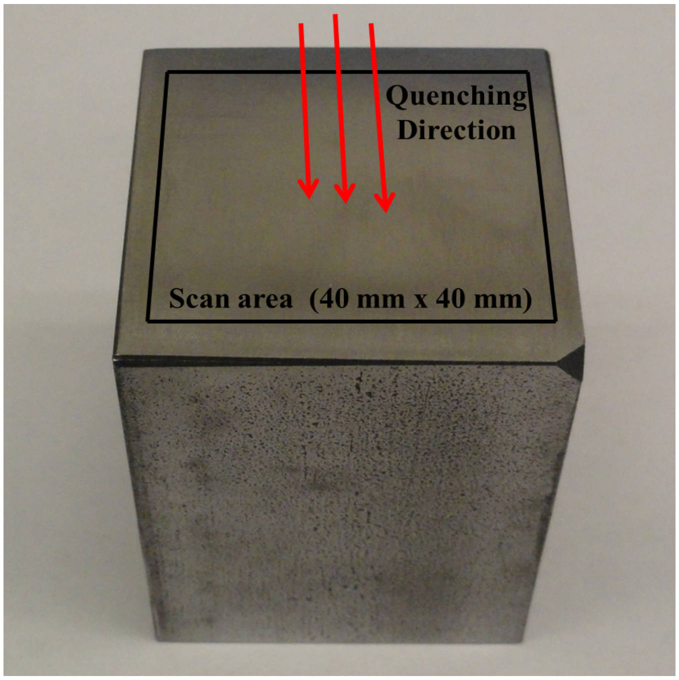

Figure 8.7: Image of a 1080 steel block (2 inch × 2 inch × 3 inch).

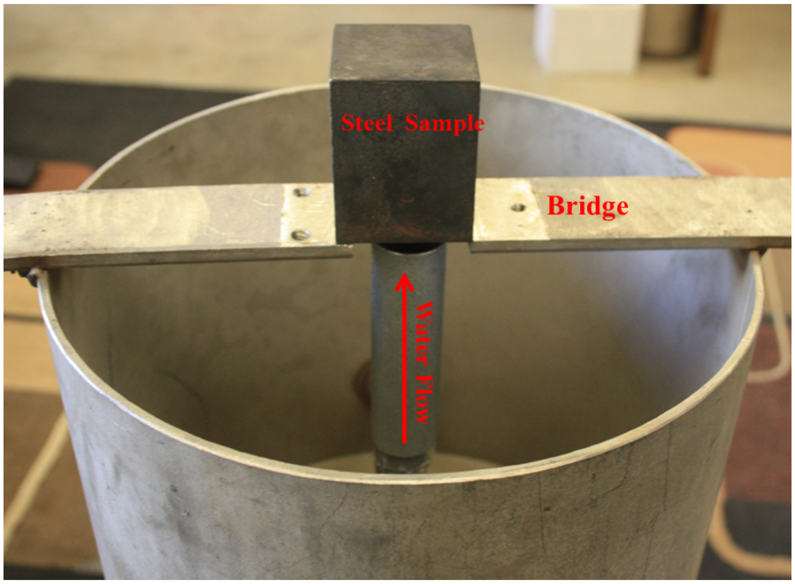

Figure 8.8: Experimental setup for quench with running water.

the water quench and the spatial variance curve of ultrasonic backscatter signals was recalculated. The green dashed line in Fig. 8.9 shows the spatial variance curve after quenching. It can be seen that the amplitude drops dramatically after quenching, an outcome that is attributed to the creation of lamellar duplex microstructure (pearlite phase) within grains that has been discussed in chapter 4 along with residual stress introduced via quenching. Here the dependence of ultrasonic scattering on residual stress is targeted. Several assumptions on the status of residual stress in the quenched sample are made: there is no shear stress in the sample and the residual stress is compressive in all directions. To separate the effects of residual stress microstructure, the quenched sample was annealed to remove the residual stress. The annealing process involved heating up the sample to 550 °C, holding the temperature for three hours, then switching off the oven to let the sample cool down slowly to room tempera-

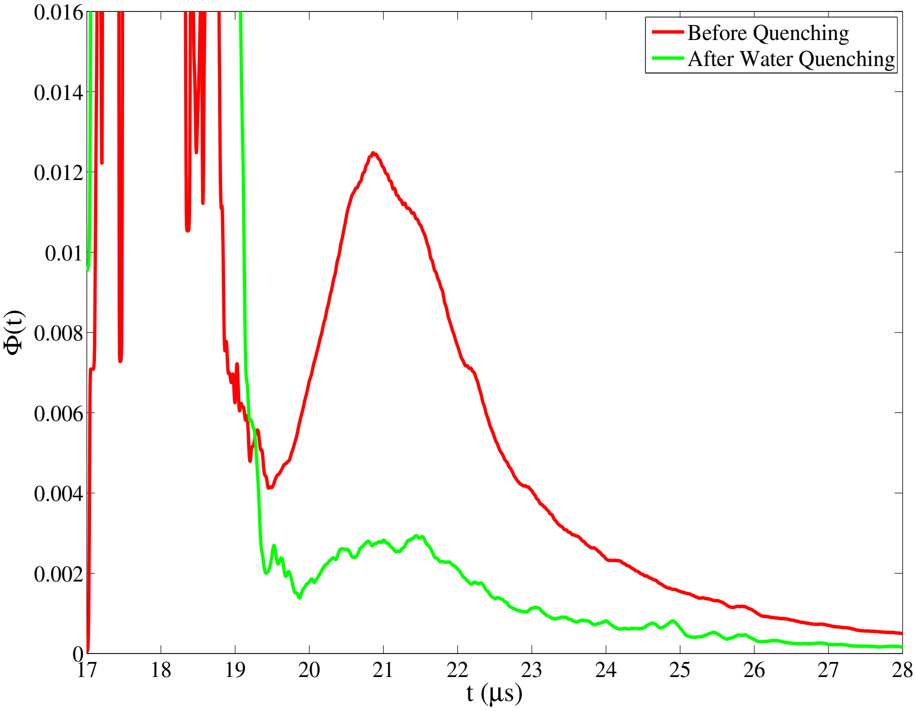

Figure 8.9: Comparison of spatial variance curves before and after water quenching.

ture within the oven. The residual stress is removed completely by annealing, while the grain sizes and the duplex microstructure are assumed unchanged during annealing. The quenched surface was rescanned with the same experimental settings after annealing.

Fig. 8.10 shows the spatial variance curves measured at normal incidence for the whole scan area shown in Fig. 8.7 as well as the curve fits given by Eq. (5.2). The solid green and blue lines represent the spatial variance curves measured from the quench surface before and after annealing, respectively, while the dished lines are the curve fits using the depth-dependent SSR model given by Eq. (5.2). It can be seen that the SSR model that includes the gradation of lamellar spacing along the propagation path fits well with the variance curve measured from the quenched surface. The solid

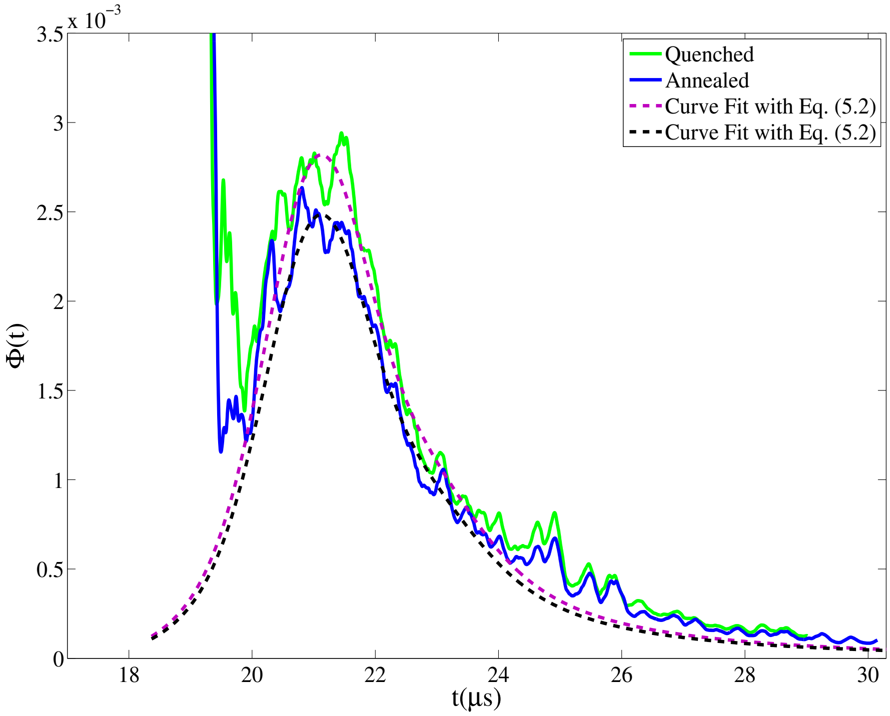

Figure 8.10: Spatial variance curves measured from the whole quenched surface after quenching and after annealing with the normal incidence ultrasound.

green and blue lines represent the spatial variance curves measured from the quench surface before and after annealing, respectively, while the dished lines are the curve fits using the depth-dependent SSR model given by Eq. (5.2). It can be seen that the SSR model that includes the gradation of lamellar spacing along the propagation path fits well with the variance curve measured from the quenched surface. By comparing these two curves, it can be observed that the profiles are very similar, a result which implies that the grain size and microstructure do not change as anticipated. The spatial variance amplitudes are determined after fitting the curves with Eq. (5.2), such that the change of variance amplitudes is quantified. This amplitude decreases by 11.89 %, a result that can be used to estimate the residual stress according to the developed stress-dependent backscatter model.

Fig. 8.11 demonstrates the estimated residual stress state in the quenched steel block. Here several specific cases of residual stress states are considered, and the stress-dependent backscatter coefficients K_0, K_1 and K_2 shown in Eq. (8.5) are calculated for each case. Table 8.3 shows the calculated stress-dependent backscatter

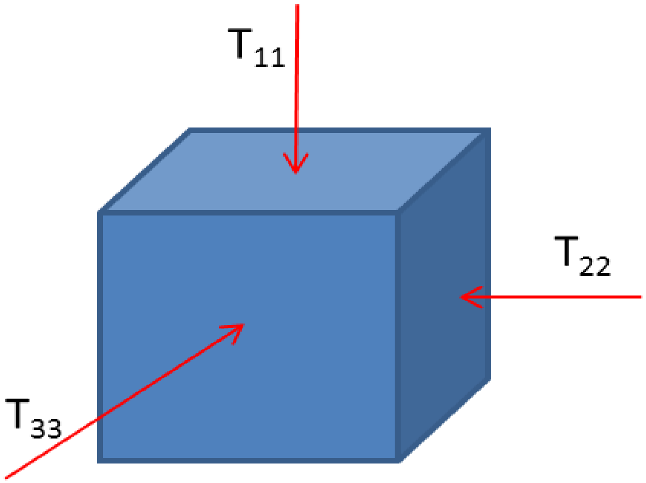

Figure 8.11: The residual stress state in the quenched steel block, the normal direction of the quenched surface is parallel to T_{11}.

Table 8.3: Theoretical backscatter coefficients of pure iron under five residual stress states, respectively [39].

Cases	$K_0(\text{GPa}^2)$	$K_1(\text{GPa})$	K_2	Residual Stress (MPa)
1. $(T_{22} = T_{33} = 0)$	582.1	-341.4	80.76	$T_{11} = -208.3$
2. $(T_{11} = 4T_{22} = 4T_{33})$	582.1	-250	31	$T_{11} = -275, T_{22} = T_{33} = -68.75$
3. $(T_{11} = 2T_{22} = 2T_{33})$	582.1	-175.1	5.9	$T_{11} = -404, T_{22} = T_{33} = -202$
4. $(T_{11} = T_{22} = T_{33})$	582.1	-10.3	-16.6	$T_{11} = T_{22} = T_{33} = -6674$
5. $(T_{11} = 0, T_{22} = T_{33})$	582.1	320.1	74	$T_{22} = T_{33} = 214.8$

coefficients of pure iron for each case and the estimated residual stress subject to the change of variance amplitude. It can be seen that the calculated residual stress is significantly dependent on the residual stress state. If the residual stress state is assumed hydrostatic (case 4), the value of the estimated residual stress is so large that it does not make sense. If it is assumed that there is no residual stress in the normal direction, the obtained residual stress in the quenched plane is tensile stress, a result that does not match the experimental observations. The average compressive residual stress along the quench direction is estimated around -208 MPa if no residual stress ($T_{22} = T_{33} = 0$) in the plane is considered. Thus, for the following discussion, the residual stress state is assumed such that there is only residual stress in the quench direction, no residual stress in the quench plane ($T_{22} = T_{33} = 0$).

To examine the distribution of residual stress on the whole quench surface, the scan area (40 mm × 40 mm) shown in Fig. 8.7 is divided into 4 × 4 subareas for calculating the spatial variance curves, respectively. About 400 collected waveforms were included in calculating the spatial variance curve for each subarea. Then the SSR model given by Eq. (5.2) is used to fit the variance curves to extract the variance maximum before and after annealing for each subarea, respectively. The change of variance maximum is quantified for each subarea. Based on the developed stress-dependent backscatter model, the changes of variance peaks are transferred to the estimated residual stress along the quenching direction by applying the elastic constants of the pure iron for the 1080 steel.

Fig. 8.12 shows the distribution of the calculated residual stress along the quenching direction with different colors. It can be seen that the calculated compressive residual stress along the quenching direction appears among the whole scanning area. The results show that the compressive residual stress is distributed over the whole quenched surface. The values of the estimated compressive residual stress range from -105 MPa to -340 MPa, and increase along the Y direction in general. The calculated maximum compressive residual stress appears at the bottom of the left column with coordinates (5,35), while the minimum residual stress locates at the top of the left

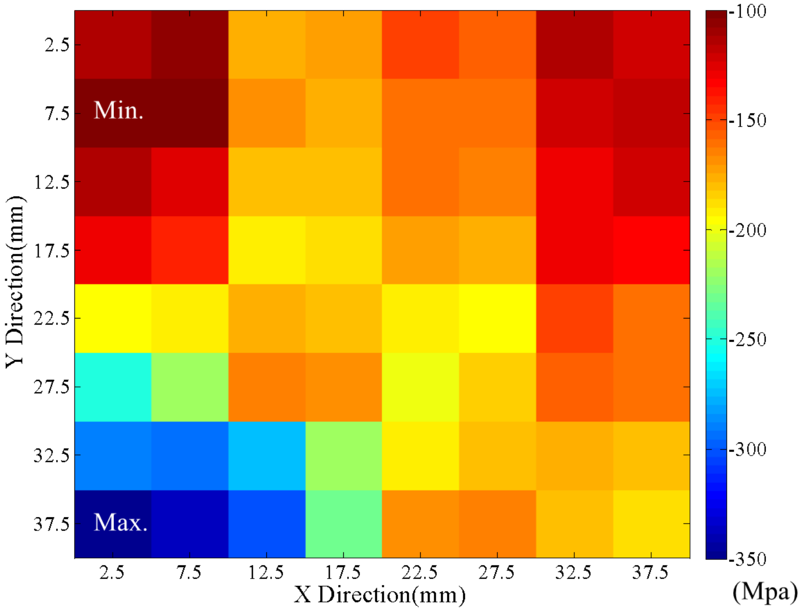

Figure 8.12: Distribution of the estimated residual stress (MPa) along the quenching direction based on the elastic constants of pure iron.

column (5,5). The errors of the estimated residual stress might come from the curve fitting as well as the application of the elastic constants of pure iron for the 1080 steel. Hossain el al. [74] presented results from an experimental and numerical study on triaxial residual stresses generated by spray water quenching in solid cylinders and spheres samples made from type 316H stainless steel. The results showed that highly compressive residual stresses occurred around the surfaces of the cylinders and spheres and tensile residual stresses occurred near the center. The compressive residual stress value is similar to the estimate of residual stress in the quenched 1080 steel block given here.

Figs. 8.13 and 8.14 demonstrate the spatial variance curves before and after annealing for the subareas that exhibit the minimum and maximum changes of the variance peaks after removing the residual stress, respectively. It can be seen that

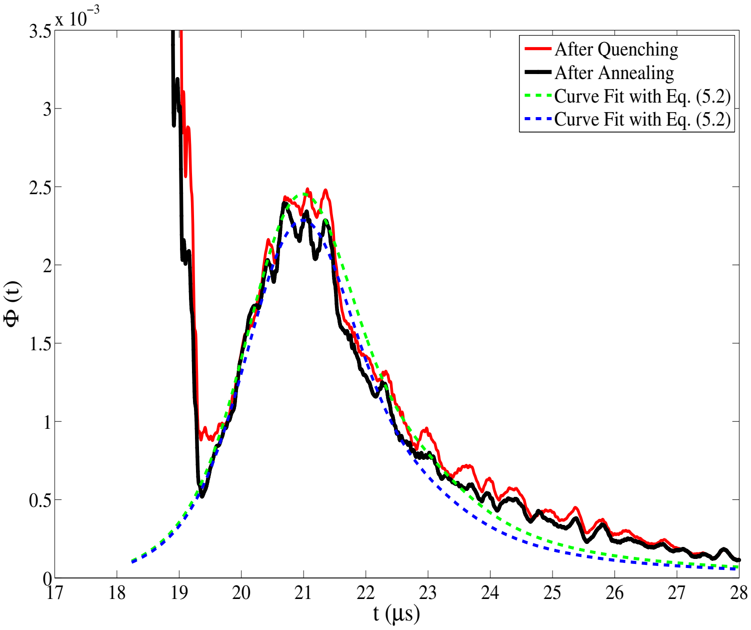

Figure 8.13: Variance curves before and after annealing at the subarea with minimum amplitude change as shown in Fig. 8.12.

the profiles of variance curves scarcely change after annealing, only the amplitudes decrease after removing the residual stress for both two subareas, results that further verify that the changes of variance curves are attributed to the removal of the residual stress rather than the change of the grain size or the duplex microstructure. The curve fits given by Eq. (5.2) match well with the variance curves near the peaks. The changes of variance amplitudes are quantified of 6.47 % and 24.47 %, respectively. The results demonstrate the significant dependence of ultrasonic scattering on residual stress. It may be possible to use this approach as a new nondestructive method for measuring residual stress in the future.

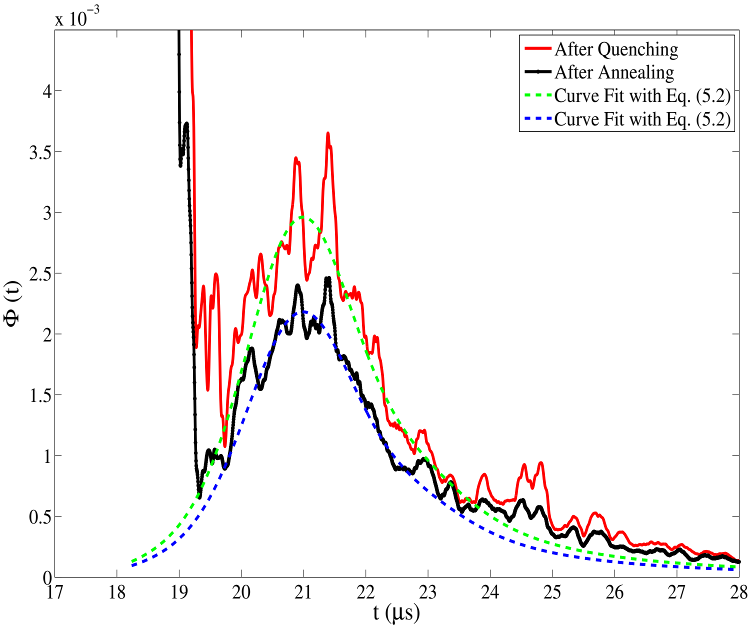

Figure 8.14: Variance curves before and after annealing at the subarea with maximum amplitude change as shown in Fig. 8.12.

8.3 Summary

In this chapter, the dependence of ultrasonic backscatter on stress was studied by quantifying the variation of the spatial variance amplitudes under the applied unidirectional load. Typical experiments were performed by acquiring waveforms with a focused transducer in a pulse-echo configuration for which the ultrasonic propagation direction is normal to the steel block but perpendicular to the loading direction. The experimental results show a decreasing trend with increasing compressive stress as predicted from the theory.

Based on the experimental observation, residual stress in the railroad wheel sample was estimated by quantifying the variation of variance amplitudes after removing residual stress via annealing. Both the rim surface and the cross section surface were scanned with a focused transducer in a pulse-echo configuration. The experimental results show that the variance amplitudes decrease about 12 % and increase about 8.0 % for the measurement from the rim surface and the cross section surface after annealing, respectively, a result that matches the predicted results from the theory. The estimated residual stress in the axial direction of a new wheel sample at a depth of 9 mm from the rim surface is around -200 MPa with respect to an assumption that the primary residual stress is parallel to the quenching direction.

A 1080 steel block was quenched unidirectionally with running water to introduce residual stress along the quench direction. It was observed that the ultrasonic scattering response decreased dramatically after quenching. The effect of residual stress on ultrasonic scattering was quantified by evaluating the change of the spatial variance amplitudes after removing the residual stress via annealing. The experimental results show that the average variance amplitude decreases by about 11.89 % based on normal incidence measurement. The average residual stress along the quench direction was estimated with respect to different assumptions of the residual stress state. The value of residual stress along the quench direction was calculated to be around -230 MPa at a depth of 9 mm with an assumption that the primary residual stress was parallel with the quench direction. The whole scan area was divided into 4×4 sub-areas to map the residual stress in the quench direction. The result illustrated that the compressive residual stress appears over the whole scanning area. The calculated stress value ranges from about -105 MPa to -340 MPa. Diffuse ultrasonic backscatter signals show a high sensitivity to residual stress so that this technique may be developed into an non-destructive method of measuring residual stress in the future.

Chapter 9

Conclusions and Future Work

In this dissertation, diffuse ultrasonic backscatter techniques were used to inspect railroad wheels. A new singly-scattered response (SSR) model that accounted for pearlitic microstructure within grains was developed based on the previous SSR model [24], [46] to evaluate lamellar duplex microstructure. The spatial variance amplitudes of the collected ultrasonic backscatter signals captured at many positions dropped dramatically near the tread surface of a quenched wheel due to the creation of the fine pearlite phase during quenching. The lamellar spacing was estimated using the developed SSR model, and the results showed a good agreement with optical micrograph observations. A graded SSR model was also developed to investigate the effects of the graded duplex microstructure within grains on ultrasonic scattering along the propagation path. The quench depth was measured accurately by fitting the variance curve measured from the tread surface with the graded SSR model using the least squares error method. In addition, expressions of ultrasonic attenuation in pearlitic steel were developed. The ultrasonic attenuation measured in a pearlitic wheel steel showed a good agreement with theoretical predictions. The effects of mode-converted (L-T) ultrasonic backscatter on pearlitic microstructure were also studied. The variance amplitudes measured in two directions on the cross section of a wheel sample were different due to the different effective interaction lengths and/or the preferred orientation of the duplex crystallites within grains.

Diffuse ultrasonic backscatter and ultrasonic attenuation demonstrate significant sensitivities to lamellar duplex microstructure within grains (pearlite), such that they can serve as non-destructive methods to evaluate pearlitic microstructure, to measure grain elongation, texture and the quench depth, which can be used for quality control in conjunction with other processes. However, there are still some problems and limitations from both the SSR modeling and ultrasonic backscatter experiments that need further investigation. First, the assumptions of the identically oriented duplex crystallites within an individual grain and of the randomly oriented crystallites within grains may be sources that cause the mismatch between the measured attenuation and the theoretical predictions at deeper locations. The micrographs showed that the duplex crystallites within an individual grain were often divided into multiple domains with different orientations. Some preferred orientation or texture may exist due to the non-uniform cooling rate, especially, at deeper locations. Second, the simplification of duplex crystallites within an individual grain as circular plates with the same diameter dimension (equal to the correlation length) and the same thickness (equal to the lamellar spacing) may lead to errors in the evaluation of lamellar spacing. The diameter dimension of a duplex crystallite was dependent on the location within a grain. The dimension was much smaller near the grain boundaries compared with that near the center of a grain. Therefore, the simplification that all the duplex crystallites within a grain had the same geometries may influence the final results. Lastly, the assumption that the inner product on the eighth-rank covariance tensor for lamellar duplex microstructure within a grain was equal to the same quantity when the lamellae were absent may also contribute to the mismatch and influence the final evaluation of lamellar spacing. The pure ferrite phase steel with a body-center cubic crystal structure is soft and ductile, while the pure cementite phase steel with a face-center cubic crystal is very hard and brittle. All these assumptions should be reconsidered in the future.

In addition to theoretical limitations, there are also some limitations of the ultrasonic backscatter and attenuation measurements that are a concern. First, because all the inspected samples were cut from only a single quenched wheel, more wheel samples (including unquenched and quenched) from other wheel plants made with different manufacturing processes need to be inspected to investigate further the effects of microstructural changes on ultrasonic backscatter due to the different manufacturing processes. Second, the variance amplitude measured using a 10 MHz transducer was much higher than that measured using a 15 MHz at the deeper locations, a result which was very different from that measured near the tread surface. In addition, the estimated lamellar spacings from the 10 MHz and 15 MHz measurements were not identical. Therefore, more work is needed to investigate if there is some frequency dependence and what is the most appropriate frequency range. Third, mismatches between the experimental attenuation, mode-converted backscatter and the theoretical predictions were observed at deeper locations, outcomes that might be attributed to the larger grains, much larger lamellar spacing, or the preferred orientation of duplex crystallites. More measurements are needed to find the sources of these mismatches. Finally, more ultrasonic measurements including those at multiple frequencies and/or multiple modes are needed to estimate the factor M directly.

In this dissertation, the dependence of ultrasonic backscatter on stress was also studied. The ultrasonic backscatter was measured on the side surface of a 1018 steel block under a uniaxial stress load. The experimental results demonstrated a decreasing trend of ultrasonic backscatter, an outcome that was similar to the theoretical prediction based on the stress-dependent covariance tensor of elastic moduli. The average residual stress in a quenched steel sample was estimated to be -230 MPa at a depth of 9 mm in the quench direction from the average 11.86 % change of variance amplitudes with and without residual stress. Diffuse ultrasonic backscatter demonstrates a high sensitivity to stress so that this technique may be developed potentially as a non-destructive method for residual stress measurement. However, there are also some limitations that need further examination. First, the slope of the measured variance amplitudes versus uniaxial stress was very different from the theoretical prediction, a result that might be attributed to the use of the elastic constants of steel with that of pure iron. Second, the real residual stress state in a quenched sample was more complicated than the assumption that there was not shear residual stress and that the primary residual stress was parallel to the quench direction. All the residual stress components can affect the ultrasonic backscatter, so that this assumption can cause some errors in the estimate of residual stress. Finally, due to the limit of the current experimental facilities, the residual stress in the quenched sample can not be confirmed using other techniques, such as X-ray diffraction or neutron diffraction. Therefore, more work is needed to show precisely how the backscatter depends on stress.

The future work will target the limitations and problems as listed above. The objectives of the future theoretical research will focus on the modification of the SSR and attenuation models by including the different elastic properties of ferrite and cementite phases, and by considering the preferred orientations of duplex microstructure at deeper locations due to the non-uniform cooling rate to make the theoretical predictions match better with the experimental results. Other methods of simplifying the duplex crystallites within a grain, such as circular plates with varying position-dependent diameter dimensions within a grain, will also be applied for comparison with the current simplified approach. The major objectives of the future experimental research will focus on investigating the appropriate frequency range and applying different frequencies to obtain the parameters that define the lamellar spacing. Then multiple ultrasonic backscatter measurements will be made to extract the lamellar spacing, the factor M, the correlation length and the residual stress simultaneously using multiple frequencies (7.5 MHz, 10 MHz, 15 MHz and so on) and multiple modes (including L-L, L-T and T-T). In addition, other techniques such as X-ray diffraction or neutron diffraction will be used for measuring residual stress in quenched steel samples to compare with ultrasonic backscatter measurements.

Bibliography

[1] R. B. Thompson, “Elastic-wave propagation in random polycrystals: fundamentals and application to nondestructive evaluation,” Appl. Phys. **84**, 234-255 (2002).

[2] I. M. Lifshits and G. D. Parkhomovski,“On the theory of ultrasonic wave propagation in polycrystals,” Zh. Eksp. Teor. Fiz. **20**, 175-182 (1950).

[3] E. P. Papadakis, “Ultraonic attenuation caused by scattering in polycrystalline media,” in: *Physical Acoustics*, edited by W. P. Marson, **4**, Part B, (Academic Press, London, NY), 269-328 (1968).

[4] L. G. Merkulov, “Investigation of ultrasonic scattering in metals,” Sov. J. Technol. Phys. **26**, 59-69 (1956).

[5] S. Hirsekorn, “The scattering od ultrasonic waves by polycrystals,” J. Acoust. Soc. Am. **72**, 1021-1031 (1982).

[6] F. E. Stanke and G. S. Kino, “A unified theory for elastic wave propagation in polycrystalline materials,” J. Acoust. Soc. Am. **75**, 665-681 (1984).

[7] R. L. Weaver, “Diffusivity of ultrasound in polycrystals,” J. Mech. Phys. Solids **38**, 55-86 (1990).

[8] F. J. Margetan, R. B. Thompson, and I. Yalda-Mooshabad, "Backscattered microstructural noise in ultrasonic toneburst inspection," J. Nondestruct. Eval. **13**, 111-136 (1994).

[9] S. Ahmed and R. B. Thompson, "Attenuation of ultrasonic waves in cubic metals having elongated, oriented grains," Nondestr. Test. Eval. **8**, 525-531 (1992).

[10] J. A. Turner, "Elastic waves propagation and scattering in heterogeneous anisotropic media: textured polycrystalline materials," J. Acoust. Soc. Am. **106**, 541-552 (1999).

[11] L. Yang, J. A. Turner, and Z. Li, "Ultrasonic characterzation of microstructure evolution during processing," J. Acoust. Soc. Am. **121**, 50-59 (2007).

[12] C. B. Guo, P. Höller, and K. Goebbels, "Scattering of ultrasonic waves in anisotropic polycrystalline metals," Acustica **59**, 112-120 (1985).

[13] F. J. Margetan, T. A. Gray, and R. B. Thompson, "A technique for quantitative measuring microstructurally induced ultrasonic noise," in *Review of Progress in Quantitative NDE*, edited by D. O. Thompson and D. E. Chimenti, volume 10, 1721 -1728 (Plenum Press, New York) (1991).

[14] R. L. Weaver, "Diffuse waves in finite plates," J. Sound and Vibr. **94**, 319-335 (1984).

[15] J. A. Turner and R. L. Weaver, "Time dependence of multiply scattered diffuse ultrasound in polycrystalline media," J. Acoust. Soc. Am. **97**(5), 2639-2644 (1995).

[16] J. A. Turner and R. L. Weaver, "Radiative transfer of ultrasound," J. Acoust. Soc. Am. **96**, 3654-3674 (1994).

[17] J. A. Turner and R. L. Weaver, “Radiative transfer and multiple scattering of diffuse ultrasound in polycrystalline media,” J. Acoust. Soc. Am. **96**, 3675-3683 (1994).

[18] R. L. Weaver and W. Sachse, “Diffusion of ultrasound in a glass bead slurry,” J. Acoust. Soc. Am. **97**, 2094-2102 (1995).

[19] R. B. Thompson and T. A. Gray, “A model relating ultrasonic scattering measurement through liquid-solid interfaces to unbounded medium scattering amplitudes,” J. Acoust. Soc. Am. **74**, 1279-1290 (1983).

[20] J. H. Rose, “Ultrasonic backscattering from polycrystalline aggregates using time-domain linear response theory,” in *Review of Progress in Quantitative NDE*, edited by D. O. Thompson and D. E. Chimenti, volume 10, 1715-1720 (Plenum Press, New York) (1991).

[21] L. W. Schmerr, “Fundamentals of ultrasonic nondestructive evaluation, a modeling approach,” (Plenum Press, New York) (1998).

[22] F. J. Margetan, A. Li, and R. B. Thompson, “The influence of inspection angle, wave type and beam shape on signal-to-noise ratios in ultrasonic pitch-catch inspections,” in *Review of Progress in Quantitative NDE*, edited by D. O. Thompson and D. E. Chimenti, volume 894, 571-578 (American Institute of Physics, New York) (2007).

[23] R. B. Thompson, F. Margetan, P. Haldipur, L. Yu, A. Li, P. Panetta, and H. Wasan, “Scattering of elastic waves in simple and complex polycrystals,” Wave Motion **45**, 655-674 (2008).

[24] G. Ghoshal, J. A. Turner, and R. L. Weaver "Wigner distribution of a transducer beam pattern within a multiple scattering formalism for heterogeneous solids," J. Acoust. Soc. Am. **122**, 2009-2021 (2007).

[25] B. D. Cook and W. J. Arnoult III, "Gaussian-Laguerre/Hermite formulation for the nearfield of an ultrasonic transducer," J. Acoust. Soc. Am. **59**, 9-11 (1976).

[26] J. E. Gubernatis, E. Domany, and J. A. Krumhansl, "Formal aspects of the theory of the scattering of ultrasound by flaws in elastic materials," J. Appl. Phys. **48**, 2804-2811 (1977).

[27] R. B. Thompson and T. A. Gray, "A model relating ultrasonic scattering measurement through liquid-solid interfaces to unbounded medium scattering amplitudes," J. Acoust. Soc. Am. **74**, 1279-1290 (1983).

[28] L. W. Schmerr and S. J. Song, "Ultrasonic nondestructive evaluation system," (Springer, New York) (2007).

[29] M. L. Oleze and J. F. Zachary, "Examination of cancer in mouse models using highfrequency quantitative ultrasound," Ultrasound in Med. and Biol. **32**, 1639-1648 (2006).

[30] D. M. Egle and D. E. Bray, "Ultrasonic measurement of longitudinal rail stresses," Mater. Eval. **378**, 41-46 (1979).

[31] M. Hirao, H. Ogi, and H. Yasui, "Contactless measurement of bolt axial stress using a shear-wave electromagnetic acoustic transducer," NDT & E Int. **34**, 179-183 (2001).

[32] A. Santos and D. E. Bray, "Ultrasonic stress measurement using PC based and commercial flaw detectors," Rev. Sci. Instrum. **71**, 3464-3469 (2000).

[33] N. Kim and M. Hong, “Measurement of axial stress using mode-converted ultrasound,” NDT & E Int. **42**, 164-169 (2009).

[34] Standard practice for Railway applications. Wheelsets and bogies. Wheels. Product requirements. No. BS EN 13262:2004+A2:2011, BSI, 2004.

[35] Standard practice for Non-destructive acceptance testing. Solid-rolled wheels, rims and wheel pairs axles of rolling stock. No. RD32.144-2000. Moscow, 2000.

[36] T. K. Ballabh, M. Paul, T. R. Middya, and A. N. Basu, “Theoretical multiple-scattering calculation of nonlinear elastic constants of disordered solids,” Phys. Rev. B. **45**, 2761-2771(1992).

[37] L. Ryzhik, G. Papanicolaou, and J. B. Keller, “Transport equations for elastic and other waves in random media,” Wave Motion **24**, 327-370 (1996).

[38] B. E. Powell and M. J. Skove, “Linear and volume compressibilities and isothermal third-order elastic constants,” J. Appl. Phys. **56**, 1548-1549 (1984).

[39] J. A. Turner and G. Ghoshal, “Polycrystals under applied loads: Second-order grain statistics,” Appl. Phys. Lett. **97**, 031907 - 031907-3 (2010).

[40] C. M. Kube, H. Du, G. Ghoshal, and J. A. Turner, “Stress-dependent changes in the diffuse ultrasonic backscatter coefficient in steel: Experimental results,” J. Acoust. Soc. Am. **132**, EL43-EL48 (2012).

[41] R. B. Thompson, F. Margetan, P. Haldipur, L. Yu, A. Li, P. Panetta, and H. Wasan, “Scattering of elastic waves in simple and complex polycrystals,” Wave Motion **45**, 655-674 (2008).

[42] J. Mamou, M. L. Oelze, W. D. O'Brien, Jr., and J. F. Zachary, "Identifying ultrasonic scattering sites from three-dimensional impedance maps," J. Acoust. Soc. Am. **117**, 413-423 (2005).

[43] S. Hirsekorn, "The scattering od ultrasonic waves by polycrystals, II. Shear waves," J. Acoust. Soc. Am. **73** 1161-1163 (1982).

[44] L. Yang, O. I. Lobkis, and S. I. Rokhlin, "Explicit model for ultrasonic attenuation in equaxial hexagnal polycrystalline materials," Ultrasonics **51**, 303-309 (2011).

[45] L. Yang, O. I. Lobkis, and S. I. Rokhlin, "Shape effect of elongated grains on ultrasonic attenuation in polycrystalline materials," Ultrasonics **51**, 697-708 (2011).

[46] G. Ghoshal and J. A. Turner, "Diffuse ultrasonic backscatter at normal incidence through a curved interface," J. Acoust. Soc. Am. **128**, 3449-3458 (2010).

[47] J. H. Rose, "Ultrasonic backscatter from microstructure," in *Review of Progress in Quantitative NDE*, edited by D. O. Thompson and D. E. Chimenti, volume 11, 1677-1684 (Plenum Press, New York) (1992).

[48] Y. K. Han and R. B. Thompson, "Ultrasonic backscattering in duplex microstructures: theory and application to titanium alloys," Metall. Mater. Trans. A. **28A**, 91-104 (1997).

[49] O. I. Lobkis and S. I. Rokhlin, "Charaterization of polycrystals with elongated duplex microstructure by inversion of ultrasonic backscattering data," Appl. Phys. Lett. **96**, 161905 - 161905-3 (2010).

[50] O. I. Lobkis, L. Yang, J. Li, and S. I. Rokhlin, “Ultrasonic backscattering in polycrystals with elongated single phase and duplex microstructures,” Ultrasonics **52**, 694-705 (2012).

[51] O. I. Lobkis, L. Yang, J. Li, and S. I. Rokhlin, “An integrated model for ultrasonic wave propagation and scattering in a polycrystalline medium with elongated hexagonal grains,” Wave Motion **49**, 544-560 (2012)

[52] O. I. Lobkis and S. I. Rokhlin, “Ultrasonic propagation and scattering in duplex microstructures with application to titanium alloys,” J. Nondestruct. Eval. **31**, 270-285 (2012).

[53] F. Zeng, S. R. Agnew, B. Raeisinia, and G. R. Myneni, “Ultrasonic attenuation due to grain boundary scattering in pure niobium,” J Nondestruct. Eval. **29** 93-103 (2010).

[54] W. P. Mason and H. J. McSkimin, “Attenuation and scattering of high frequency sound waves in metals and glasses,” J. Acoust. Soc. Am. **19**, 464-473 (1947).

[55] W. P. Mason and H. J. McSkimin, “Physical acoustics and microstructure of iron alloys,” Inter. Metals Rev. **29**, 1-24 (1984).

[56] J. B. Keller, “Stochastic equations and wave propagation in random media,” in *Proc. 16th Symp. App. Math*, volume 16. 145-170 (Am. Math. Soc. New York) (1964).

[57] D. R. Askeland, “The science and engineering of materials,” (PWS-KENT Publishing company, Boston) (1989).

[58] P. D. Panetta and R. B. Thompson, “Ultrasonic attenuation in duplex titanium alloys,” in *Review of Progress in Quantitative NDE*, edited by D. O. Thompson

and D. E. Chimenti, volume 18 (Kluwer Academic, Plenum Publishers) 1717-1721 (1999).

[59] B. Rockstroh, F. Walte, W. Kappes, S. Bessert, M. Krning, W. Schfer, R. Dath, B. Blacker, J. Montnacher, F. Minich, A. Kushnarev, V. Kamardin, and Y. Smorodinskiy, "New ultrasound testing systems for the production testing of rail wheels," Insight-Non-Destructive Testing and Condition Monitoring, **49**(6), 333-336 (2007).

[60] H. W. Zhang, S. Ohsaki, S. Mitao, M. Ohnuma and K. Hono "Microstructural investigation of white etching layer on pearlite steel rail," Materials Science and Engineering: A **421**, 191-199 (2006).

[61] S. B. Newcomb and W. M. Stobbs, "A transmission electron microscopy study of the white-etching layer on a rail head," Materials Science and Engineering **66**(2), 195-204 (1984).

[62] F. Walther and D. Eifler, "Local cyclic deformation behavior and microstructure of railway wheel materials," Materials Science and Engineering: A **387-389** 481-485 (2004).

[63] J. H. Lee, J. H Jang, B. D. Joo, Y. M. Son, and Y. H. Moon, "Laser surface hardening of AISI H13 tool steel," Trans. Nonferrous Met. Soc. China **19**, 917-920 (2009).

[64] M. Hirao, H. Fukuoka, and H. Toda, "Non-destructive evaluation of hardening depth using surface-wave dispersion patterns," Journal of Mechanical Working Technology **8**, 171-179 (1983).

[65] K. Fujisawa andA. Nakanishi, "Hardening depth measurement by using ultrasonic backscattering," Nondestructive Testing Communications **4**, 131-136 (1989)

[66] L. Yang, J. Li, O. I. Lobkis, and S. I. Rokhlin, "Ultrasonic Propagation and Scattering in Duplex Microstructures with Application to Titanium Alloys," J Nondestruct. Eval. **31**, 270-283 (2012).

[67] H. Du, C. Lonsdale, J. Olive, B. M. Wilson, and J. A. Turner, "Evaluation of railroad wheel steel with Lamellar duplex microstructures using diffuse ultrasonic backscatter," J Nondestruct. Eval. **32**, 331-340 (2013).

[68] H. Du, C. Lonsdale, J. Olive, B. M. Wilson, and J. A. Turner, "Measurement of quench depth in railroad wheels by diffuse ultrasonic backscatter," J Nondestruct. Eval. (2013) DOI 10.1007/s10921-013-0207-7.

[69] P. Hu, C. M. Kube, L. M. Koester, and J. A. Turner, "Mode-converted diffuse ultrasonic backscatter," J. Acoust. Soc. Am. **134**(2), 982-990 (2013).

[70] L. W. Schmerr and S. J. Song, "Theoretical model of mode-converted diffuse ultrasonic backscatter," (Springer, New York, 2007, Chaps. 5, 6, and 8) (2007).

[71] H. Du and J. A. Turner, "Ultrasonic attenuation in pearlitic steel," Ultrasonics (2013), http://dx.doi.org/10.1016/j.ultras.2013.10.017.

[72] P. H. Rodgers and A. L. Van Buren, "An exact expression for the Lommel difraction correction integra," J. Acoust. Soc. Am. **55**, 724-728 (1974).

[73] C. Lonsdale, "Wheel Rim Axial Residual Stress and a Proposed Mechanism for Vertical Split Rim Formation," *ASME 2011 Rail Transportation Division Fall Technical Conference* (RTDF2011) September, 21-22 (2011).

[74] S. Hossain, C. E. Truman, D. J. Smith, and M. R. Daymond, “Application of quenching to create highly triaxial residual stresses in type 316H stainless steels,” International Journal of Mechanical Sciences **48**, 235-243 (2006).

[75] D. S. Hughes and J. L. Kelly, “Second order elastic deformation of solids,” Phys. Rev. **92**, 1145-1149 (1953).

[76] R. A. Toupin and B. Bernstein, “Sound waves in deformed perfectly elastic materials. Acoustoelastic effect,” J. Acoust. Soc. Am. **33**, 216-225 (1961).

[77] R. N. Thurston and K. Brugger, “Third-order elastic constants and the velocity of small amplitude elastic waves in homogeneously stressed media,” Phys. Rev. **133**, 1604-1610 (1964).

[78] T. Bateman, W. P. Mason, and H. J. McSkimin, “Third-order elastic moduli of germanium,” J. Appl. Phys. **32**, 928-936 (1961).

[79] Y. H. Pao and W. Sachse, “Physical Acoustics,” Volume XVII, Academic press (1984).

[80] H. Fukuoka, H. Toda, and T. Yamane, “Acoustoelastic stress analysis of residual stress in a patch-welded disk,” Experimental Mechanics **18**(7), 277-280 (1978).

[81] C. S. Man and W. Y. Lu, “Towards an acoustoelastic theory for measurement of residual stress,” Journal of Elasticity **172**, 159-182 (1987).

[82] T. Leon-Salamanca and D. F. Bray, “Residual stress measurement in steel plates and welds using critically refracted longitudinal (LCR) waves,” Research in Nondestructive Evaluation **7**(4), 169-184 (1996).

[83] H. Qozam, J. Hoblos, G. Bourse, C. Robin, H. Walaszek, P. Bouteille and M. Cherfaoui, “Ultrasonic stress measurement in welded component by using Lcr

waves: analysis of the microstructure effect," Materials Science Forum **524**, 453-458 (2006).

[84] H. Qozam, S. Chaki, G. Bourse, C. Robin, H. Walaszek and P. Bouteille, "Microstructure effect on the Lcr elastic wave for welding residual stress measurement," Experimental Mechanics **50**, 179-185 (2010).

[85] Z. H. Zhu, M. A. Post and S. A. Meguid,"The potential of ultrasonic non-Destructive measurement of residual stresses by modal frequency spacing using leaky lamb waves," Experimental Mechanics **52**, 1329-1339 (2012).

[86] Z. H. Zhu, M. A. Post and P. C. Xu, "Stress evaluation using ultrasonic interference spectrum of leaky lamb waves," Experimental Mechanics **51**(6), 971-980 (2011).

[87] R. B. Thompson, "Elastic-wave propagation in random polycrystals: fundamentals and application to nondestructive evaluation," Imaging of Complex Media with Acoustic and Seismic Waves Topics in Applied Physics **84**, 233-257 (2002).